國 立 交 通 大 學

材 料 科 學 與 工 程 學 系

博 士 論 文

等通道轉角擠型製程對 ZA85 鎂合金之顯微組織與機械性質改善之研究

A Study on the Microstructures and Mechanical Properties of the ZA85 Magnesium Alloy Fabricated by Equal–Channel Angular Extrusion

研 究 生：林哲毅

指導教授：朝春光　博士

劉增豐　博士

中 華 民 國 一零三 年 六 月

等通道轉角擠型製程對 ZA85 鎂合金之顯微組織與機械性質改善之研究

A Study on the Microstructures and Mechanical Properties of the ZA85 Magnesium Alloy Fabricated by Equal–Channel Angular Extrusion

研 究 生：林哲毅　　Student：Che–Yi Lin

指導教授：朝春光　博士　　Advisor：Dr. Chuen–Guang Chao

劉增豐　博士　　Dr. Tzeng–Feng Liu

國 立 交 通 大 學

材 料 科 學 與 工 程 學 系

博 士 論 文

A Dissertation

Submitted to Department of Materials Science and Engineering

College of Engineering

National Chiao Tung University

in Partial Fulfillment of Requirements

for the Degree of

Dotor of Philosophy

in

Materials Science and Engineering

June 2014

Hsinchu, Taiwan

中 華 民 國 一零三 年 六 月

等通道轉角擠型製程對 ZA85 鎂合金之顯微組織與機械性質改善之研究

研究生：林哲毅　　指導教授：朝春光　博士

劉增豐　博士

國 立 交 通 大 學

材 料 科 學 與 工 程 學 系

摘　要

本研究係以重力澆鑄法製成 ZA85 (Mg–8 wt.% Zn–5 wt.% Al) 鎂合金鑄錠，接著分別將此鑄造材及經過固溶熱處理(solution heat treatment, SHT)的 ZA85 鎂合金經由等通道轉角擠型(equal–channel angular extrusion, ECAE)以改善合金的顯微組織與機械性質。研究結果顯示，高溫下對 ZA85 鎂合金進行 ECAE，其晶粒細化的機制為動態再結晶，ZA85 鎂合金鑄造材的初始晶粒可從 150 μm 大幅細化至 4 μm。在晶界上的 $Mg_{32}(Al,Zn)_{49}$ (τ–phase)不連續晶出相尺寸亦從 100 μm 被剪切至 1 μm，且此細小的 τ–phase 顆粒均勻的分布在動態再結晶的晶界上。在室溫機械性質的部分，試片在經過 ECAE 後，其最大拉伸強度(ultimate tensile strength, UTS)及降伏強度(yield strength, YS)可分別從鑄造材的 175 及 131 MPa 提升至 402 及 281 MPa；在 200 ℃ 高溫機械性質的部分，經過 ECAE 製程的試片其 UTS 及 YS 亦分別從鑄造材的 105 及 74 MPa 提升至 249 及 162 MPa。此機械性質的顯著提升歸因於大幅細化的晶粒以及均勻分布在動態再結晶晶界上的細小 τ–phase 顆粒。

另一方面，經過 SHT 的 ZA85 鎂合金其顯微組織顯示幾乎所有的不連續晶

出相 τ–phase 皆溶回鎂基地內，晶粒大小相較於鑄造材些微長大至 170 μm。經過兩階段的 ECAE 製程後，平均晶粒大小可大幅細化至 4 μm，未完全固溶回鎂基地的 τ–phase 被剪切至 1 μm 且均勻的分布在動態再結晶的晶界上，此外，亦可發現有許多平均尺寸約為 100 nm 的細小析出物 τ–phase 均勻的分布在鎂基地內，此細小的析出物是在 ECAE 製程中發生動態析出所產生。從拉伸試驗結果可發現，藉由 SHT + ECAE 製程可進一步提升 ZA85 鎂合金的機械性質。在室溫以及 200 ℃ 的環境下，ZA85 鎂合金的 UTS 及 YS 可分別提升至 415 MPa/284 MPa 及 261 MPa/173 MPa。此強化的結果歸因於晶粒細化、析出強化以及細小且均勻分布的高溫穩定相 τ–phase。

經過 ECAE 製程的 ZA85 鎂合金除了可以大幅提升強度外，延性亦能獲得大幅的改善，在適當的溫度及應變速率範圍內，本研究結果發現經過 ECAE 的 ZA85 鎂合金具由低溫超塑性(low temperature superplasticity, LTSP)以及高應變速率超塑性(high strain rate superplasticity, HSRSP)。LTSP 的部分，在 300 ℃，應變速率為 1.0×10^{-3} s^{-1} 以及 1.0×10^{-4} s^{-1} 的測試條件下，ZA85 鎂合金的伸長量分別為 147%及 400%；在 250 ℃，應變速率為 1.0×10^{-4} s^{-1} 的測試條件下，伸長量可達 205%。HSRSP 的部分，在 400 ℃，應變速率為 1.0×10^{-2} s^{-1} 的測試條件下，伸長量可達 113%。進一步探討材料的變形機制，ZA85 鎂合金在 300 及 350 ℃，應變速率為 1.0×10^{-3} s^{-1} 以及 1.0×10^{-4} s^{-1} 的測試條件下，其變形機制為晶界擴散控制的晶界滑動，在更高溫的 400 ℃，其變形機制轉換成差排潛變。

關鍵字：ZA85 鎂合金；等通道轉角擠型；晶粒細化；固溶熱處理；動態析出；超塑性

A Study on the Microstructures and Mechanical Properties of the ZA85 Magnesium Alloy Fabricated by Equal–Channel Angular Extrusion

Student：Che–Yi Lin **Advisor：Dr. Chuen–Guang Chao**

Dr. Tzeng–Feng Liu

Department of Materials Science and Engineering

National Chiao Tung University

Abstract

In this study, the as–cast and solution–heat–treated Mg–8 wt.% Zn–5 wt.% Al (ZA85) alloys were subjected to the equal–channel angular extrusion (ECAE). The microstructural evolutions and tensile properties of the experimental alloys were investigated. In the as–cast ZA85 alloy, the initial grain size and precipitate size of 150 and 100 μm were greatly reduced to 4 and 1 μm, respectively, after the ECAE process. The grain–refinement mechanism of the experimental alloy fabricated by the ECAE process is dynamic recrystallization. At room temperature (RT), the ultimate tensile strength (UTS) and yield strength (YS) of the ECAE processed specimens were 402 and 281 MPa, respectively, compared with 175 (UTS) and 131 MPa (YS) for the as–cast specimens. At 200 ℃, the UTS and YS of the ECAE processed specimens improved to 249 and 162 MPa, respectively, compared with 105 MPa (UTS) and 74 MPa (YS) for the as–cast specimens. This improvement in tensile properties of the ZA85 alloy was attributed to the refined grains and the well–distributed fine $Mg_{32}(Al,Zn)_{49}$ (τ–phase) precipitates.

In order to further improve the mechanical properties of the ZA85 alloy, the as–cast ZA85 alloy was subjected to solution heat treatment (SHT). Dynamic precipitation was then induced using two–step ECAE process. After the SHT process, almost all the non–continuous τ–phase dissolved into the α–Mg matrix and the average grain size slightly increased to 170 μm. After six ECAE passes, the average grain size was greatly reduced to 4 μm, and fine τ–phase particles with ~100 nm in size were uniformly distributed in the α–Mg matrix by dynamic precipitation. The combination of SHT + ECAE process was demonstrated to greatly improve the tensile properties of the experimental alloy. By testing over a range of temperatures, the maximum ultimate tensile strength and the yield strength of 415 MPa/284 MPa and 261 MPa/173 MPa were obtained at RT and 200 ℃, respectively. The strengthening factors for the SHT + ECAE alloy are the grain refinement, precipitation hardening, and presence of fine and well–distributed τ–phase particles.

It was also demonstrated that ECAE processing produces superplasticity. By testing over a range of temperatures and strain rates, the ECAE processed ZA85 alloy exhibits both low temperature superplasticity (elongations of 147% and 400% at 300 ℃ with initial strain rates of 1.0×10^{-3} s^{-1} and 1.0×10^{-4} s^{-1}, respectively; an elongation of 205% at 250 ℃ with the initial strain rate of 1.0×10^{-4} s^{-1}) and high strain rate superplasticity (an elongation of 113% at 400 ℃ with the initial strain rate of 1.0×10^{-2} s^{-1}). The dominant deformation mechanism for the specimens tested at 300 and 350 ℃ with the initial strain rates ranging from 1.0×10^{-4} s^{-1} to 1.0×10^{-3} s^{-1} is GBS controlled by grain boundary diffusion. At the higher testing temperature of 400 ℃, the deformation mechanism for the experimental alloy is dislocation creep.

Keywords: ZA85 alloy; Equal–channel angular extrusion (ECAE); Grain refinement; Solution heat treatment; Dynamic precipitation; Superplasticity

致　謝

在這漫長的學習過程中，由衷感謝指導老師朝春光教授以及劉增豐教授這些年來的諄諄教誨以及悉心指導，在研究遇到困難與瓶頸時，總是能指引我實驗的方向並給予許多建議，使我獲益良多也讓我能順利地完成研究以及此篇論文。感謝師範大學工教系的學長郭金國教授提供鎂合金的熔煉場所，才使得本研究得以順利進行。另外還要特別感謝 UCLA 材料系系主任楊鎮銘教授，在我於美國交換學生的那一年期間，不論是在研究或是生活上都給予我相當多的幫忙。感謝葉柏青博士、Tim Tseng、張元瑋、Jonathan Quan 讓我在人生地不熟的異鄉能有回到家的親切感。

在實驗室的成員中特別要感謝的是蔡浩然學長，從我碩一進實驗室到博士班畢業這七年，不論是在研究亦或是生活上都給予我許多幫助與建議，本研究使用的熔煉設備以及 ECAE 設備皆是我們共患難辛苦的成果，在此除了感謝之外也恭喜學長已順利取得博士學位。感謝王承舜博士、段逸軒博士、林志龍博士、陳柏至博士、張凱明、黃世陽、王浩仰、陳永昌學長們在課業上及研究上的建議與協助，也感謝林晟毅、李孝謙、張珮珊、薛舜仁、馬可威、陳俊宏、宋明翰、劉建寶、王思穎學弟妹們在實驗以及生活上給予的幫忙與照應。另外還要特別感謝湯季高、羅俊傑、涂宏恩學長們在這漫長的研究路上的陪伴，有你們一起聊天打嘴砲才能讓苦悶的研究生活更加多采多姿。

要感謝的人實在太多，最要感謝的莫過於是我最親愛的父母、妹妹以及總是在背後默默支持我的女朋友筱婷，在我遇到挫折瓶頸時給我鼓勵與支持，且提供我衣食無虞的生活，讓我能心無旁騖、無後顧之憂的完成學業，對於你們的付出，我的心中充滿萬分的感恩與感動，在此，謹以此論文獻給我摯愛的家人。

Contents

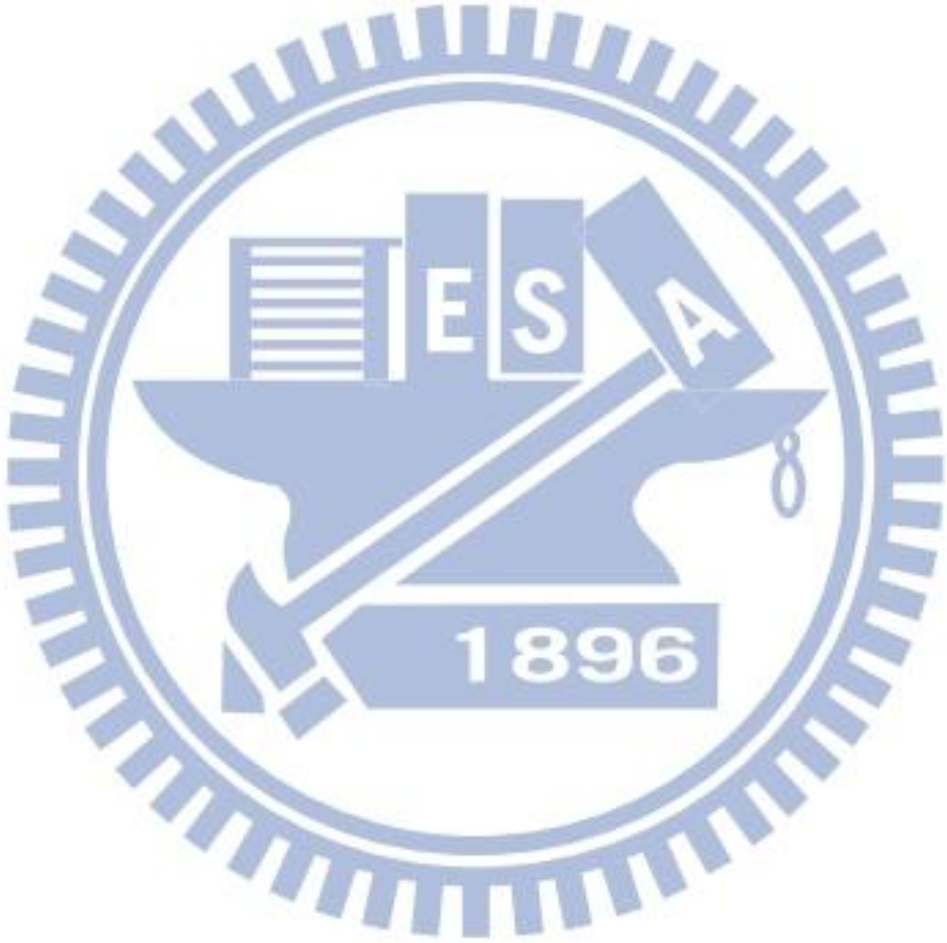

Table Captions

Chapter 3

Chapter 4

Figure Captions

Chapter 2

Chapter 3

Chapter 4

Chapter 5

Chapter 1 Introduction

1.1 General Background

Magnesium–based alloys are among the lightest of all structural metals. They have excellent strength (or stiffness)–to–weight ratio, superior damping capacity, high impact resistance, well electromagnetic shielding characteristics and are cost–effective in engineering applications [1–4]. These properties give magnesium alloys a broad range of applications, especially in electronic industries, aircraft industries as well as automobile industries. In automobile industries, the use of magnesium alloys was only 0.22kg/car in Europe in 1995. However, European Union had demanded that the manufacturers need to take the discarding charges by themselves from 2006 and the recycle rate of discarding cars need to reach to 95% by 2015. The strict laws had greatly increased the consumption of magnesium alloys in automobile industries in Europe. According to the estimation, the growth rate of magnesium usage in Europe is going to reach 30% per year. In addition, the recycle rate of automobile rubbish will arrive at 95% by 2015 in Japan, which also makes Japan automobile manufacturers take more consideration in designing new cars in the future. Thus, the application of magnesium alloys in automobile industries will be increased.

However, the application of magnesium alloys in automobile industries is mainly on the structural components and frame of cars. The engine and transmission system which possess considerable extent in total weight of automobiles are the potential parts for the development of magnesium alloys. The main limitation for the application of magnesium alloys in the engine and transmission system in which the working temperature is about 200 ℃ is the poor high–temperature properties of the

commercial AZ– and AM–series magnesium alloys. These alloys are unsuitable for use at temperature above 120 ℃ since they show poor creep resistance and large decrease in strength at elevated temperature. This phenomenon is attributed to the presence of the intermetallic phase β–$Mg_{17}Al_{12}$ which precipitates along grain boundaries and exhibits a low melting point. Thus, grain boundary sliding is allowed to occur even at temperature below 150 ℃ [5]. In recent year, it has been reported that a ternary addition of a large amount of zinc to binary Mg–Al alloys can completely suppress the formation of the β–phase [6,7]. The precipitate of Mg–Zn–Al (ZA) alloys is $Mg_{32}(Al,Zn)_{49}$ (τ–phase), which has a higher melting point and decomposition temperature [8]; therefore, ZA alloys exhibit better properties at elevated temperatures compared with commercial AZ alloys.

Besides, there are still some properties which make the applications of magnesium alloys not as extensive as aluminum alloys by now: (I) Poor high–temperature properties because magnesium alloys are all prone to excessive creep deformation when exposed to even low levels of load at high temperature, as mentioned above; (II) Low ductility at room temperature because of their hexagonal close–packed (HCP) crystalline structure which has deficient slip systems; (III) Difficult to smelt and manufacture, and easy to combust with oxygen because of their high chemical activity; (IV) Poor corrosion resistance. In recent years, as the improving surface–treatment techniques, the oxidation resistance of magnesium alloys can be improved effectively. Consequently, improving the poor ductility and high–temperature properties of magnesium alloys in order to broaden their applications is the most important issue of magnesium alloys nowadays.

One of the promising methods adopted to increase both the strength and ductility of materials is microstructural refinement. Such methods are mechanical alloying [9–12], rapid solidification processing [13–15], torsion straining [16–18],

reciprocating extrusion [19–21], and equal channel angular extrusion (ECAE) [22–25]. They all resulted in producing bulk ultrafine-grained magnesium alloys with high strength and ductility. Among them, the ECAE process is one of the most often used severe plastic deformation (SPD) methods, which can result in bulk, homogeneous submicron or nanocrystalline microstructure [26–29]. The ECAE die is a block with two intersecting channels of identical cross section. SPD by simple shear occurs in a zone where the two channels meet. Large amount of strain can be accumulated by repeated pressing since the cross section of the specimen is identical after pressing [25]. Also, the ECAE process can be used to eliminate defects such as blow holes and shrinkages introduced by the casting process and to refine coarse precipitates, which will significantly improve the strength and ductility of the materials.

ECAE research on Mg alloys has focused mainly on AZ alloys. The effects of the ECAE process on ZA alloys, which have better high–temperature properties compared with AZ alloys, have not been investigated yet. Therefore, the purpose of this study is an attempt to improve the strength and ductility at room temperature (RT) as well as at elevated temperatures of the ZA85 magnesium alloy by using the ECAE process. The microstructural evolutions after the ECAE process are also investigated.

1.2 Organization of the Dissertation

This dissertation is divided into six chapters.

In chapter 2, the literatures are reviewed, including the development of high–temperature magnesium alloys, characteristics of the ECAE process, deformation mechanism of magnesium alloys, precipitation hardening of magnesium alloys, and Superplasticity of Magnesium alloys.

In chapter 3, the as–cast ZA85 alloy was subjected to the ECAE process and the

microstructural evolutions after the ECAE process are investigated in details. Both the size of grains and precipitates were greatly refined after the ECAE process. The grain–refinement mechanism of the experimental alloy is characterized as dynamic recrystallization. Moreover, the mechanical properties are also investigated at RT and high temperature of 200 ℃. It was found that both the strength and ductility of the experimental alloy increased with increasing number of ECAE passes.

In chapter 4, the as–cast ZA85 alloy was subjected to the solution heat treatment (SHT) prior to the ECAE process in order to further improve the mechanical properties of the experimental materials. The microstructural evolutions after the SHT + ECAE process are also characterized in details. It was found that dynamic precipitation occurred during the ECAE process and formed the fine and well–distributed τ–phase (~100 nm in size) within the α–Mg matrix. RT and high–temperature tensile tests showed that the specimens fabricated by SHT + ECAE have better mechanical properties than those fabricated only by the ECAE process.

In chapter 5, superplasticity of the ZA85 alloy processed by ECAE is investigated. The deformation mechanism of the experimental alloy is characterized in details. It was demonstrated that ECAE processing greatly enhances ductility of the experimental alloy. In this study, the ECAE processed ZA85 alloy exhibits both low temperature superplasticity and high strain rate superplasticity.

Finally, the summary and conclusions of the results in this dissertation is given in chapter 6.

References

[1] X.F. Huang, W.Z. Zhang, J.F. Wang, W.W. Wei, Journal of Alloys and Compounds 516 (2012) 186.

[2] K. Cho, T. Sano, K. Doherty, C. Yen, G. Gazonas, P. Moy, B. Davis, R. DeLorme," Magnesium Technology and Manufacturing for Ultra light Weight Armored Ground Vehicles", Proceedings of 26th Army Science Conference

[3] J. Wang, S. Gao, P. Song, X. Huang, Z. Shi, F. Pan, Journal of Alloys and Compounds 509 (2011) 8567.

[4] M. Bamberger, G. Dehm, Annual Review of Materials Research 38 (2008) 505.

[5] Y. Guangyin, S. Yangshan, D. Wenjiang, Materials Science and Engineering A 308 (2001) 38.

[6] A. Srinivasan, U.T.S. Pillai, B.C. Pai, Metallurgical and Materials Transactions 36 A (2005) 2235.

[7] B.H. Kim, S.W. Lee, Y.H. Park, I.M. Park, Journal of Alloys and Compounds 493 (2010) 502.

[8] I.A. Anyanwu, Y. Gokan, S. Nozawa, A. Suzuki, S. Kamado, Y. Kojima, S. Takeda, T. Ishida, Materials Transactions 44 (2003) 562.

[9] C. Suryanarayana, E. Ivanov, V.V. Boldyrev, Materials Science and Engineering A 304–306 (2001) 151.

[10] J.S. Benjamin, T.E. Volin, Metallurgical Transactions, 5 (1974) 1929.

[11] J. Patel, K. Morsi, Journal of Alloys and Compounds 540 (2012) 100.

[12] C. Martinez, S. Ordonez, D. Guzman, D. Serafini, I. Iturriza, O. Bustos, Journal of Alloys and Compounds 581 (2013) 241.

[13] E.J. Lavernia, T.S. Srivatsan, Journal of Materials Science 45 (2010) 287.

[14] S.S. Nayak, S.K. Pabi, D.H. Kim, B.S. Murty, Intermetallics 18 (2010) 487.

[15] Z.Zhang, H. Yu, S. Wang, H. Wang, G. Min, Journal of Materials Science and

Technology 26 (2010) 151.

[16] K. Nakamura, K. Neishi, K. Kaneko, M. Nakagaki, Z. Horita, Materials Transactions 45 (2004) 3338.

[17] Z. Horita, T.G. Langdon, Materials Science and Engineering A 410–411 (2005) 422.

[18] A.P. Zhilyaev, T.G. Langdon, Progress in Materials Science 53 (2008) 893.

[19] X.F. Guo, D. Shechtman, Journal of Materials Processing Technology 187–188 (2007) 640.

[20] W.P. Yang, X.F. Guo, K.J. Yang, Transactions of Nonferrous Metals Society of China 22 (2012) 255.

[21] S.W. Lee, Y.L. Chen, H.Y. Wang, C.F. Yang, J.W. Yeh, Materials Science and Engineering A 464 (2007) 76.

[22] V.M. Segal, Materials Science and Engineering A 197 (1995) 157.

[23] V.M. Segal, Materials Science and Engineering A 386 (2004) 269.

[24] V.M. Segal, K.T. Hartwig, R.E. Goforth, Materials Science and Engineering A 224 (1997) 107.

[25] M. Furekawa, Y. Iwahashi, Z. Horita, M. Nemoto, T.G. Langdon, Materials Science and Engineering A 257 (1998) 328.

[26] W.N. Tang, R.S. Chen, J. Zhou, E.H. Han, Materials Science and Engineering A 499 (2009) 404.

[27] B. Huarte, C.J. Luis, I. Puertas, J. Leon, R. Luri, Journal of Materials Processing Technology 162–163 (2005) 317.

[28] A.L. Etter, T. Baudin, C. Rey, R. Penelle, Materials Characterization 56 (2006) 19.

[29] Y.C. Yuan, A.B. Ma, J.H. Jiang, F.M. Lu, W.W. Jian, D. Song, Y.T. Zhu, Materials Science and Engineering A 588 (2013) 329.

Chapter 2 Literature Review

2.1 Development of High–Temperature Magnesium Alloys

In 1960, Volkswagen cooperated with Dow Chemical, Norsk Hydro, and University of Hanover to develop the first high–temperature magnesium alloy: AS41. The main second phase of the AS41 alloy is the thermally stable micro–needlelike Mg_2Si phase which precipitates along grain boundaries, resulting good creep resistance at elevated temperature, as shown in Fig. 2.1 [1–3]. The AS21 magnesium alloy which was developed afterwards has better creep resistance than the AS41 alloy. However, the decrease of aluminum content leads to poor casting properties. In 1970, two major types of high–temperature magnesium alloys were developed: AE– and ZA–series alloys. AE–series magnesium alloys which were developed by Dow Chemical and named as AE21 and AE42 had the addition of rare earth elements. The thermally stable intermetallic phase $Al_{11}(RE)_3$ would precipitate along grain boundaries, as shown in Fig. 2.2 [4]. At 150 ℃ with the load of 50MPa, the creep resistance of the AE42 alloy is a time and five times higher than those of the AS41 and AZ91 alloys, respectively, as shown in Fig. 2.3 [5]. However, the rare earth elements are expensive and easy to vanish during the melting process, which limits widespread applications of such alloys. On the other hand, NL Industries have developed several high–zinc magnesium alloys (ZA), including ZA124, ZA102, AZ88, and AZ55 alloys. The ZA124 alloy showed the same level of creep resistance as the AS41 alloy with better corrosion resistance and fluidity. The corrosion resistance of the ZA102 alloy can be further improved to the level of the AS42 alloy by adding 0.3 wt.% Ca into the alloy [6]. However, it had been reported that the addition of the Ca element would form the eutectic Mg–Al–Zn–Ca phase with low melting temperature.

Therefore, the ZA + Ca magnesium alloys cannot be used at temperatures above 175 ℃ [7]. They also have some problems such as hot cracking and the difficulty to be subjected to the die–casting process. The main precipitates of ZA series magnesium alloys is the τ–$Mg_{32}(Al,Zn)_{49}$ phase, which has higher melting point and decomposed temperature than those of the β–$Mg_{17}Al_{12}$ phase [8]. This result is also confirmed by the Mg–Zn–Al phase diagram, as shown in Fig. 2.4. J. Zhang et al. [9] reported that the high–temperature creep resistance of ZA–series magnesium alloys was superior to that of commercial AZ–series magnesium alloys, as shown in Fig. 2.5.

In 1990s, lots of magnesium–alloy suppliers and automobile corporations invested much capital in developing high–temperature magnesium alloys. Hydro corporation added small amount of RE into AS–series alloys in order to remain the creep resistance with the increase of corrosion resistance. In recent year, adding the Ca and Sr elements to replace the high–cost RE elements into magnesium alloys would result in better high–temperature properties [10–12]. The creep resistance of AJ– and AJC–series magnesium alloys is much better than that of the AE42 alloy by forming the high–temperature–stable phase along grain boundaries, as shown in Figs. 2.6 and 2.7. Dead Sea and Honda automobile corporations used the Ca element to replace some amount of RE elements to develop Mg–Zn–Al–Ca–RE alloys. It had been reported that in Mg–Zn–Al–Ca–RE alloys, $Al_{11}La_3$ phase formed in the α–Mg matrix with Al_2Ca precipitated along grain boundaries to hinder grain–boundary migration. Therefore, the creep resistance of Mg–Zn–Al–Ca–RE alloys is superior to those of the AE42 and AS41 alloys, as shown in Figs. 2.8 and 2.9 [13].

2.2 Equal–Channel Angular Extrusion (ECAE)

The ECAE process, invented by V.M. Segal in 1995, is one of the most often used SPD methods to result in bulk, homogeneous submicron or nanocrystalline

microstructure [14,15]. The ECAE die is a block with two intersecting channels of identical cross section. The inner angle and outer curvature of the ECAE channel are denoted as Φ and Ψ, respectively, as shown in Fig. 2.10. During the ECAE process, the specimen would be pressed through the ECAE channel and be deformed by a pure shear stress. Because the cross–sectional areas of the entrance and outlet channels are identical, large amount of strain can be accumulated by repeated pressing. This is the great merit of ECAE over the conventional extrusion. When subjected to the ECAE process, there are several factors which would affect the final microstructure of the materials, including the ECAE die angle, ECAE route, number of ECAE passes, processing temperature, and pressing rate.

Fig. 2.11 shows three different types of die–angle combination in the ECAE–die design. Under the assumption of no friction between the specimen and ECAE die, with different Ψ, the accumulated strain can be determined as the following equations [16].

(a) $\Psi = 0°$, $\gamma = 2\cot\frac{\Phi}{2}$,

(b) $\Psi = 180° - \Phi$, $\gamma = \Phi$,

(c) $0° < \Psi < 180° - \Phi$, $\gamma = 2\cot\left(\frac{\Phi}{2}+\frac{\Psi}{2}\right)+\Psi\csc\left(\frac{\Phi}{2}+\frac{\Psi}{2}\right)$,

where γ is the accumulated shear strain. Therefore, when the specimen is pressed through the ECAE die with the angles of Φ and Ψ once, the accumulated shear strain will be $\gamma = 2\cot\left(\frac{\Phi}{2}+\frac{\Psi}{2}\right)+\Psi\csc\left(\frac{\Phi}{2}+\frac{\Psi}{2}\right)$. In addition, from the theory of plastic mechanics, the equivalent strain can be determined by the following equation:

$$\varepsilon_{eq} = \left[\frac{2\left(\varepsilon_x^2+\varepsilon_y^2+\varepsilon_z^2+\frac{\gamma_{xy}^2+\gamma_{yz}^2+\gamma_{zx}^2}{2}\right)}{3}\right]^{1/2} \quad \cdots\cdots\cdots(1)$$

where ε_{eq} is the equivalent strain, ε_x, ε_y, and ε_z are the normal strains in x, y, and z directions, respectively, and γ_{xy}, γ_{yz}, and γ_{zx} are the shear strains in x–y, y–z, and z–x planes, respectively. Because the specimen experiences pure shear stress during the ECAE process, $\varepsilon_x = \varepsilon_y = \varepsilon_z = \gamma_{yz} = \gamma_{zx} = 0$. Thus, the relationship between the equivalent strain and die angles of Φ and Ψ after one single pass can be evaluated by the following equation:

$$\varepsilon_{eq} = \frac{\left(2\cot\left(\frac{\Phi}{2}+\frac{\Psi}{2}\right)+\Psi\csc\left(\frac{\Phi}{2}+\frac{\Psi}{2}\right)\right)}{\sqrt{3}} \quad \cdots\cdots\cdots(2)$$

Consequently, after N ECAE passes, the total amount of accumulated strain can be determined by the following equation:

$$\varepsilon_{eq,total} = N\left[\frac{2\cot\left(\frac{\Phi}{2}+\frac{\Psi}{2}\right)+\Psi\csc\left(\frac{\Phi}{2}+\frac{\Psi}{2}\right)}{\sqrt{3}}\right] \quad \cdots\cdots\cdots(3)$$

Fig. 2.12 shows the relationship between the amount of equivalent strain and ECAE die angles of Φ and Ψ after one single pass [17]. It can be inferred that the equivalent strain decreases with increasing both Φ and Ψ, while Φ shows more influence than Ψ.

Different routes of ECAE process result in different microstructures. There are four kinds of ECAE routes: route A, route B_A, route B_C, and route C, as shown in Fig. 2.13 [18]. By using route A in which the sample is deformed in the same surface, the microstructure will become to a thin–foil structure like the one fabricated by the conventional extrusion. Route B_A in which the specimen is rotated through 90° in the different direction after each pass. That is, after one pass, if the specimen is subjected to clockwise rotation, the specimen will be rotated counterclockwise after another one pass. Therefore, the shear stress is applied on two specific planes, leading to a non–uniform microstructure. By using route B_C in which the specimen is rotated through 90° in the same direction after each pass, the refined and equiaxed–grain

structure will be obtained after every 4 ECAE passes [19]. Route C in which the specimen is rotated through 180° after each pass is another way to obtain the equiaxed–grain microstructure.

There are several factors that determine whether the specimen can go through the ECAE die successfully or not, such as the ECAE processing temperature, pressing rate, and initial grain size. As for the ECAE processing temperature, Al alloys which have 12 sets of slip systems because of their face–centered cubic (FCC) crystalline structure can be pressed through the ECAE die successfully even at RT. However, in Mg alloys, there are only three slip systems at RT due to their HCP crystalline structure. Therefore, the ECAE processing temperature is usually higher than 200 ℃ [20–22]. By applying a back pressure, the ECAE processing temperature can be lowered in the Mg alloys. K. Xia et al. applied a back pressure of 50 MPa to successfully press the AZ31 alloy through the ECAE die for eight passes at 150 ℃ [23]. In the aspect of the pressing rate, Semiatin et al. subjected the 4340 steel to the ECAE process at 350 ℃ with different pressing rates and found that high pressing rate would lead to the failure of the sample, as shown in Fig. 2.14 [24]. Kang et al. subjected the AZ31 alloy to the ECAE process with different temperatures and pressing rates and found that the pressing rate could be increased by increasing ECAE processing temperature, as shown in Fig. 2.15 [25]. The initial grain size is also an important factor for the ECAE process. Matsubara et al. subjected the as–cast Mg–9% Al alloy with the initial grain size of 50 μm to the ECAE process at 200 ℃ and 8 mm/s and found that the sample experienced failure after only one ECAE pass. Thus, they conducted the conventional extrusion prior to the ECAE process to reduce the grain size of the alloy to about 12 μm. With the same ECAE processing condition, the as–extruded Mg– 9% Al alloy was successfully pressed through the ECAE die for two passes [26]. In summary, raising the ECAE processing temperature can increase the

pressing rate; conducting to other processes prior to the ECAE process to preliminarily refine grains can increase the ECAE processing temperature and/or pressing rate.

2.3 Deformation Mechanism of Magnesium Alloys

Magnesium alloys which have HCP crystalline structure have limited slip systems, leading to a poor workability. In order to address this issue, a large number of studies have been carried out to date on single crystals, poly–crystals, and by modeling to understand the deformation and recrystallization mechanisms at a wide range of temperatures [27–31]. Possible slip systems in magnesium alloys include three basal ((0001)<a>), three prismatic ($\{10\bar{1}0\}$<a>), and twelve pyramidal ($\{10\bar{1}1\}$<a> and $\{11\bar{2}2\}$<c + a>). In addition, six $\{10\bar{1}2\}$ extension twinning systems and a total of twelve $\{10\bar{1}1\}$ and $\{10\bar{1}3\}$ contraction twinning [32] systems are also available. The critical resolved shear stress (CRSS) is the minimum stress required to activate the slip systems. It is agreed that, at RT, $CRSS_{basal} < CRSS_{extension\ twinning} < CRSS_{prismatic} < CRSS_{pyramidal}$ [29]. The relative ratio of these CRSS values depends on the alloying elements, grain size, strain rate, and temperature. Slip band analysis on Mg single crystals deformed along the hexagonal axis at temperatures ranging from room temperature to 400 ℃ showed basal and prismatic slip traces at temperatures below 400 ℃. After deformation at 400 ℃, pyramidal slip traces were observed [33,34]. Galiyev et al. found $\{11\bar{2}2\}1/3\langle\bar{1}\bar{1}23\rangle$ slip traces and <c + a> dislocations in a warm deformed (150 ℃) ZK60 alloy. They observed increasing <c + a> dislocation density with increasing temperature. The authors ascribed the activation of non–basal slip to locally high compatibility stresses at grain boundaries, which exceeds the CRSS for

non–basal slip [35].

Understanding the recrystallization mechanisms during hit working of magnesium alloys is also a key to improve workability, to control the grain size and texture and, thus, to alter the final properties. Several recrystallization mechanisms were observed to be operative in magnesium alloys, namely continuous dynamic recrystallization (CDRX) [36,37], discontinuous dynamic recrystallization (DDRX) [38,39], twinning induced dynamic recrystallization (TDRX) [40], and particle stimulated nucleation (PSN) [41]. DRX has been found to be strongly related to the operative slip and twinning systems [35,42–44]. Most studies agree that recrystallization occurs readily when multiple slip operates, i.e., when both basal and non–basal systems contribute to deformation. The main characteristics of CDRX are summarized as follows [45]: (I) Stress–strain curves exhibit a single and smooth maximum, followed by a slow but significant softening stage. A steady state is observed at large strains, which can only be achieved in torsion (at von Mises equivalent $\varepsilon \sim 30$). The flow stress and all the average microstructural parameters remain independent of strain; (II) The crystalline size decreases greatly up to a strain $\varepsilon \sim 5$, then, it increases slowly to reach a steady value at large strains ($\varepsilon \sim 30$); (III) Low–angle boundaries are generated at low strains, and part of them start to transform into high–angle boundaries at moderate strains ($\varepsilon \sim 1$); (IV) A strong crystallographic texture forms at large strains. DDRX typically accompanies regular multipeak stress oscillations on stress–strain curves resulting from constant–strain–rates or constant–displacement–speeds tests [46]. The microstructure after testing shows recrystallized grains containing subgrains. In general, DDRX occurs in low to medium stacking fault energy alloys during the hot deformation. New grains are formed by strain–induced grain boundary motion once a critical shear stain is reached [47]. Dislocation–free grains then grow as deformation continues by bulging into their

surroundings and consuming the deformed regions [48].

Janecek et al. proposed that the grain–refinement mechanism for magnesium alloys processed by ECAE is DRX [49]. They have subjected the as–cast AZ31 alloy with the initial grain size of 380 μm to the ECAE process at 200 ℃ with the pressing rate of 15 mm/min via route B_C. After one ECAE pass, the microstructure shows a typical large–deformed structure with high dislocation density in the matrix, as shown in Fig. 2.16. After four ECAE passes, the microstructure of the experimental alloy consists of larger grains of 1–3 μm in size and finer grains of 500–800 μm in size, and no dislocation is observed within some grains, as shown in Fig. 2.17. The dislocation density increases owing to the large amount of strain accumulated by the repetition of ECAE processes. Then, dynamic recrystallization occurs in the area of high dislocation density, producing numerous fine grains and reducing dislocation density. Lv et al. had investigated the DRX evolution of Mg–2.0 Zn–0.3 Zr– 0.9 Y alloy using compression test conducted at 250–400 ℃ with strain rate rang of 0.001–1 s^{-1} [50]. They concluded that in the strain rate range of 0.001–0.01 s^{-1}, DRX grains are mainly formed at original grain boundaries and second phase particles, and DRX volume fraction increases with increasing deformation temperature; in the strain rates range of 0.1–1 s^{-1}, DRX grains are mainly formed in twins, and DRX volume fraction decreases with increasing deformation temperature, as shown in Fig. 2.18. The processing map exhibits a deformation domain of complete DRX occurring in the deformation range of 350–400 ℃ and the strain rate range of 0.001–0.01 s^{-1}.

2.4 Precipitation Hardening of Magnesium Alloys

2.4.1 Precipitation Hardening (T6 Heat Treatment)

In general, T6 heat treatment involves two separate steps, including solution heat treatment (SHT) and artificial aging. SHT in which an alloy or metal is heated to a

suitable temperature, is held at that temperature long enough to allow a certain constituent to enter into solid solution, and is then cooled rapidly to form supersaturated solid solution (SSSS). The complete dissolution of phases is depended on the solutionising temperature, time, and chemical composition of the alloy. Among these parameters, the temperature and time are controlled to elucidate the heat treatment process. The artificial aging process results transformation of SSSS into fine precipitates [51]. The artificial–aging behavior is also depended upon the aging time, temperature, and coherency between the matrix and precipitates. Because precipitation is a diffusion–dependant process, higher temperature results in faster nucleation and growth rates. At same aging temperature with longer time, the size of precipitates increases. As a result, the coherency between the matrix and precipitates transforms from coherent to semi–coherent, and then to incoherent. These transformations correspond to the three stages in the age–hardening curve, i.e. under aging, aging, and overaging, respectively. In Mg–Zn–Al alloys, the high Zn content (above 6 wt%) makes it difficult for complete dissolution of the precipitates because Zn exceeds the maximum solid solubility limit [52]. Furthermore, the solutionising time must be carefully determined to allow the maximum dissolution of precipitates into the matrix. Balasubramani et al. [53] have subjected the as–cast ZA84 alloy to the T6 heat treatment at different temperature and/or time in order to determine the optimum parameters for the SHT and artificial aging in the ZA84 alloy. The differential thermal analysis (DTA) showed that the liquidus and solidus temperatures of the ZA84 alloy are 593.44 and 346.62 ℃, respectively. Based on the DTA results, the solutionising temperature of the ZA84 alloy is 335 ℃ which is slightly less than the solidus temperature. They also reported that the amount of dissolved precipitates increases with increasing time at solutionising temperature of 335 ℃, whereas phase melting is observed at grain boundaries when solutionising time exceeds 48 h, as

shown in Fig. 2.19 [53]. As for the artificial aging, the hardness of the solution–heat–treated ZA84 alloy reached maximum value at 180 ℃ for 16 h, as shown in Fig. 2.20 [53]. Therefore, the optimum temperature/time required for SHT and artificial aging in the ZA84 alloy are 335 ℃/48 h and 180 ℃/16 h, respectively.

2.4.2 Dynamic Precipitation

Dynamic precipitation (or dynamic aging) is a process that combines thermo–mechanical processing (TMP) and an aging treatment. After the SHT process, the precipitation reaction occurs simultaneously during TMP. Several studies have reported that materials fabricated by SHT + TMP process have greater mechanical properties than those fabricated by T6 heat treatment [54–57]. Cai et al. have reported that, compared with a static aging process, both the 6061 and 6069 aluminum alloys experienced dynamic precipitaion and that the peak values of the hardness were reached within a shorter time after the SHT + TMP process, as shown in Fig. 2.21 (a) [54]. Moreover, the peak values of hardness, ultimate tensile strength (UTS), and yield strength (YS) of the dynamically aged alloys are also greater than those of the statically aged alloys, as shown in Fig. 2.21 (b) [54]. Roven et al. investigated the precipitation behavior during the ECAE process in an Al–Mg–Si alloy and found that fine–spherical precipitates are dynamically formed during ECAE. The length of the precipitates is much less than that of the precipitates observed after static aging. The hardness values after ECAE at both RT and 175 ℃ are much higher than the peak values in the specimens statically aged at 175 ℃. They suggested that this increase in strength is because the finer precipitates and high dislocation density induced by the ECAE process enhance dislocation strengthening and precipitation refinement strengthening [55]. Hou et al. have subjected the Mg–Gd–Y–Nd–Zr alloy to the hot compression process to investigate the dynamic precipitation behavior [58]. They

found that the morphology of precipitates obtained by dynamic precipitation differs from that of the same phase produced by T6 heat treatment. But their orientation relationship with Mg matrix does not change.

2.5 Superplasticity of Magnesium Alloys

Superplastic forming (SPF), defined as elongations of at least 100% and strain rate sensitivity close to 0.5, is an effective method to fabricate hard–to–form materials into complex shapes [59,60]. For SPF to be used in industry, the development of high strain–rate superplasticity (HSRSP), defined as superplasticity occurring at strain rates at or above 1.0×10^{-2} s^{-1} [61], is needed, especially for Mg alloys with poor formability. R.B. Figueiredo et al. [62] proposed two strategies for achieving HSRSP in Mg alloys processed by equal–channel angular extrusion (ECAE): (I) by pressing the alloys through a reduced number of passes in order to increase the thermal stability of the microstructure; and (II) by increasing the processing temperature to permit the occurrence of superplastic flow at higher testing temperatures. Another desirable property for developing superplasticity in a material is low temperature superplasticity (LTSP), defined as superplasticity occurring at temperatures at or below 0.55 T_m, where T_m is the alloy melting temperature [61]. The presence of LTSP is an attractive property in Mg alloys because of their susceptibility to surface oxidation when formed at elevated temperatures and their low formability at temperatures close to RT.

Many previous experiments established that superplasticity requires a small polycrystalline grain size (typically less than 10 μm [63]) and these small grains are generally achieved through the application of SPD. As mentioned in chapter 2.2, ECAE is one of the most popular SPD methods and has proved to be effective in refining grains in various Mg alloys, resulting in improved ductility, strength, and

superplasticity [14,26,64–71]. K. Matsubara et al. [26] reported that the Mg–9% Al alloy processed by a combination of extrusion and ECAE exhibited a maximum elongation of 840% at 200 ℃ with a strain rate of 3.3×10^{-4} s^{-1}. R.B. Figueiredo et al. [64] reported that an ECAE processed ZK60 alloy showed a maximum elongation of 3050% at 200 ℃ with a strain rate of 1.0×10^{-4} s^{-1}. V.N. Chuvil'deev et al. [65] found that the ECAE processed AZ91 alloy possessed 570% in elongation at 300 ℃ with a strain rate of 3.0×10^{-3} s^{-1} and the ECAE processed ZK60 alloy exhibited 810% in elongation at 260 ℃ with a strain rate of 3.0×10^{-3} s^{-1}, as shown in Fig. 2.22. X. Liu et al. [68] reported that the as–rolled LZ82 alloy exhibited superplasticity with a maximum elongation of 430% at 225 ℃ and of 120% even at 150 ℃ with a strain rate of 1.6×10^{-4} s^{-1}, as shown in Fig. 2.23. Y. Miyahara et al. [69] found that the ECAE processed AZ61 possessed 1320% at 200 ℃ with a strain rate of 3.3×10^{-4} s^{-1}, as shown in Fig. 2.24. M. Kawasaki et al. [70] also provided a very detailed tabulation of all papers reporting superplasticity in metals processed by the ECAE process.

Superplastic deformation is an integrated process that combines grain boundary sliding (GBS), dislocation movement, and diffusion in intracrystalline. The *m* value represents the proportion of GBS, and it is well known that high strain rate sensitivity (typically *m* close to 0.5) is a characteristic of superplastic metals and alloys [72,73]. The stress exponent (*n* value), which is reciprocal of the *m* value, is calculated to determine deformation mechanism of the materials. It has been reported that the *n* value of the GBS and the dislocation creep mechanisms are 2 and 3, respectively [73,74]. Moreover, GBS is usually accommodated by slip controlled by diffusion [75]. To further understand the deformation mechanism of mateirals, the activation energy for the deformation is calculated under constant strain rate using the following formula [76]:

$$Q = nR\frac{\partial(\ln\sigma)}{\partial(1/T)}$$

where Q is the apparent activation energy, n is the stress exponent, R is the gas constant (R = 8.31 J/(K · mol)), σ is the true stress, and T is the absolute temperature. Therefore, according to the relationship of $\ln\sigma$ versus $1/T$ at different strain rates during the deformation, the activation energy Q can be calculated, and then, the deformation mechanism of materials can be determined.

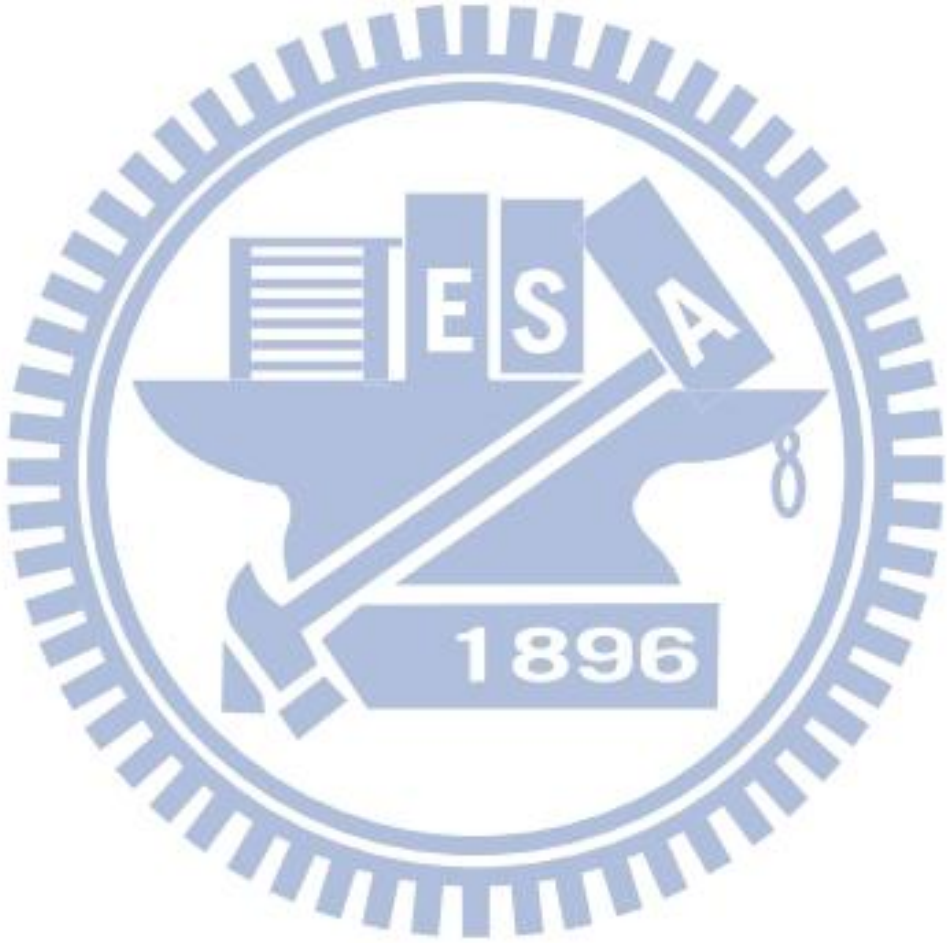

References

[1] P. Zhang, Scripta Materialia 52 (2005) 277.

[2] E. Evangelista, E. Gariboldi, O. Lohne, S. Spigarelli, Materials Science and Engineering A 387–389 (2004) 41.

[3] B. Bronfin, M. Katsir, E. Aghion, Materials Science and Engineering A 302 (2001) 46.

[4] I.P. Mpreno, T.K. Nandy, J.W. Jones, J.E. Allison, T.M. Pollock, Scripta Materialia 48 (2003) 1029.

[5] G. Petterson, H. Westengen, R. Hoier, O. Lohne, Materials Science and Engineering A 207 (1996) 115.

[6] Z. Zhang, R. Tremblay, D. Dube, Materials Science and Engineering A 385 (2004) 286.

[7] A.A. Luo, Materials Science Forum 419–422 (2003) 57.

[8] Z. Zhang, A. Couture, A. Luo, Scripta Materialia 39 (1998) 45.

[9] J. Zhang, Z. X. Guo, F. Pan, Z. Li, X. Luo, Materials Science and Engineering A 456 (2007) 43.

[10] B. Jing, S. Yangshan, X. Shan, X. Feng, Z. Tianbai, Materials Science and Engineering A (2006) 181.

[11] K. Hirai, H. somekawa, Y. Takigawa, K. Higashi, Materials Science and Engineering A 403 (2005) 276.

[12] R. Ninomiya, T. Ojiro, K. Kubota, Acta Metallurgica et Materialia (2005) 276.

[13] I. Anyanwu, Y. Gokan, A. Suzuki, S. Kamado, Y. Kojima, S. Takeda, T. Ishida, Materials Science and Engineering A (2004) 93.

[14] V.M. Segal, Materials Science and Engineering A 197 (1995) 157.

[15] V.M. Segal, K.T. Hartwig, R.E. Goforth, Materials Science and Engineering A 224 (1997) 107.

[16] Y. Iwahashi, J. Wang, Z. Horita, M. Nemoto, T.G. Langdon, Scripta Materialia 35 (1996) 143.

[17] Y. Iwahashi, Z. Horita, M. Nemoto, T.G. Langdon, Acta Materialia 11 (1997) 4733.

[18] V.M. Segal, Materials Science and Engineering A 386 (2004) 269.

[19] Y. Iwahashi, Z. Horita, M. Nemoto, T.G. Langdon, Acta Materialia 9 (1998) 3317.

[20] K. Mathis, J. Gubicza, N.H. Nam, Journal of Alloys and Compounds 394 (2005) 194.

[21] W.J. Kim, S.I. Hong, Y.S. Kim, S.H. Min, H.T. Jeong, J.D. Lee, Acta Materialia 51 (2003) 3293.

[22] S.R. Agnew, J.A. Horton, T.M. Lillo, D.W. Brown, Scripta Materialia 50 (2004) 377.

[23] K. Xia, J.T. Wang, X. Wu, G. Chen, M. Gurvan, Materials Science and Engineering A 410–411 (2005) 324.

[24] S.L. Semiatin, V.M. Segal, R.E. Goforth, N.D. Frey, D.P. Delo, Metallurgical and Materials Transactions 30A (1999) 1425.

[25] F. Kang, J.T. Wang, Y. Peng, Materials Science and Engineering A 487 (2008) 68.

[26] K. Matsubara, Y. Miyahara, Z. Horita, T.G. Langdon, Acta Materialia 51 (2003) 3073.

[27] S. Sandlobes, M. Friak, J. Neugebauer, D. Raabe, Materials Science and Engineering A 576 (2013) 61.

[28] I. Ulacia, N.V. Dudamell, F. Galvez, S. Yi, M.T. Perez–Prado, I. Hurtado, Acta Materialia 58 (2010) 2988.

[29] A. Chapuis, J.H. Driver, Acta Materialia 59 (2011) 1986.

[30] N. Standford, K. Sotoudeh, P.S. Bate, Acta Materialia 59 (2011) 4866.

[31] S.R. Agnew, O. Duygulu, International Journal of Plasticity 21 (2005) 1161.

[32] M. Bamberger, G. Dehm, Annual Review of Materials Research 38 (2008) 505.

[33] H. Yoshinaga, R. Horiuchi, Materials Transactions JIM 4 (1963) 1.

[34] H. Yoshinaga, R. Horiuchi, Materials Transactions JIM 5 (1963) 14.

[35] A. Galiyev, R. Kaibyshev, G. Gottstein, Acta Materialia 49 (2001) 1199.

[36] J.C. Tan, M.J. Tan, Materials Science and Engineering A 339 (2003) 124.

[37] X. Yang, Y. Okabe, H. Miura, T. Sakai, Materials Science and Engineering A 535 (2012) 209.

[38] D.G. Cram, X.Y. Fang, H.S. Zurob, Y.J.M. Brechet, C.R. Hutchinson, Acta Materialia 60 (2012) 6390.

[39] Y. Lin, W. Liu, L. Wang, E.J. Lavernia, Materials Science and Engineering A 573 (2013) 197.

[40] Q. Ma, B. Li, E.B. Marin, S.J. Horstemeyer, Scripta Materialia 65 (2011) 823.

[41] L.P. Troeger, E.A. Starke Jr, Materials Science and Engineering A 293 (2000) 19.

[42] M.M. Myschlyaev, H.J. McQueen, H. Mwembela, E. Konopleva, Materials Science and Engineering A 337 (2002) 121.

[43] J.A. del Valle, O.A. Ruano, Materials Science and Engineering A 487 (2008) 473.

[44] M.R. Barnett, Journal of Light Metals 1 (2001) 167.

[45] S. Gourdet, F. Montheillet, Acta Materialia 51 (2003) 2685.

[46] T. Sakai, J.J. Jones, Acta Metallurgica 32 (1984) 189.

[47] F.J. Humphreys, M. Hatherly, Elsevier, Amsterdam (2004).

[48] J.E. Bailey, P.B. Hirsch, Proceedings of the Royal Society A 267 (1962) 11.

[49] M. Jenecek, M. Popov, M.G. Krieger, R.J. Hellmig, Y. Estrin, Materials Science and Engineering A 462 (2007) 116.

[50] B.J. Lv, J. Peng, Y.J. Wang, X.Q. An, L.P. Zhong, A.T. tang, F.S. Pan, Materials and Design 53 (2014) 357.

[51] L. Lasa, J.M. Rodriguez–Ibabe, Materials Characterization 48 (2002) 371.

[52] ASM, "Metallography, Structure and Phase Diagram", Metals Handbook 8th Edition 8 316.

[53] N. Balasubramani, U.T.S. Pillai, B.C. Pai, Journal of Alloys and Compounds 457 (2008) 118.

[54] M. Cai, D.P. Field, G.W. Lorimer, Materials Science and Engineering A 373 (2004) 65.

[55] H.J. Roven, M.P. Liu, J.C. Werenskiold, Materials Science and Engineering A 483–484 (2008) 54.

[56] T. Li, K. Zhang, X.G. Li, Z.W. Du, Y.J. Li, M.L. Ma, G.L. Shi, Journal of Magnesium and Alloys 1 (2013) 47.

[57] M. Vaseghi, A.K. Taheri, S. Hong, H.S. Kim, Materials and Design 31 (2010) 4076.

[58] X.L. Hou, Z.Y. Cao, X. Sun, L.D. Wang, L.M. Wang, Journal of Alloys and Compounds 525 (2012) 103.

[59] R. Kaibyshev, T. Sakai, F. Musin, I. Nikulin, H. Miura, Scripta Materialia 45 (2001) 1373.

[60] T.G. Langdon, Journal of Materials Science 44 (2009) 5998.

[61] Glossary of terms used in metallic superplastic materials, Japanese Industrial Standard, JIS H7007, 1995.

[62] R.B. Figueiredo, T.G. Langdon, Scripta Materialia 61 (2009) 84.

[63] T.G. Langdon, Metallurgical Transactions 13A (1982) 689.

[64] R.B. Figueiredo, T.G. Langdon, Advanced Engineering Materials 10 (2008) 37.

[65] V.N. Chuvil'deev, T.G. Nieh, M.Yu. Gryaznov, A.N. Sysoev, V.I. Kopylov, Scripta Materialia 50 (2004) 861.

[66] G. Ben Hamu, D. Eliezer, L. Wagner, Journal of Alloys and Compounds 468

(2009) 222.

[67] B. Chen, D.L. Lin, L. Jin, X.Q. Zeng, C. Lu, Materials Science and Engineering A 483-484 (2008) 113.

[68] X. Liu, R. Wu, Z. Niu, J. Zhang, M. Zhang, Journal of Alloys and Compounds 541 (2012) 372.

[69] Y. Miyahara, Z. Horita, T.G. Langdon, Materials Science and Engineering A 420 (2006) 240.

[70] M. Kawasaki, T.G. Langdon, Journal of Materials Science 42 (2007) 1782.

[71] R.B. Figueiredo, T.G. Langdon, Journal of Materials Science 45 (2010) 4827.

[72] T.G. Langdon, Journal of Materials Science 44 (2009) 5998.

[73] T.G. Nieh, J. Wadsworth, O.D. Sherby, Superplasticity in Metals and Ceramics, Cambridge University Press, Cambridge (1997).

[74] R.Z. Valiev, Materials Science and Engineering A 59 (1997) 234.

[75] O.D. Sherby, J. Wadsworth, Progress in Materials Science 33 (1989) 169.

[76] X. Wu, Y. Liu, Scripta Materialia 46 (2002) 269.

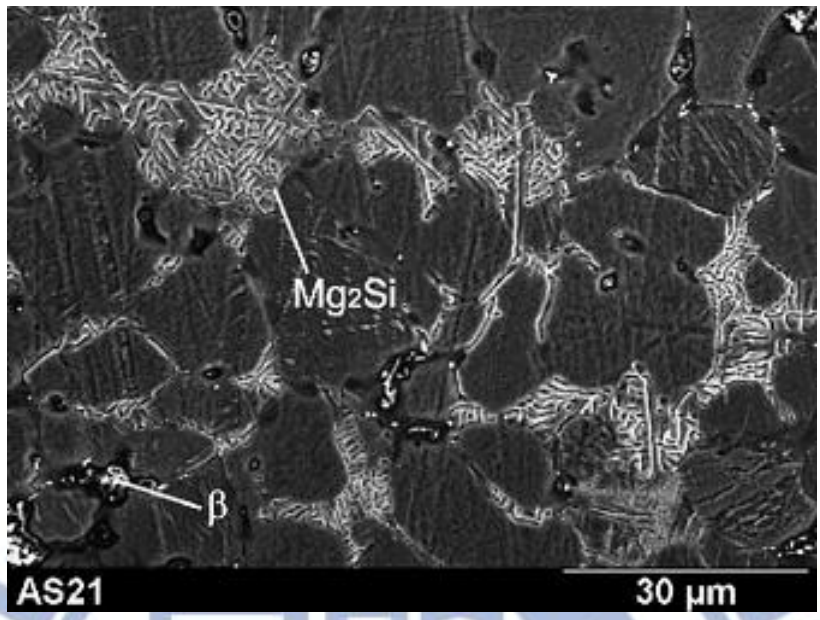

Figure 2.1. Microstructure of the AS21 alloy [1].

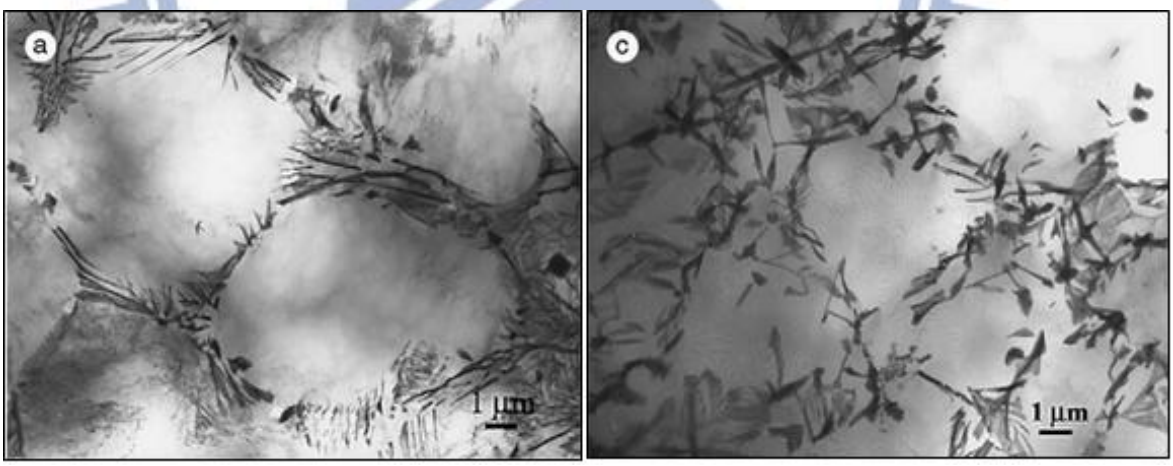

Figure 2.2. Microstructure of the AE42 alloy [4].

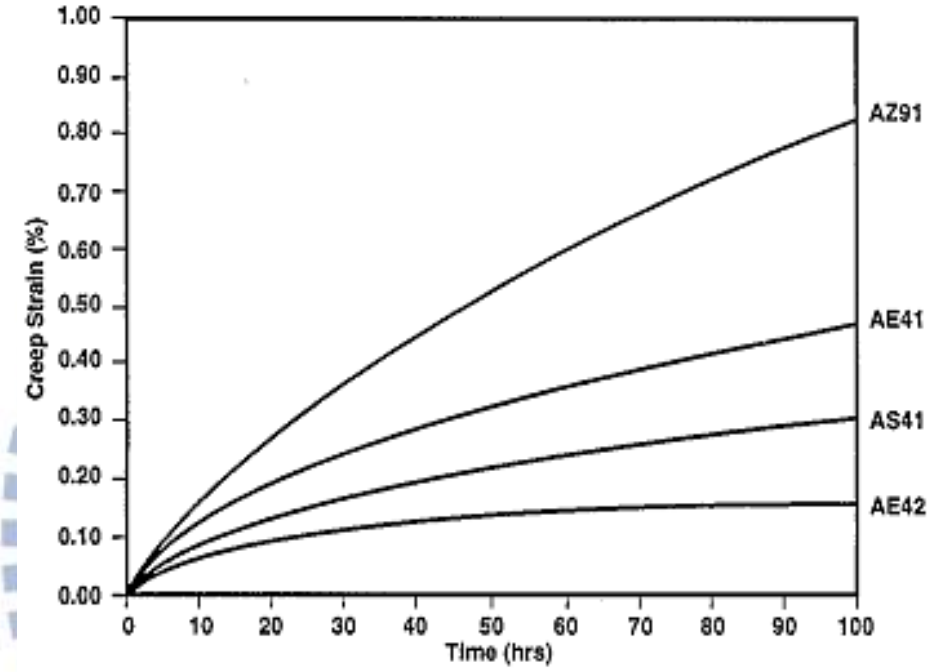

Figure 2.3. Creep properties of the AE42, AE41, AS41, and AZ91 alloys [5].

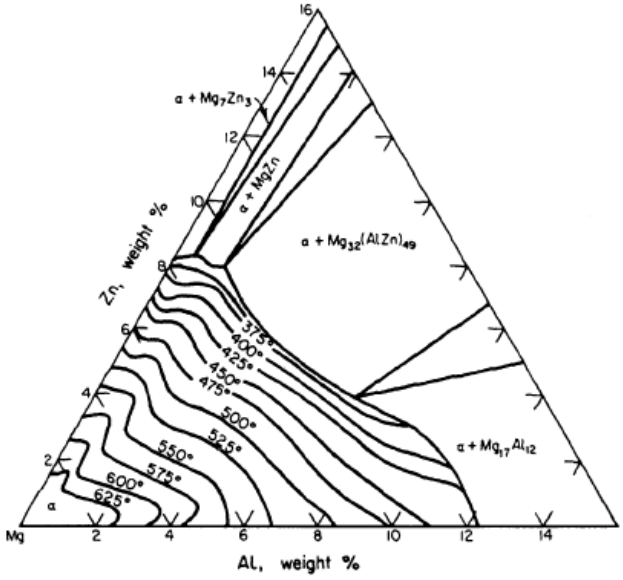

Figure 2.4. Ternary phase diagram of Mg–Zn–Al alloy.

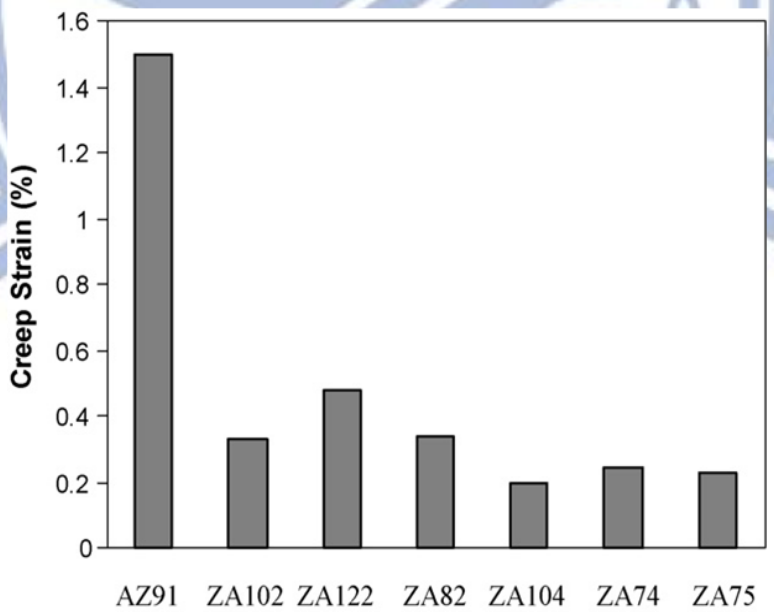

Figure 2.5. Creep behaviors between the AZ91 and ZA–series magnesium alloys [9].

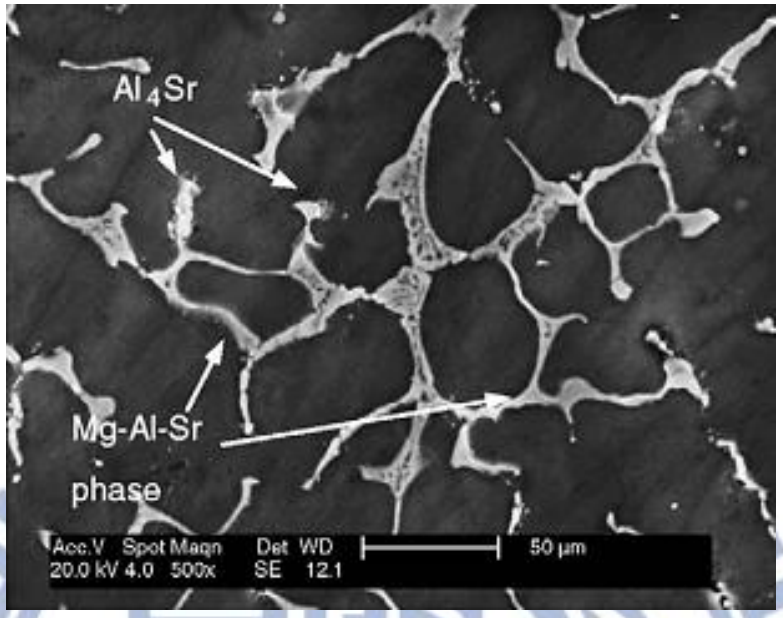

Figure 2.6. Microstructure of the AJ43 alloy [10].

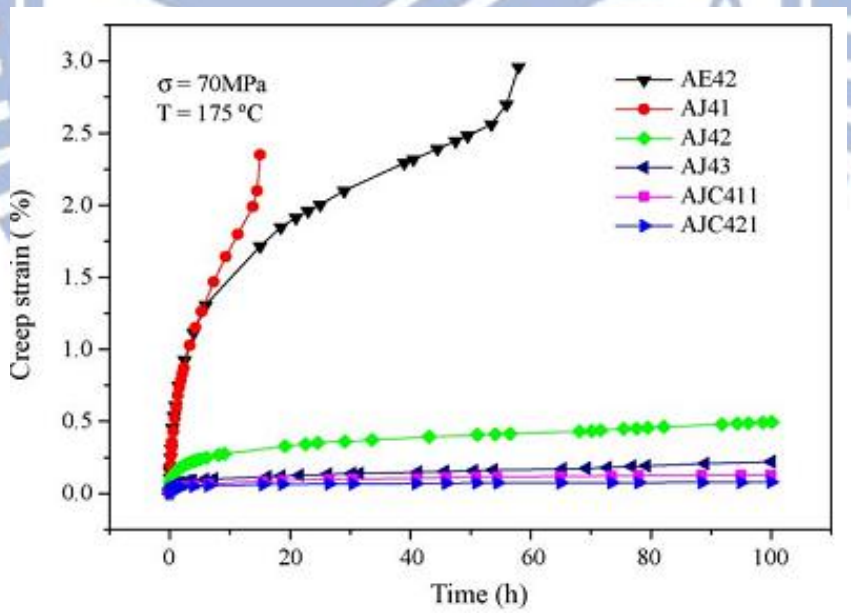

Figure 2.7. Creep behaviors of Mg–Al–Sr and Mg–Al–Sr–Ca alloys [10].

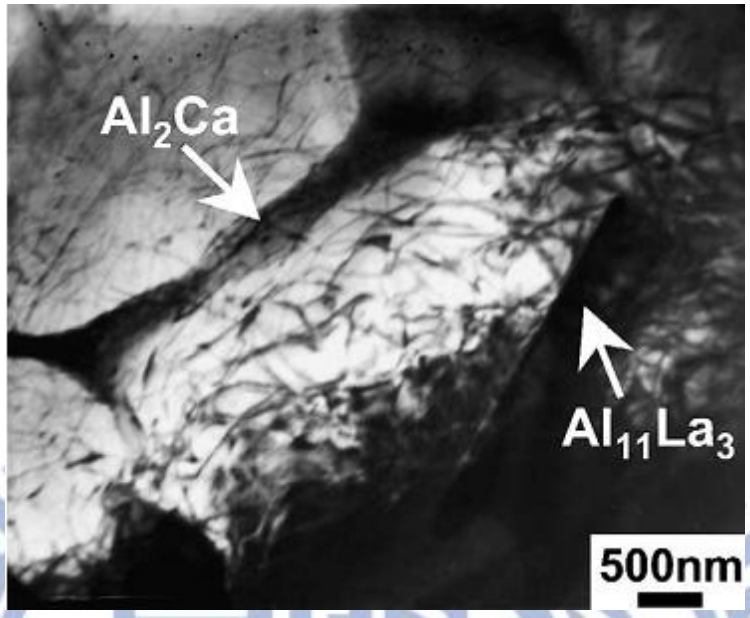

Figure 2.8. Microstructure of the Mg–Zn–Al–Ca–RE alloy [13].

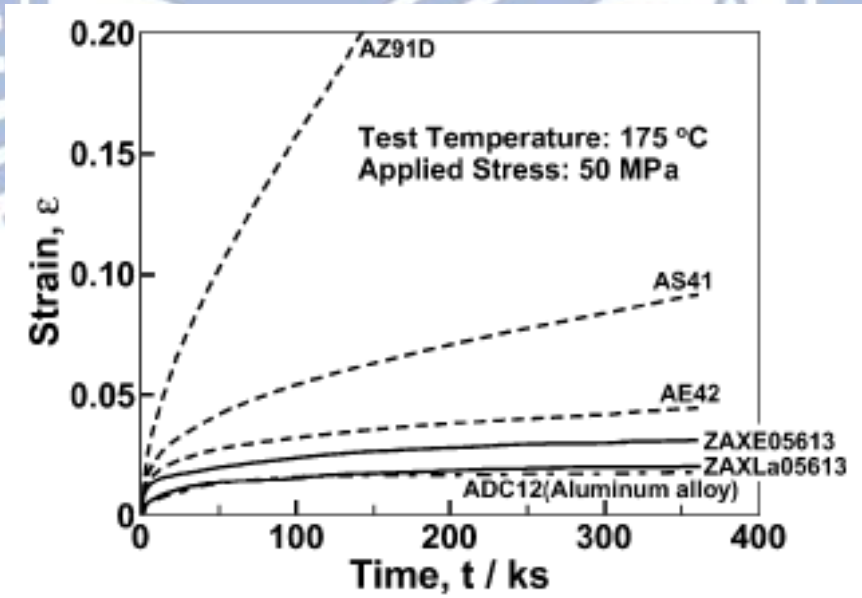

Figure 2.9 Creep behaviors between As41, AE42, and Mg–Zn–Al–Ca–RE alloys [13].

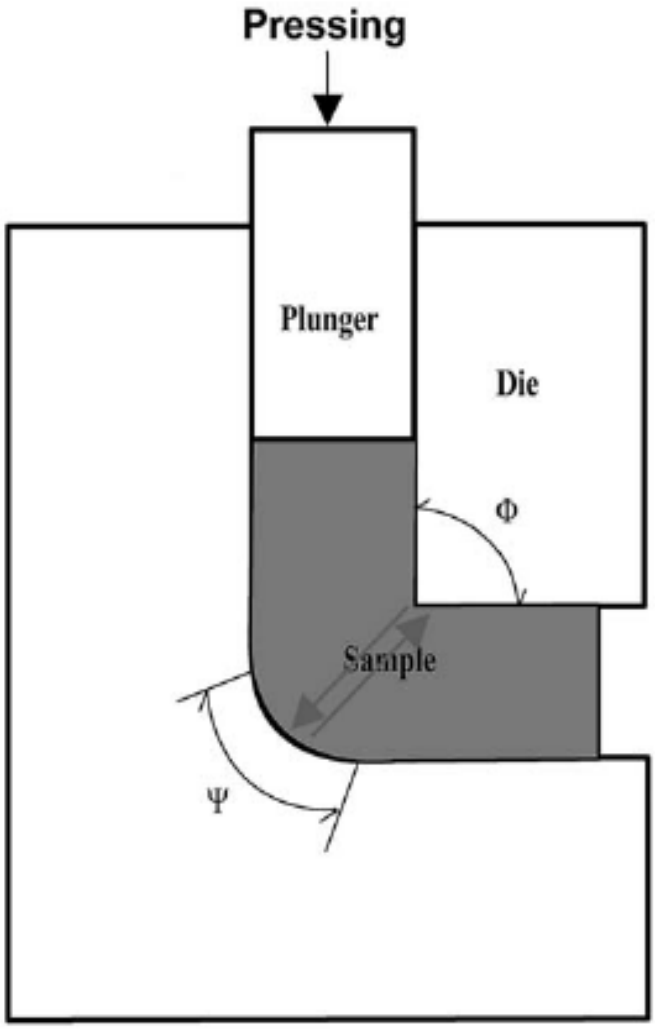

Figure 2.10. The cross–sectional figure of the ECAE die [15].

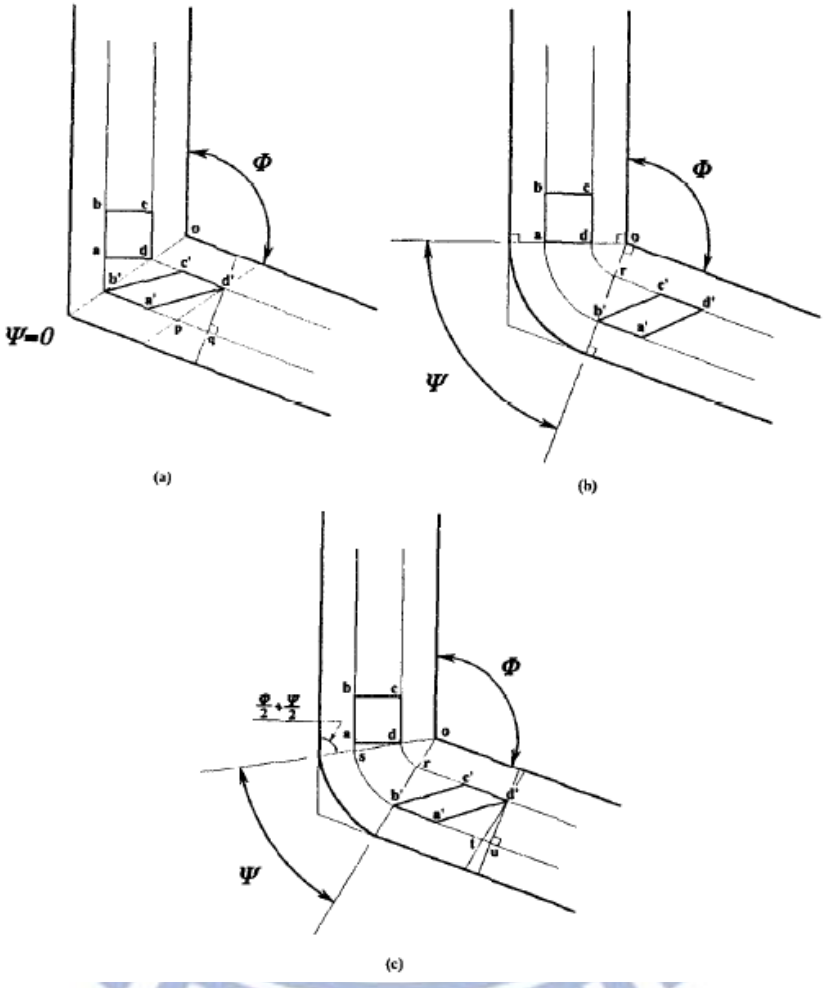

Figure 2.11. Three types of die–angle combination in the ECAE–die design [16].

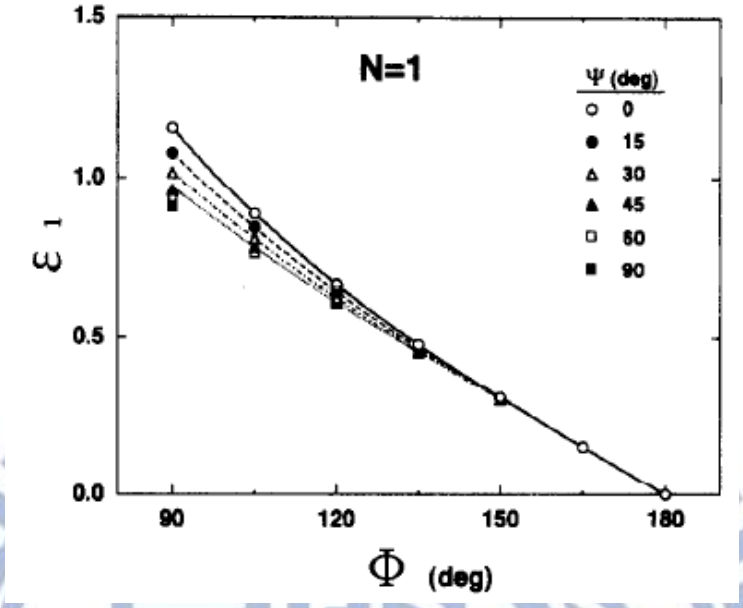

Figure 2.12. The relationship between the amount of accumulated strain and die angles of Φ and Ψ [17].

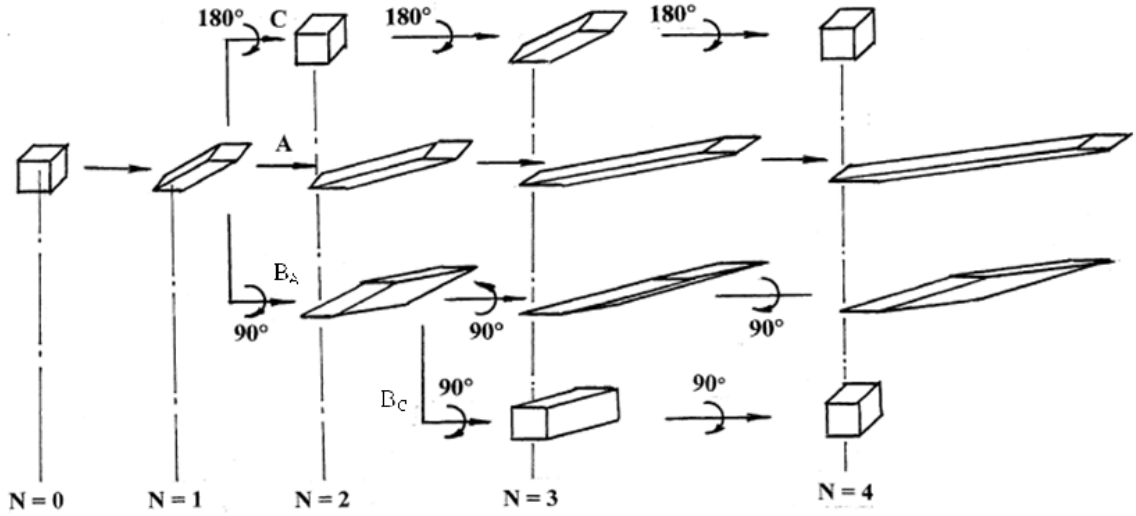

Figure 2.13. Four types of ECAE routes [18].

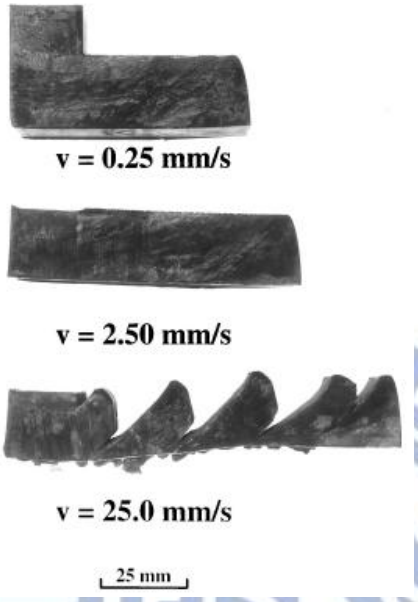

Figure 2.14. Appearance of the 4340 steel subjected to the ECAE process at 350 ℃ with different pressing rates [24].

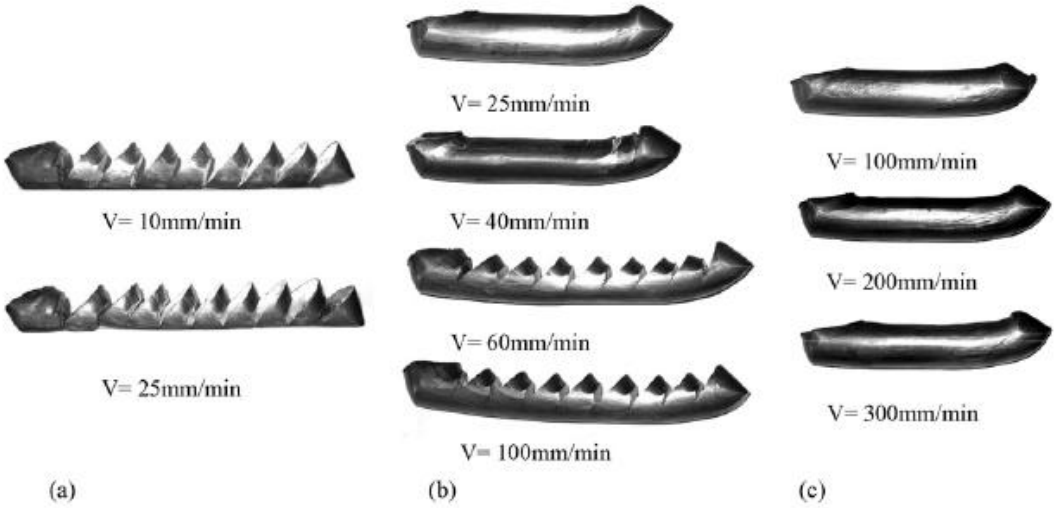

Figure 2.15. Appearance of the AZ31 alloy subjected to the ECAE process with different temperatures and pressing rates [25].

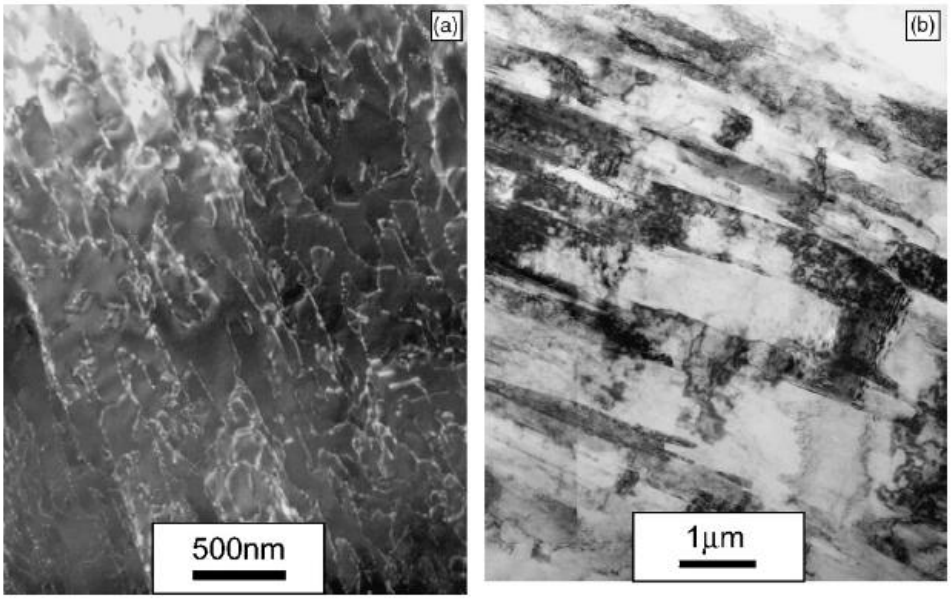

Figure 2.16. Microstructure of the as–cast AZ31 alloy after one ECAE pass, (a) dislocation: $\vec{b}=[1\bar{2}10]$, $\vec{g}=[\bar{1}011]$, and (b) subgrain: $\vec{b}=[1\bar{2}10]$, $\vec{g}=[10\bar{1}0]$ [49].

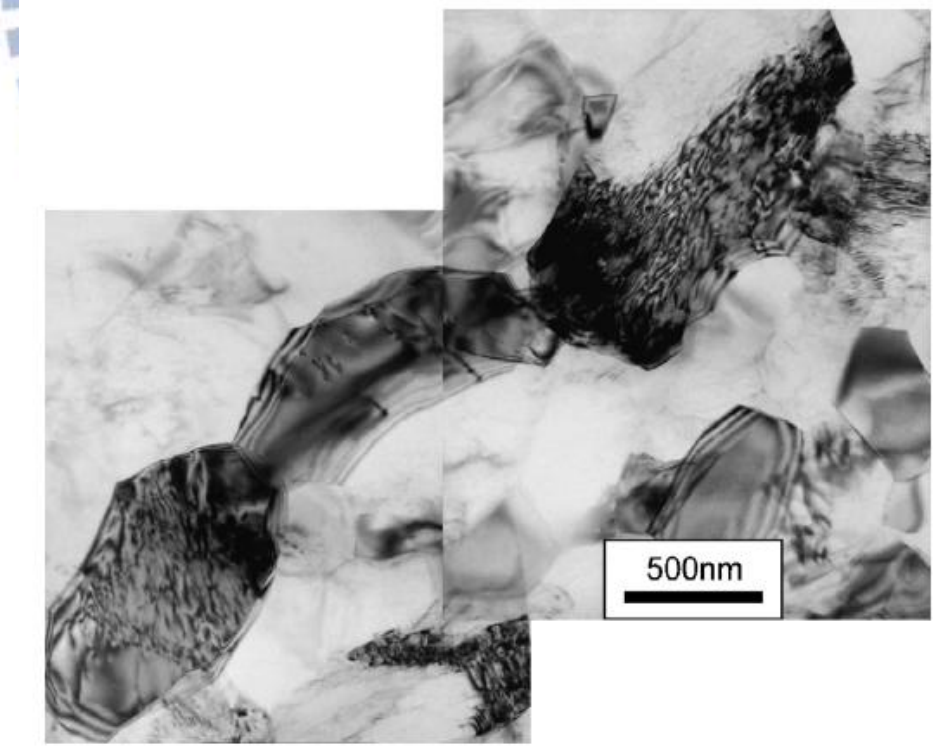

Figure 2.17. Microstructure of the as–cast AZ31 alloy after four ECAE passes [49].

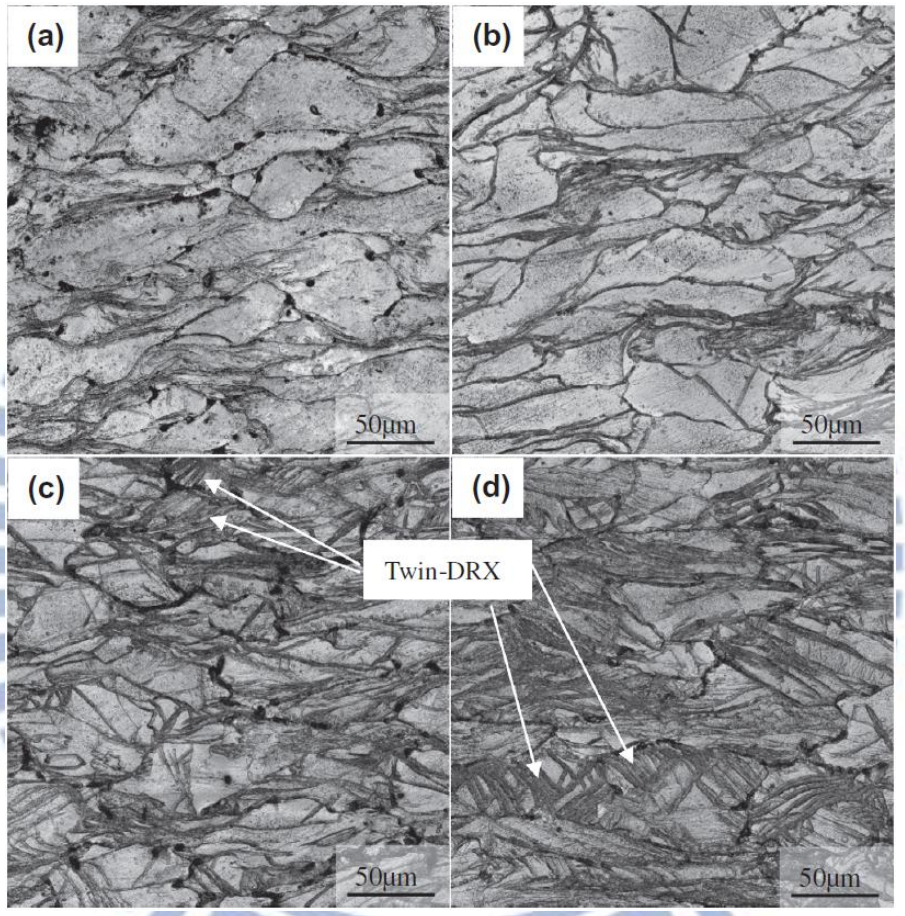

Figure 2.18. Microstructures of the compressed Mg–2.0 Zn–0.3 Zr– 0.9 Y alloy at 250 ℃ with different strain rates (a) 0.001 s^{-1}, (b) 0.01 s^{-1}, (c) 0.1 s^{-1}, and (d) 1 s^{-1} [50].

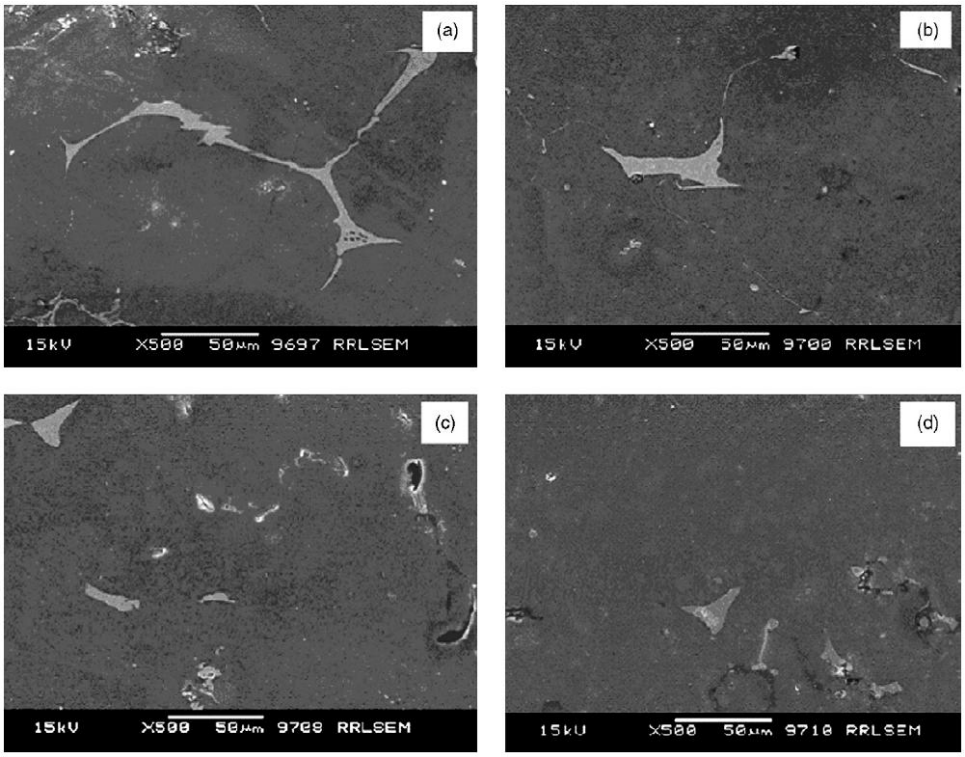

Figure 2.19. SEM micrograph of the ZA84 alloy subjected to the SHT for (a) 24 h, (b) 48 h, (c) 72 h, and (d) 100 h [53].

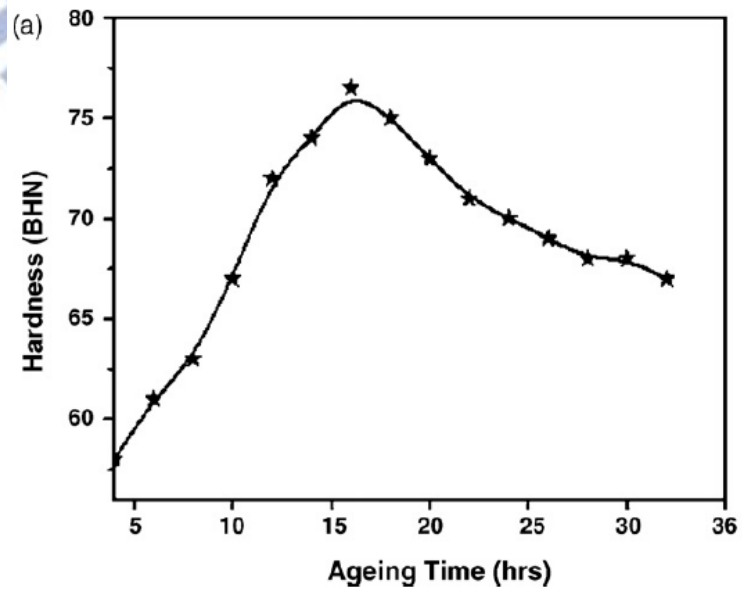

Figure 2.20. Hardness vs. aging time of the ZA84 alloy after the T6 treatment [53].

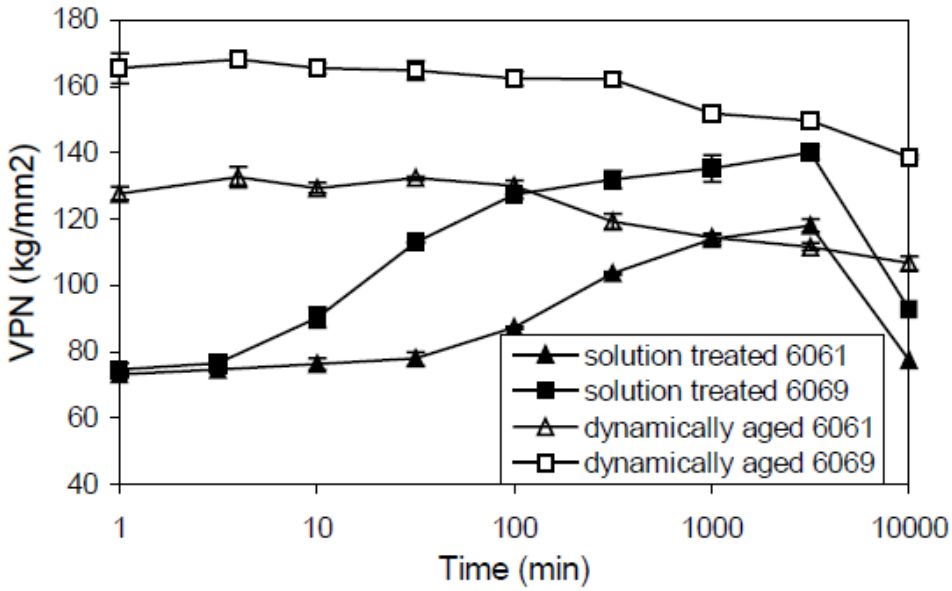

Figure 2.21 (a) A comparison of aging characteristics of the dynamically aged and the as–solutionised samples at 170 ℃ [54].

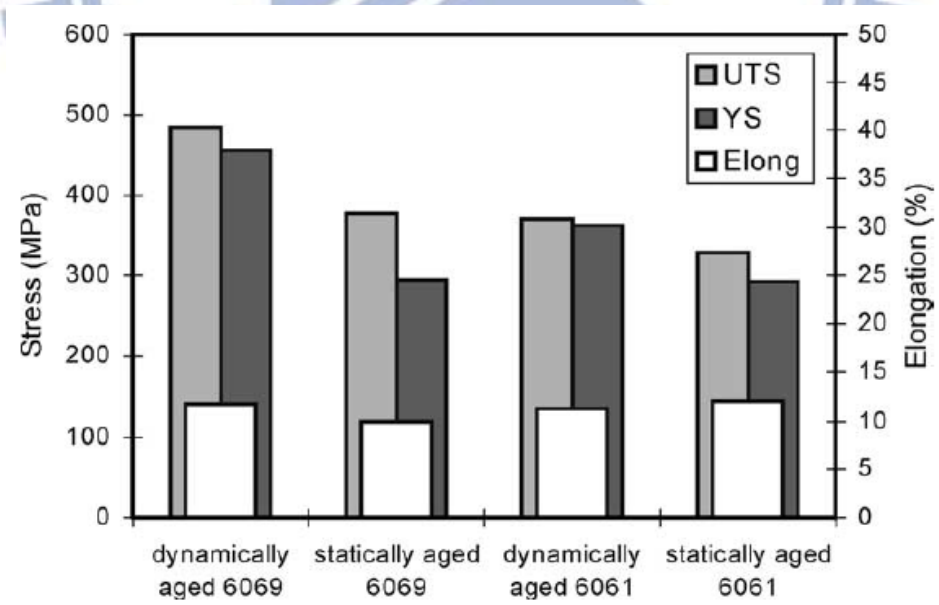

Figure 2.21 (b) Tensile properties of the 6069 and 6061 alloys after dynamic aging and static peak–aging at 170 ℃ [54].

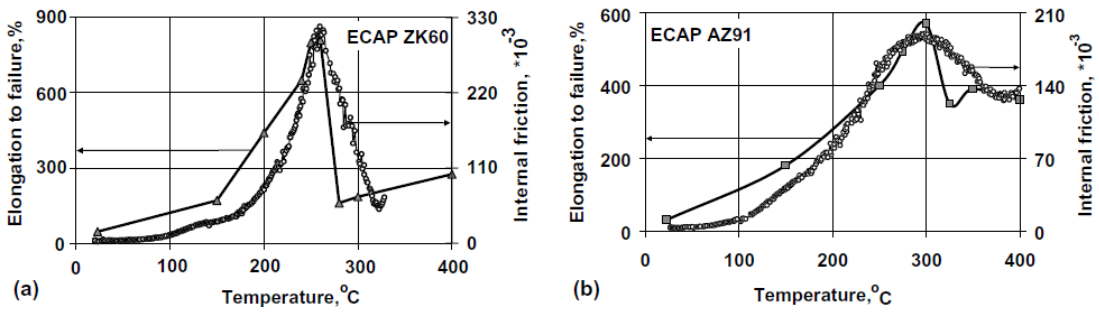

Figure 2.22. Comparison of elongation to failure as a function of deformation temperature in the (a) ZK60 and (b) AZ91 alloys [65].

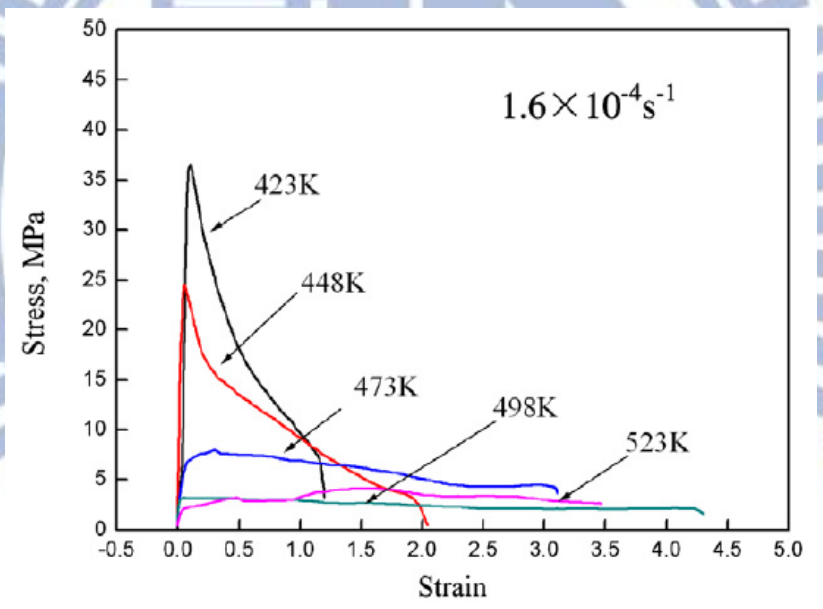

Figure 2.23. The tensile stress–strain curves of the as–rolled LZ82 alloy [68].

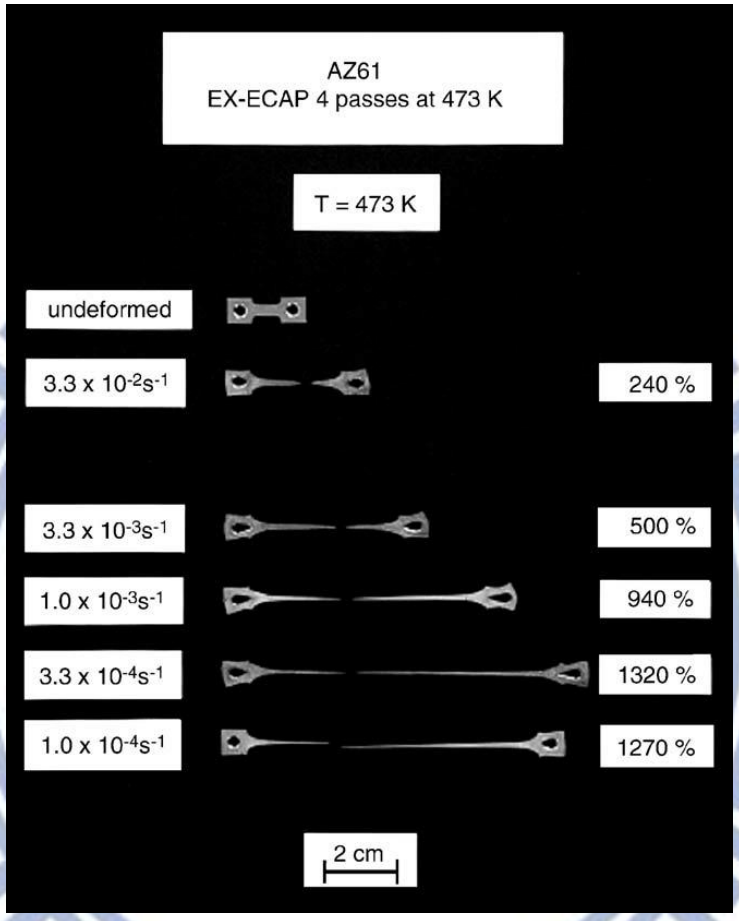

Figure 2.24. Appearance of the tensile specimens after four ECAE passes at 200 ℃ and pulling to failure at 200 ℃; the upper specimen is untested [69].

Chapter 3 Effects of Equal–Channel Angular Extrusion on the Microstructure and Tensile Properties of the ZA85 Magnesium Alloy

3.1 Introduction

In recent years, the development of magnesium alloys, which generally have excellent properties such as low density, high specific strength, superior damping capacity, high thermal conductivity, and good electromagnetic shielding characteristics, has been attracting much attention [1–4]. These properties make magnesium alloys suitable for a broad range of applications in electronic devices and the aircraft and automobile industries among others. Among various magnesium alloys, Mg–Al–Zn (AZ) alloys are widely used because of their desirable mechanical properties, corrosion resistance, and castability. However, the application of these alloys is limited at temperatures above 120 ℃. This is because their heat resistance is inferior to that of aluminum alloys at high temperatures [5]. This phenomenon is attributed to the presence of intermetallic $Mg_{17}Al_{12}$ (β–phase), which mainly precipitates along grain boundaries and exhibits a low decomposition temperature of approximately 470 ℃. Thus, grain boundary sliding occurs even at temperatures below 150 ℃ [6,7]. It has been reported that the addition of rare earth (RE) elements to magnesium improves its properties at elevated temperatures [8–10]. However, the use of Mg-RE alloys is limited owing to their inferior ductility and the high cost of RE elements. Another way to improve the high–temperature performance of AZ alloys is to suppress the formation of the β–phase [11]. It has been reported that a ternary addition of a large amount of zinc to binary Mg–Al alloys, with a Zn:Al

composition of approximately 2:1, can completely suppress the formation of the β–phase [12,13]. The main precipitate of Mg–Zn–Al (ZA) alloys is $Mg_{32}(Al,Zn)_{49}$ (τ–phase), which has a higher melting point and decomposition temperature than the β–phase [14]; therefore, ZA alloys exhibit better properties at elevated temperatures compared with commercial AZ alloys.

Another disadvantage of commercial magnesium alloys is their poor formability and low ductility at room temperature (RT) as a result of their hexagonal close-packed (HCP) crystal structure, which limits their practical applications. Microstructure refinement is a promising method to increase the ductility and strength of magnesium alloys. Severe plastic deformation (SPD) has been introduced in materials processing to produce ultrafine-grained microstructures [15]. Equal–channel angular extrusion (ECAE) is one of the most popular SPD methods and can produce a homogeneous submicron or nanocrystalline microstructure in bulk materials [16,17]. A block with two intersecting channels that have identical cross sections is used as an ECAE die. Severe deformation occurs via simple shear in the zone where the two channels intersect. Large amounts of strain can accumulate by repeated pressing because the channel cross sections are identical. ECAE is proven to be effective in refining grains in various magnesium alloys, resulting in improved ductility, strength, and superplasticity [18–22].

ECAE research on Mg alloys has focused mainly on AZ alloys. The effects of ECAE on ZA alloys, which have better high-temperature properties compared with AZ alloys, have not been investigated yet. Therefore, we investigate the microstructure and tensile properties of the as–cast ZA85 alloy after ECAE via route B_C [23] at 180, 220, and 250 ℃.

3.2 Experimental Procedures

The experimental alloy was prepared from commercially pure Mg, Al, and Zn (>99.9%). A steel crucible and an electron resistance furnace were used for melting and alloying with SF_6 as the protective atmosphere. Steel molds were used for casting the alloy. The as–cast alloy was air cooled from the molten state. The chemical composition of the experimental alloy was determined by energy dispersive spectroscopy (EDS). The results of chemical analyses were averaged over three different regions that were chosen randomly from the ingot. The chemical composition of the alloy is 8.34 wt.% Zn, 4.74 wt.% Al with the balance Mg, as shown in Table 3.1. For ECAE, specimens of dimensions 17 mm × 17 mm × 60 mm were cut from the ingot, and an ECAE die with an angle of 120° was used. Boron nitride was used as the lubricant during ECAE. The ECAE die was preheated to 180, 220, and 250 ℃ and maintained for 15 min before inserting a lubricated ECAE specimen into the entrance channel. All specimens were held inside the ECAE die for 5 min before pressing. These specimens were processed via route B_C in which after each pass, the specimen was rotated through 90° in the same direction at a pressing speed of 2 mm/min. Microstructures of the as–cast and ECAE materials were examined by standard metallographic procedures. The polished surface was etched with 3 mL acetic acid solution, 5 mL deionized water, 35 mL ethanol, and 1 g picric acid. The microstructures were observed by optical microscopy, scanning electron microscopy (SEM), and transmission electron microscopy (TEM). Regarding the ECAE specimens, the surfaces perpendicular to ND (y–plane) were observed [24]. The average grain size, grain size distribution, and area fraction of grain size were obtained with Image Pro software (IpWin32). A Rockwell indenter with a load of 100 kgf was used for a Rockwell hardness B (HRB) test at RT. The HRB values were averaged over 10 tests under each set of conditions. The ECAE specimens were

longitudinally cut to obtain tensile specimens with a gauge section of 6 mm × 3 mm × 2 mm. Tensile tests were conducted at RT and 200 ℃ with an initial strain rate of $1 \times 10^{-3}\ s^{-1}$ using an Instron 8501 universal testing machine. A furnace mounted on the machine was used for high–temperature tensile tests. The specimens were heated to 200 ℃ and then held for 10 min prior to the tensile tests. Ultimate tensile strength (UTS), yield strength (YS), and elongation were averaged over three to five tests under each set of conditions.

3.3 Results and Discussion

The optical micrograph of the as–cast ZA85 alloy shows an equiaxed grain structure with an average grain size of approximately 150 μm, as shown in Fig. 3.1. The coarse precipitates, identified as the τ–phase by X–ray diffraction (the same as in previous literature [12,14,25]), are distributed along the grain boundaries, as shown in Fig. 3.2. The chemical composition of matrix and τ–phase checked by EDS are shown in Table 3.2. Moreover, several defects such as blow holes and shrinkage voids are clearly observed in the as–cast specimen. These defects result from the air trapped in the melting alloy during casting and from the difference between the cooling rates in the inner and outer regions of the ingot.

Fig. 3.3 shows the optical micrographs of the ECAE–processed specimens after different number of passes were conducted at 180 ℃. After fewer than four ECAE passes, all microstructures became inhomogeneous with fine recrystallized grains along the grain boundaries and a number of large distorted grains. This resultant microstructure, termed as “bimodal,” was also observed by Chang et al. [26]. These differ from the microstructure of aluminum alloys subjected to the ECAE process. Nakashima et al. [27] reported that after two ECAE passes at RT, the microstructure of aluminum alloys became homogeneous with ultrafine grains less than 1 μm in size.

This phenomenon is attributed to the difference between the grain refinement mechanisms of magnesium and aluminum alloys. For aluminum alloys, Berbon et al. [28] proposed a grain refinement mechanism during ECAE deformation. In the first pass, several dislocations are introduced within the grain because of the applied strain. These dislocations then rearrange into low–energy dislocation structures (LEDSs). The dislocations generated in the following passes then transform the LEDSs into subgrains. With increasing number of ECAE passes, boundary misorientation would increase to form high–angle grain boundaries. However, the grain refinement mechanism of magnesium alloys by ECAE is mainly dynamic recrystallization [29, 30] because of the relatively few slip systems in HCP metals during the ECAE process at testing temperatures. In HCP metals, the slip system at RT is mainly the basal slip system. At high temperatures, non–basal slip systems such as prismatic and pyramidal slip systems can become activated. However, in this study, ECAE processing temperatures are below 250 ℃, which is not high enough to activate all non–basal slip systems [31]. Therefore, dynamic recrystallization is responsible for grain refinement. From the TEM micrograph shown in Fig. 3.4, it can be observed that after six ECAE passes at 180 ℃, there are several dislocation–free grains attributable to dynamic recrystallization. The density of dislocation increases owing to the large amount of strain accumulated by the repetition of ECAE processes. Then, dynamic recrystallization occurs in the area of high dislocation density, producing numerous fine grains and reducing dislocation density. It should be noted that the microstructures exist in a preferential orientation after one, two, and six passes but not after four passes. In this study, because ECAE is conducted via route B_C, in which the specimen is rotated 90° in the same direction after each pass, the grain structure would return to an equiaxed structure after every four passes.

Fig. 3.5 shows the area fraction of grain sizes for the ECAE–processed

specimens. As can be observed in Fig. 3.5(a), the area fraction of fine grains (less than 10 μm) increased with the number of ECAE passes at 180 ℃. This indicates that the area fraction of dynamically recrystallized grains progressively increased with strain. In addition, the area fraction of large grains apparently decreased with subsequent passes. This suggests that ECAE can result in a uniform microstructure. Furthermore, defects such as blow holes and shrinkage voids in the as–cast specimen were eliminated after the ECAE process, as shown in Fig. 3.3.

The SEM micrographs (Fig. 3.6) show the effect of ECAE on the precipitates. The precipitate size reduced with increasing number of ECAE passes. After four passes, the size was significantly reduced to less than 10 μm. After six passes, it was further reduced to an average of 1 μm with uniform distribution. This proves that ECAE not only reduces grain size but also shatters coarse precipitates. In general, the precipitates shattered by shear stress during the ECAE process ought to have an irregular shape and a rough surface. In this study, the ECAE process is conducted at high temperatures with a low pressing speed; hence, the precipitate surface becomes smoother to reduce surface energy.

Figs. 3.7 and 3.8 show the optical micrographs of the ECAE–processed specimens after different number of passes at 220 and 250 ℃, respectively. Compared to the results at the lower ECAE temperature of 180 ℃, the degree of dynamic recrystallization increased with ECAE temperature so that a more uniform microstructure was obtained at higher temperatures. Figs. 3.7(c) and 3.8(c) show that the microstructures obtained after four ECAE passes at 220 and 250 ℃ were more uniform than those at 180 ℃. These new fine grains grew slightly during the ECAE process at 220 and 250 ℃. This indicates that a higher temperature is more beneficial for dynamic recrystallization. Therefore, the degree of dynamic recrystallzation increases with ECAE temperature, leading to much more uniform microstructures at

higher ECAE temperatures with the same number of ECAE passes. The area fraction of grains less than 10 μm in size reached 80% after six passes at 180 ℃. On the other hand, most of the dynamically recrystallized grains had grown to 10–20 μm during ECAE at 220 ℃, as shown in Fig. 3.5(b). The area fraction of grains of sizes 10–20 μm was approximately 1.5% after one pass and increased to approximately 14.5% and 44% after two and four passes, respectively. After ECAE at 250 ℃, grain growth was more evident. In particular, most of the dynamically recrystallized grains had grown to sizes 20–30 μm, as shown in Fig. 3.5(c). Furthermore, the area fraction of grains with sizes 20–30 μm increased to approximately 38% after four passes.

Fig. 3.9 shows the average grain size with different number of ECAE passes at different temperatures. It can be observed that the degree of grain refinement increased with ECAE temperature after one pass. The average grain sizes of the specimens were 31, 19, and 16 μm after one pass at 180, 220, and 250 °C, respectively. However, the grain refinement rate decreased with additional passes at 220 ℃. Note that the average grain size increased from 14 μm after two passes to 20 μm after four passes at 250 ℃. In contrast, at the lower ECAE temperature of 180 ℃, the average grain size reduced to 8 μm after four ECAE passes. It was further reduced to 4 μm after six ECAE passes without conspicuous grain growth.

Fig. 3.10 shows that hardness increases with the number of ECAE passes, which can be attributed to two factors. The first one is grain refinement. As can be observed in Figs. 3.9 and 3.10, a smaller grain size is accompanied by greater hardness. The second factor is the shattered precipitates. These uniformly distributed fine precipitates would hinder grain boundary sliding as well as dislocation slips, which leads to better mechanical properties. After six ECAE passes at 180 ℃, hardness increased significantly from HRB 19 to HRB 46.

Fig. 3.11 shows the results of the tensile tests on the ZA85 alloy conducted at RT.

The trend of the tensile properties is similar to the trend of the hardness properties. For the as-cast specimen, UTS was 175 MPa at RT. After one ECAE pass at 180, 220, and 250 ℃, UTS increased to 187, 198, and 220 MPa, respectively. It can be observed that ECAE temperature varies directly with the strength of the alloy. In addition, UTS and YS increased with additional ECAE passes at 180 and 220 ℃ but decreased with increasing number of ECAE passes from two to four; this is owing to the grain growth effect at 250 ℃. At 180, 220, 250 ℃, the UTS of the four–pass ECAE–processed specimens were 373, 348, and 242 MPa, respectively. At 180 ℃, the UTS of the six–pass ECAE–processed specimens reached 402 MPa. Compared with those of the as–cast ZA85 alloy, the UTS and YS at RT were improved by up to 230% and 215%, respectively. The tensile properties at RT in the present study are also superior to those of many other AZ series alloys that were subjected to ECAE, as shown in Table 3.3 [18,29,32,33].

Fig. 3.11(c) shows that the elongation of the present alloy at RT was improved by ECAE. After six passes at 180 ℃, the elongation of the alloy improved from 2.3% to approximately 6.4%. This increment in elongation is attributed to (1) the elimination of defects such as blow holes and shrinkage voids formed during casting, as shown in Fig. 3.3, and (2) precipitate refinement. It is worth mentioning that after four ECAE passes, the average grain size at 180 ℃ is smaller than that at 250 ℃, whereas elongation is higher in the latter case. This phenomenon can be attributed to the degree of dynamic recrystallization during ECAE. As can be observed in Fig. 3.3(c), after four ECAE passes at 180 ℃, the microstructure is rather inhomogeneous with fine recrystallized grains as well as a number of large initially distorted grains. On the other hand, the microstructure is more uniform with fully recrystallized grains after four ECAE passes at 250 ℃, as shown in Fig. 3.8(c). Therefore, the dislocation density would be considerably reduced by the high degree of recrystallization in the

latter case, thereby leading to a material with higher ductility.

Fig. 3.12 shows the results of the high–temperature tensile tests conducted at 200 ℃. The trend of the high–temperature tensile properties is similar to the trend of the RT properties. The UTS and YS of six–pass ECAE–processed specimens increased to 249 and 162 MPa at 200 ℃, respectively. Compared with the 105 and 74 MPa values of the as–cast ZA85 alloy, the UTS and YS at 200 ℃ were improved by up to 229% and 210%, respectively. Note that the high–temperature tensile properties of the ZA85 alloy in the present study are superior to those of other high–temperature magnesium alloys, as shown in Table 3.4 [34]. In addition, elongation increased to 28.5% in the tensile test at 200 ℃ after six ECAE passes at 180 ℃. The high–temperature tensile properties of materials are influenced by several factors such as average grain size and precipitate size as well as their distribution. In this study, the improvement in high-temperature tensile properties is mainly attributed to the refined grains and precipitates. After the ECAE process, both coarse grains and precipitates with initial sizes greater than 100 μm are considerably refined to less than 10 μm. According to the deformation mechanism map of pure magnesium, the high–temperature deformation of the present experimental condition could be termed as dislocation glide. Therefore, we assume that the deformation of the ZA85 alloy during the high–temperature tensile tests is dislocation glide. Consequently, the refined grains less than 10 μm in size would hinder dislocation to improve the high–temperature properties. Moreover, the precipitates also play an important role in improving the high–temperature properties. The refined precipitates uniformly distributed at grain boundaries hinder grain boundary migration. The precipitate of the ZA85 alloy is the τ–phase instead of the β–phase. The τ–phase has a higher decomposition temperature than the β–phase. Therefore, the significant improvement in the high–temperature tensile properties of the ZA85 alloy after ECAE is ascribed to

the well–distributed τ–phase.

3.4 Summary and Conclusions

The effects of ECAE on the microstructure and tensile properties of the ZA85 magnesium alloy were examined, and some interesting findings were obtained.

1. The grain size under the as–cast condition (about 150 μm) was significantly reduced to 4 μm after six ECAE passes at 180 ℃. On the other hand, the average grain size of the ECAE–processed specimens at 250 ℃ increased from 14 μm after two passes to 20 μm after four passes owing to the grain growth effect. At first, the microstructure was not uniform, showing a "bimodal" grain size distribution; however, it became more homogeneous with further ECAE passes.
2. The hardness at RT increased with the number of ECAE passes; this can be attributed to grain refinement and the shattered precipitates that were distributed uniformly in the material. Furthermore, hardness increased from HRB 19 to HRB 46 after six passes at 180 ℃.
3. The precipitate size was significantly reduced, from an average of 100 μm to 1 μm, with increasing number of ECAE passes and uniform distribution was obtained after six passes.
4. In RT tensile tests, the UTS, YS, and elongation of the as–cast ZA85 alloy were 175 MPa, 130 MPa, and 2.3%, respectively. After six passes at 180 ℃, UTS, YS, and elongation increased to 402 MPa, 281 MPa, and 6.4%, respectively.
5. Tensile tests at an elevated temperature of 200 ℃ showed that the UTS, YS, and elongation of the as–cast ZA85 alloy were 105 MPa, 74 MPa, and 5.1%, respectively. After six ECAE passes at 180 ℃, UTS, YS, and elongation increased to 249 MPa, 162 MPa, and 28.5%, respectively. Moreover, the high–temperature

tensile properties of the present alloy are superior to those of many other commercial high–temperature magnesium alloys.

References

[1] D.J. Li, X.Q. Zeng, J. Dong, C.Q. Zhai, W.J. Ding, Journal of Alloys and Compounds 468 (2009) 164.

[2] M. Bamberger, G. Dehm, Annual Review of Materials Research 38 (2008) 505.

[3] X.F. Huang, W.Z. Zhang, J.F. Wang, W.W. Wei, Journal of Alloys and Compounds 516 (2012) 186.

[4] K. Liu, J. Meng, Journal of Alloys and Compounds 509 (2011) 3299.

[5] D.H. Xiao, M. Song, F.Q. Zhang, Y.H. He, Journal of Alloys and Compounds 484 (2009) 416.

[6] A. Srinivasan, U.T.S. Pillai, B.C. Pai, Metallurgical and Materials Transactions 36 A (2005) 2235.

[7] B.H. Kim, S.W. Lee, Y.H. Park, I.M. Park, Journal of Alloys and Compounds 493 (2010) 502.

[8] I.A. Anyanwu, Y. Gokan, S. Nozawa, A. Suzuki, S. Kamado, Y. Kojima, S. Takeda, T. Ishida, Materials Transactions 44 (2003) 562.

[9] J.F. Nie, K. Oh-ishi, X. Gao, K. Hono, Acta Materialia 56 (2008) 6061.

[10] D. Wu, R.S. Chen, E.H. Han, Journal of Alloys and Compounds 509 (2011) 2856.

[11] H. Liu, Y. Chen, Y. Tang, S. Wei, G. Niu, Journal of Alloys and Compounds 440 (2007) 122.

[12] Z. Zhang, A. Couture, A. Luo, Scripta Materialia 39 (1998) 45.

[13] M. Vogel, O. Kraft, E. Arzt, Scripta Materialia 48 (2003) 985.

[14] J. Zhang, Z.X. Guo, F. Pan, Z. Li, X. Luo, Materials Science and Engineering A 456 (2007) 43.

[15] Y.B. Chun, S.H. Yu, S.L. Semiatin, S.K. Hwang, Materials Science and Engineering A 398 (2005) 209.

[16] V.M. Segal, Materials Science and Engineering A 197 (1995) 157.

[17] V.M. Segal, K.T. Hartwig, R.E. Goforth, Materials Science and Engineering A 224 (1997) 107.

[18] K. Máthis, J. Gubicza, N.H. Nam, Journal of Alloys and Compounds 394 (2005) 194.

[19] H.K. Kim, Y.I. Lee, C.S. Chung, Scripta Materialia 52 (2005) 473.

[20] M. Eddahbi, P. Pérez, M.A. Monge, G.Garcés, R. Pareja, P. Adeva, Journal of Alloys and Compounds 473 (2009) 79.

[21] G. Ben Hamu, D. Eliezer, L. Wagner, Journal of Alloys and Compounds 468 (2009) 222.

[22] B. Chen, D.L. Lin, L. Jin, X.Q. Zeng, C. Lu, Materials Science and Engineering A 483-484 (2008) 113.

[23] Y. Iwahashi, Z. Horita, M. Nemoto, T.G. Langdon, Acta Materialia 46 (1998) 3317.

[24] W.J. Kim, S.I. Hong, Y.S. Kim, S.H. Min, H.T. Jeong, J.D. Lee, Acta Materialia 51 (2003) 3293.

[25] N. Balasubramani, A. Srinivasan, U.T.S. Pillai, K. Raghukandan, B.C. Pai, Journal of Alloys and Compounds 455 (2008) 168.

[26] S.Y. Chang, S.W. Lee, K.M. Kang, S. Kamado, Y. Kojima, Materials Transactions 45 (2004) 488.

[27] K. Nakashima, Z. Horita, M. Nemoto, T.G. Langdon, Acta Materialia 5 (1998) 1589.

[28] P.B. Berbon, T.G. Langdon, The Minerals, Metal & Materials society (2000) 381.

[29] M. Janeček, M. Popov, M.G. Krieger, R.J. Hellmig, Y. Estrin, Materials Science and Engineering A 462 (2007) 116.

[30] C.W. Su, L. Lu, M.O. Lai, Materials Science and Engineering A 434 (2006) 227.

[31] M.H. Yoo, S.R. Agnew, J.R. Morris, K.M. Ho, Materials Science and Engineering A 319-321 (2001) 87.

[32] K. Xia, J.T. Wang, X. Wu, G. Chen, M. Gurvan, Materials Science and Engineering A 410-411 (2005) 324.

[33] Z. Zuberova, Y. Estrin, T.T. Lamark, M. Janeček, R.J. Hellmig, M. Krieger, Journal of Materials Processing Technology 184 (2007) 294.

[34] A.A. Luo, Materials Science Forum 419-422 (2003) 57.

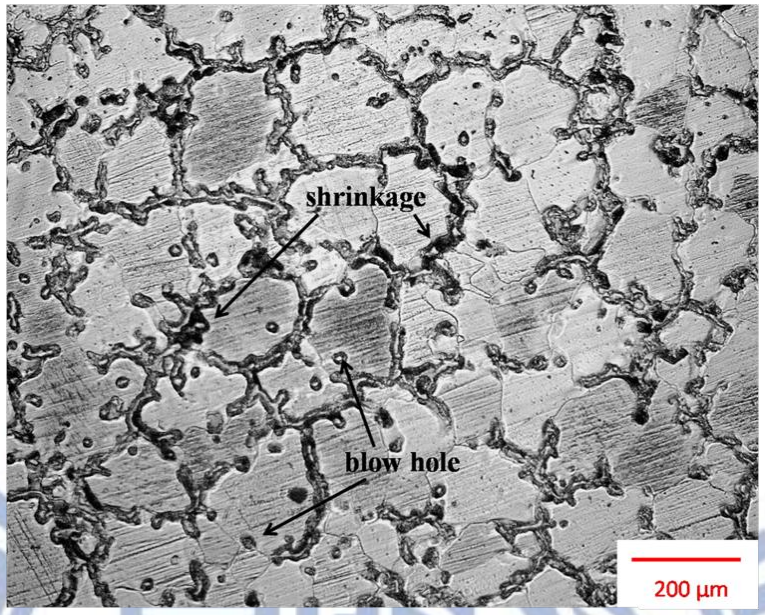

Figure 3.1 Optical micrograph of the as–cast ZA85 alloy.

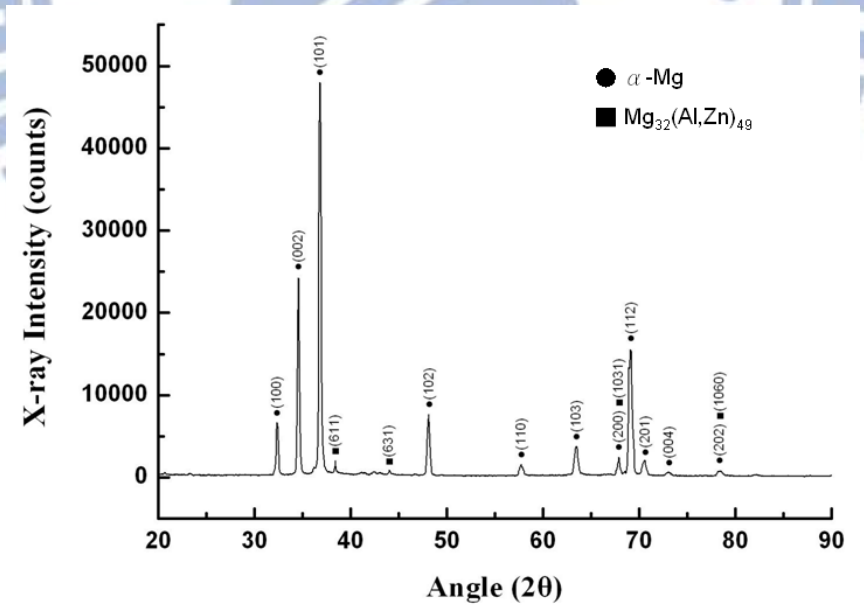

Figure 3.2 XRD analysis of the as–cast ZA85 alloy.

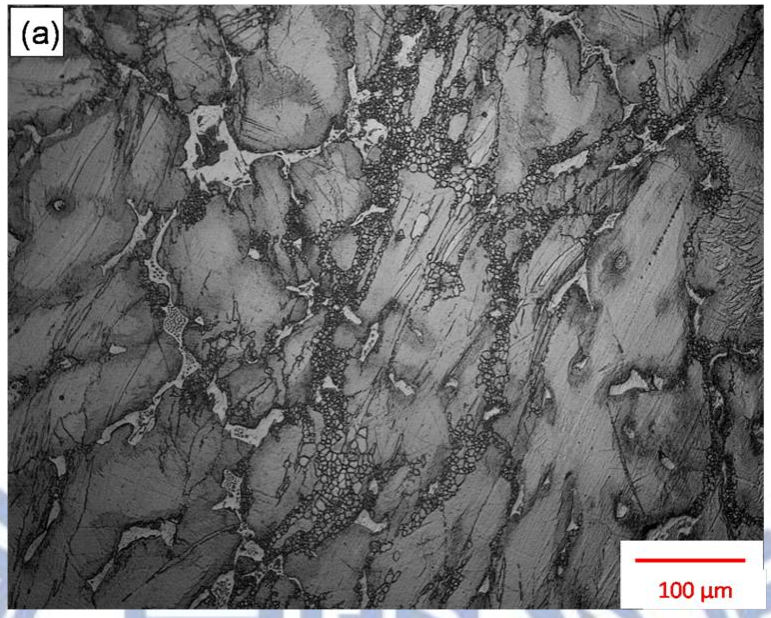

Figure 3.3 (a)

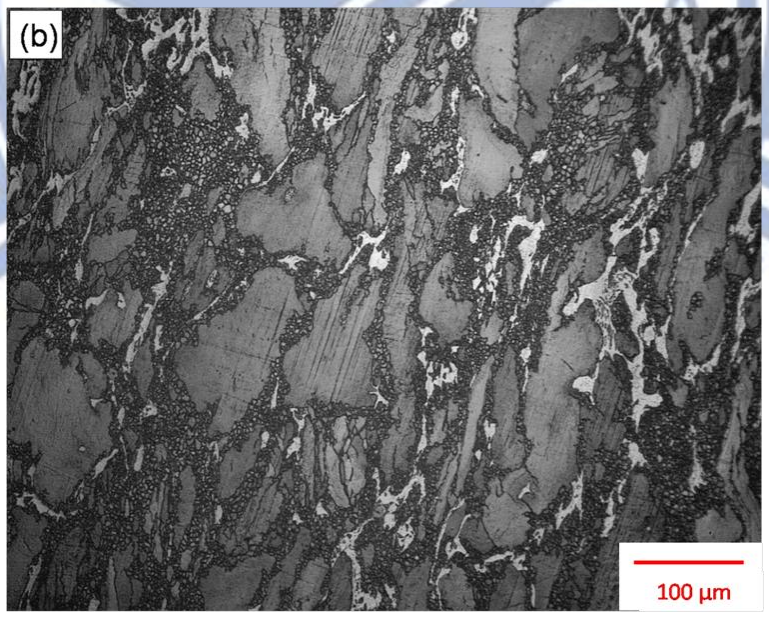

Figure 3.3 (b)

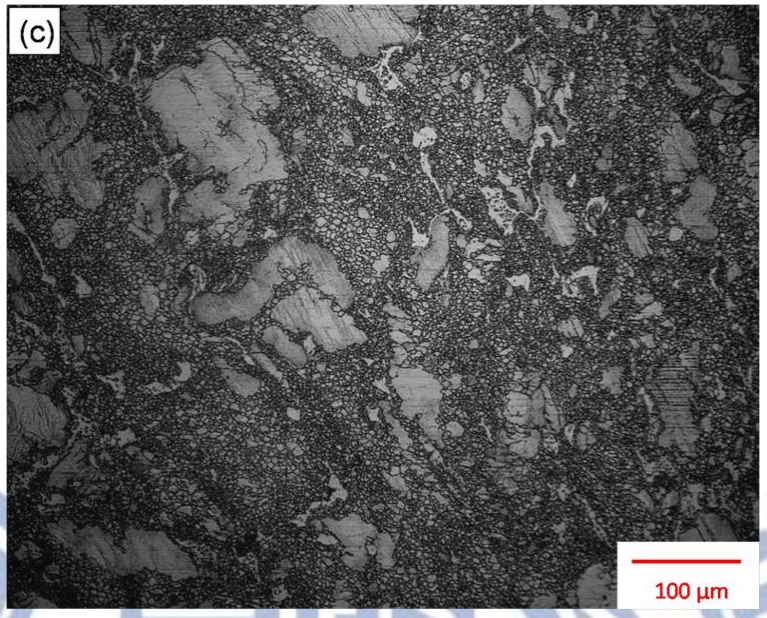

Figure 3.3 (c)

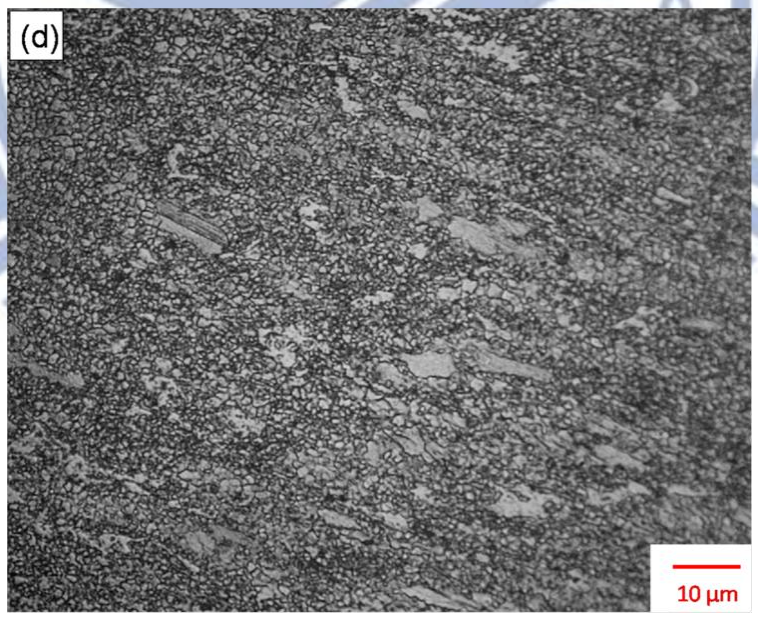

Figure 3.3 (d)

Figure 3.3 Optical micrographs of the ZA85 alloy after ECAE at 180 ℃ for (a) N = 1, (b) N = 2, (c) N = 4, and (d) N = 6.

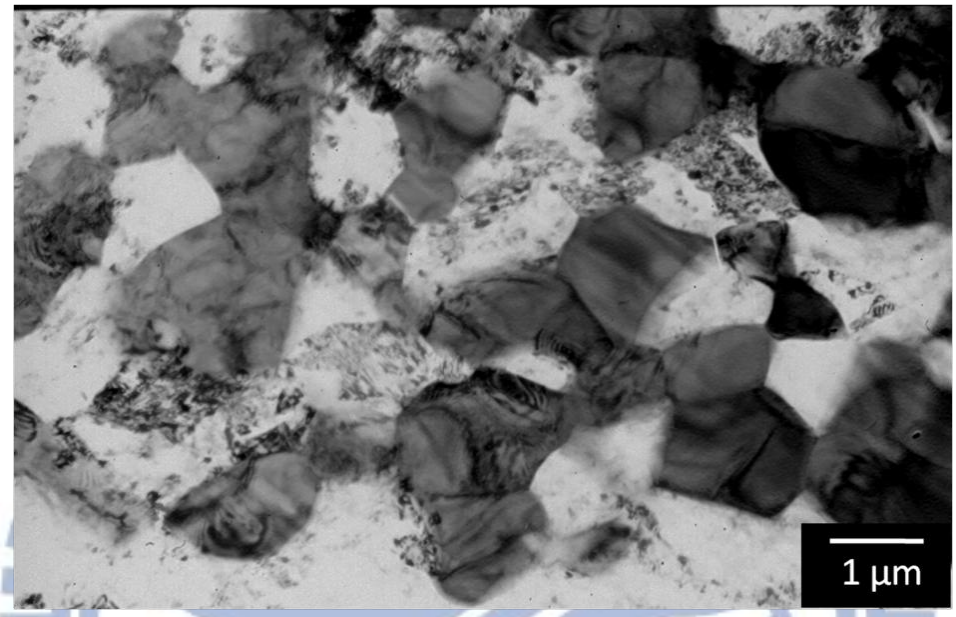

Figure 3.4 TEM micrograph of the ZA85 alloy after six ECAE passes at 180 ℃.

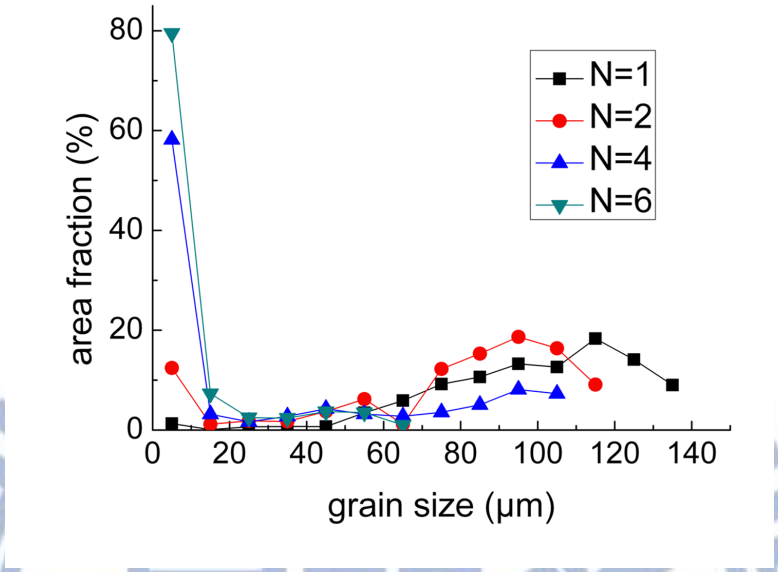

Figure 3.5 (a)

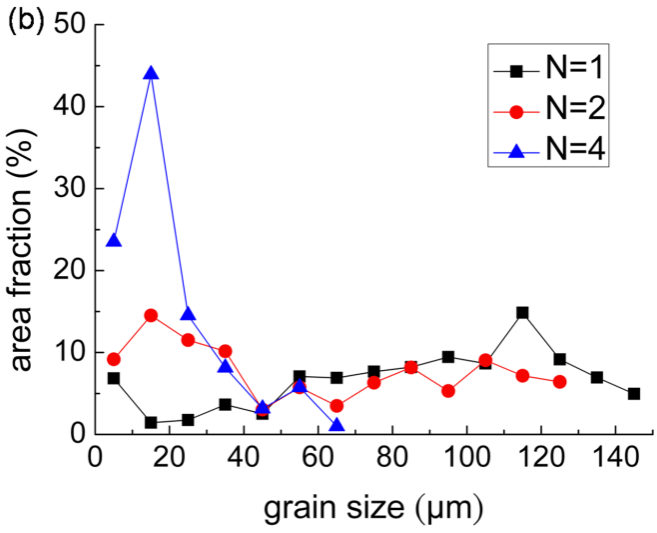

Figure 3.5 (b)

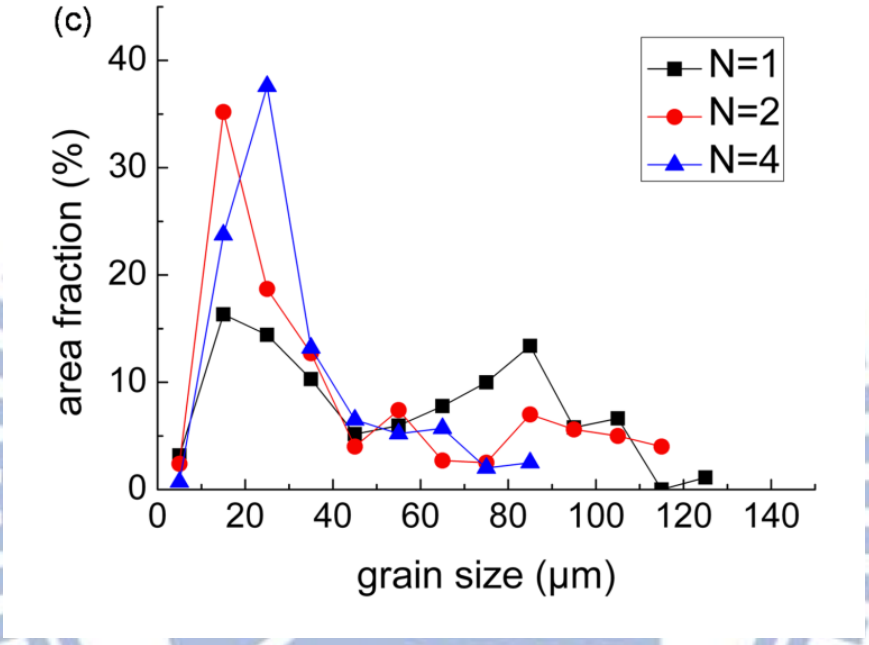

Figure 3.5 (c)

Figure 3.5 Area fraction of grains with different sizes after ECAE at (a) 180, (b) 220, and (c) 250 ℃.

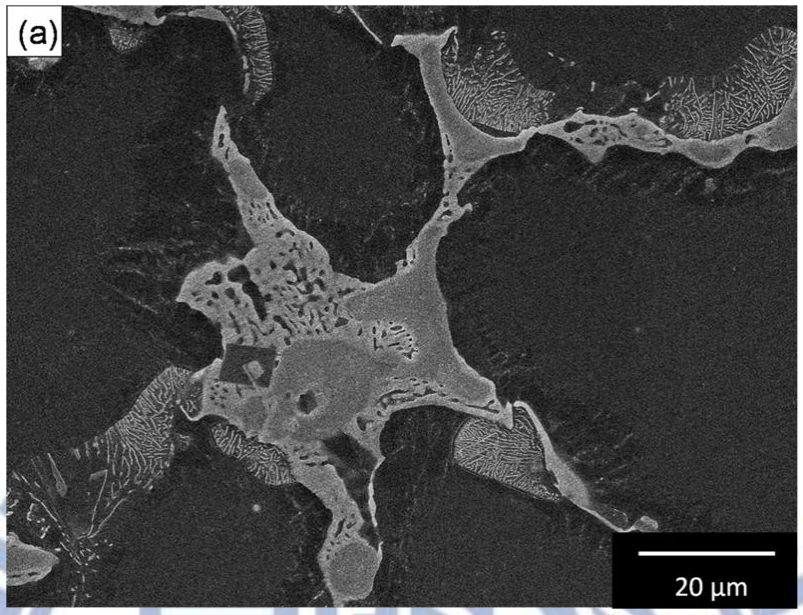

Figure 3.6 (a)

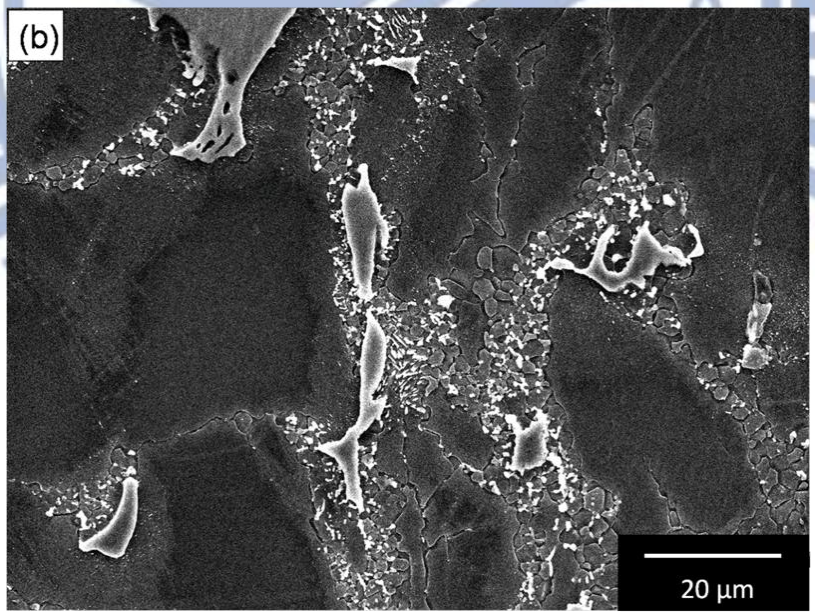

Figure 3.6 (b)

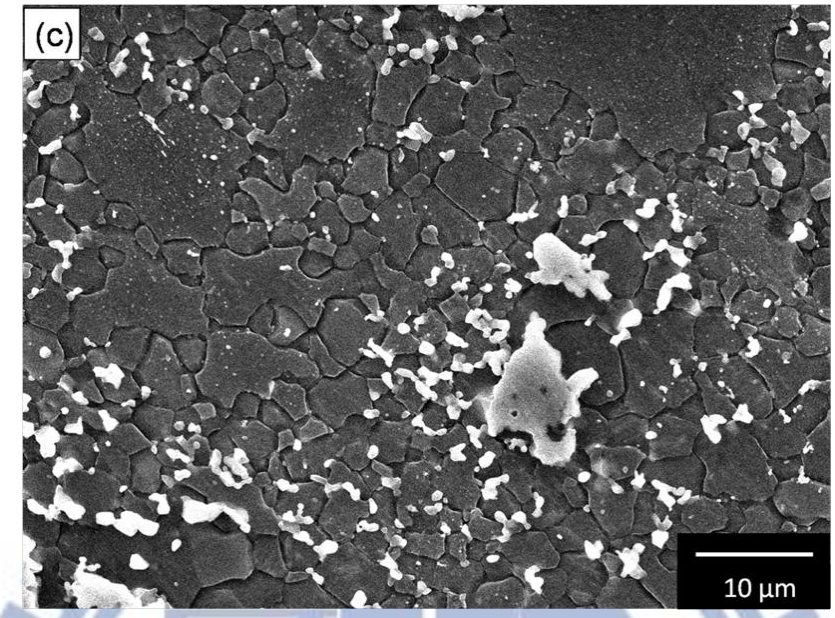

Figure 3.6 (c)

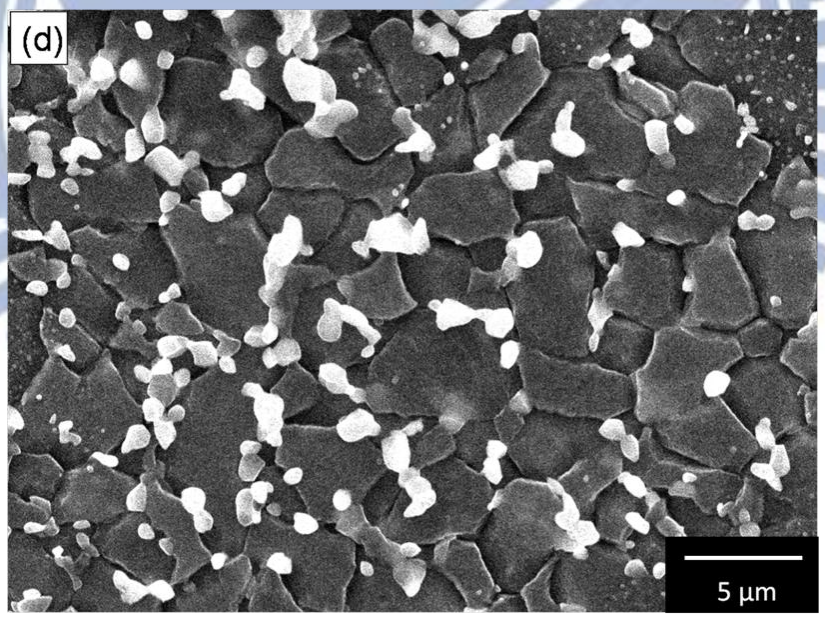

Figure 3.6 (d)

Figure 3.6 SEM micrographs of the ZA85 alloy after ECAE at 180 ℃ for (a) N = 0, (b) N = 1, (c) N = 4, and (d) N = 6.

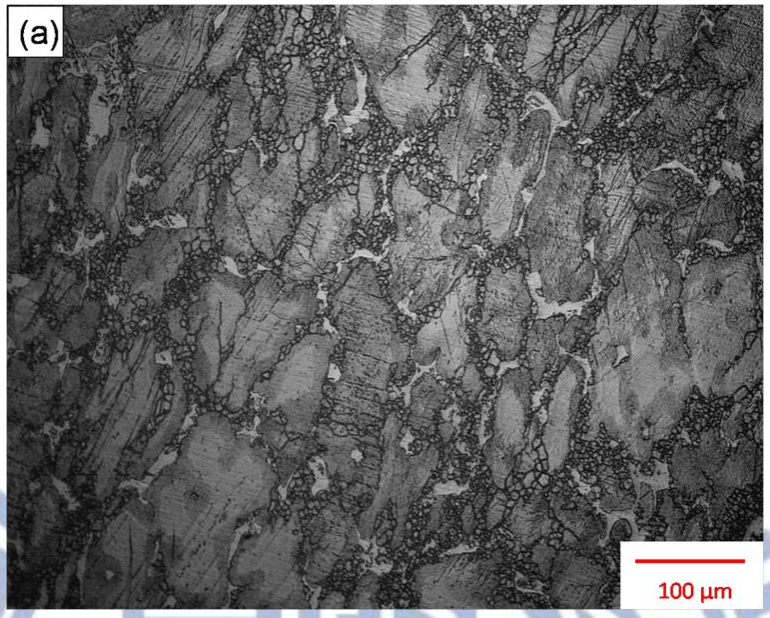

Figure 3.7 (a)

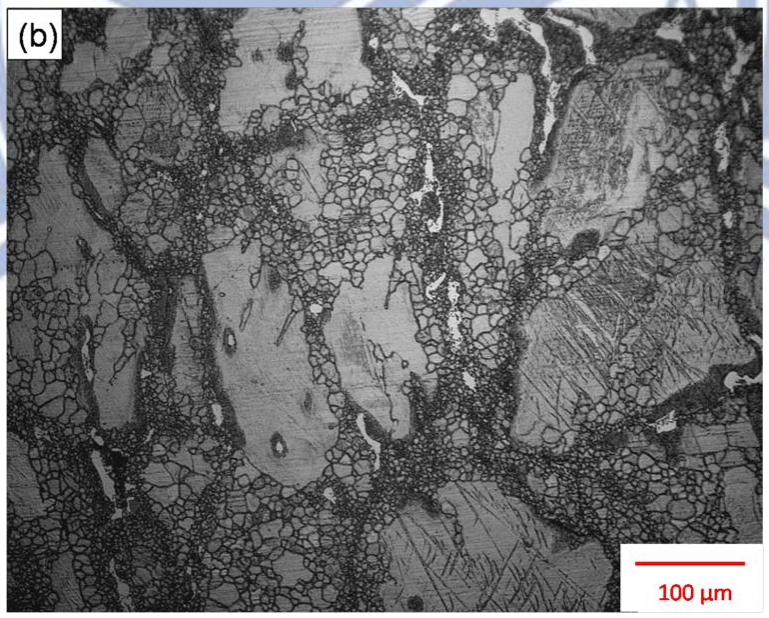

Figure 3.7 (b)

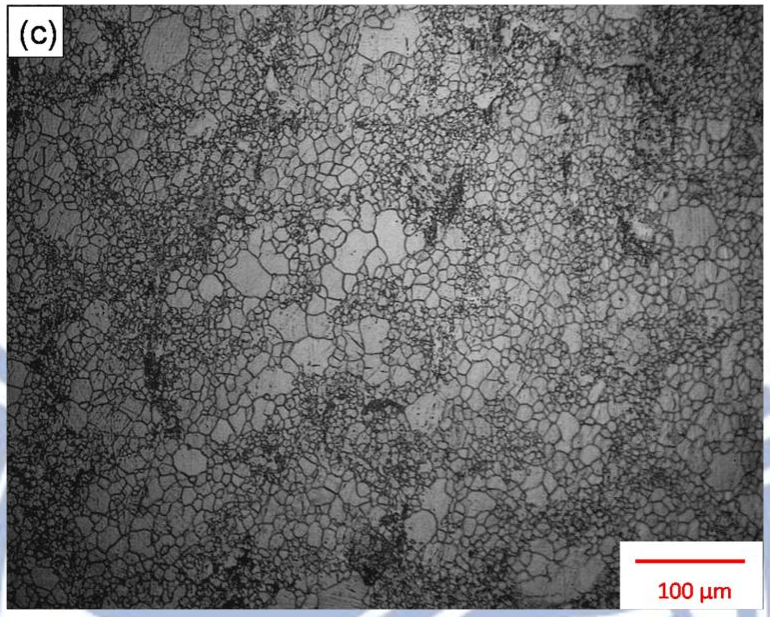

Figure 3.7 (c)

Figure 3.7 Optical micrographs of the ZA85 alloy after ECAE at 220 ℃ for (a) N = 1, (b) N = 2, and (c) N = 4.

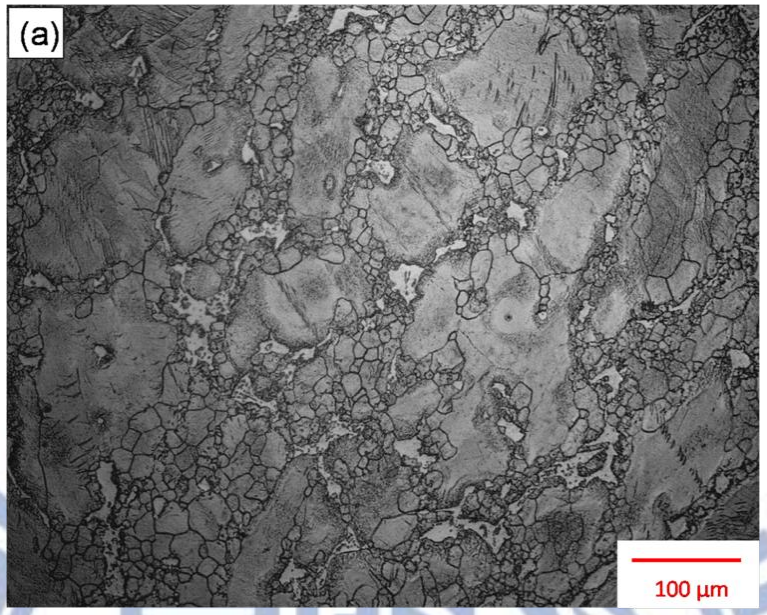

Figure 3.8 (a)

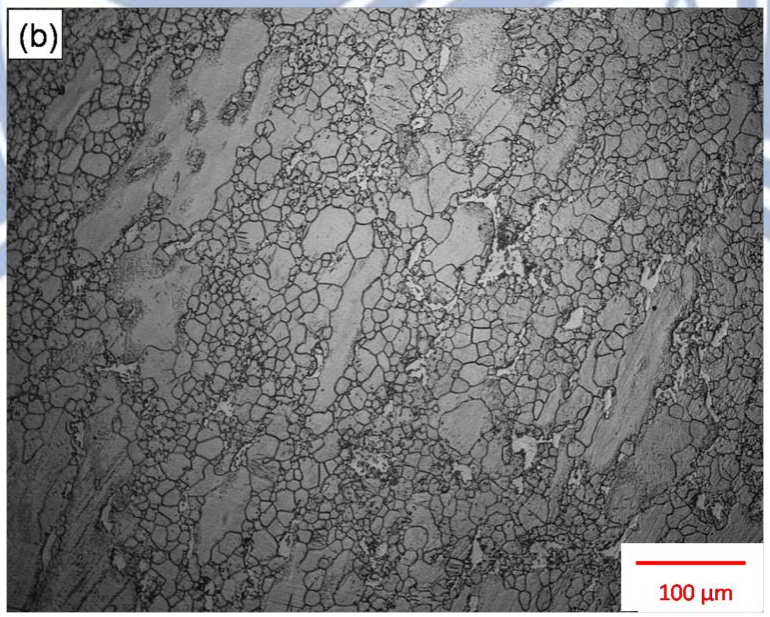

Figure 3.8 (b)

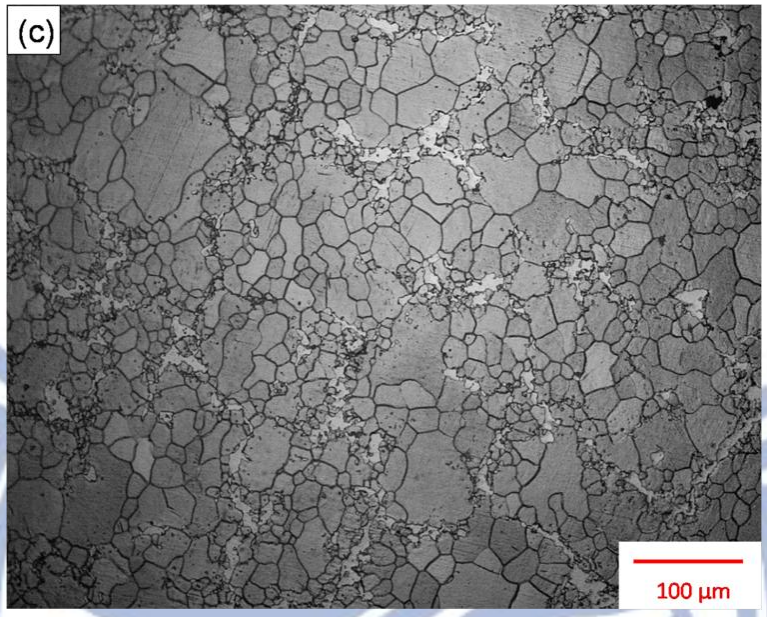

Figure 3.8 (c)

Figure 3.8 Optical micrographs of the ZA85 alloy after ECAE at 250 ℃ for (a) N = 1, (b) N = 2, and (c) N = 4.

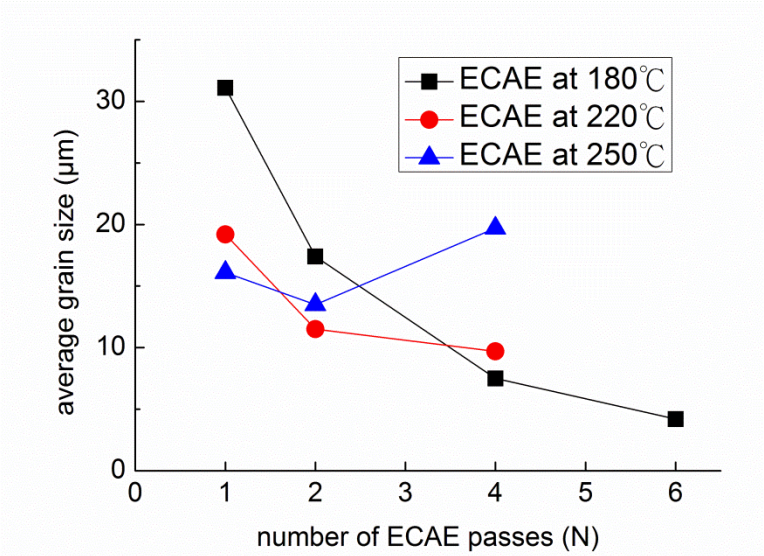

Figure 3.9 Average grain size with number of passes at different ECAE temperatures.

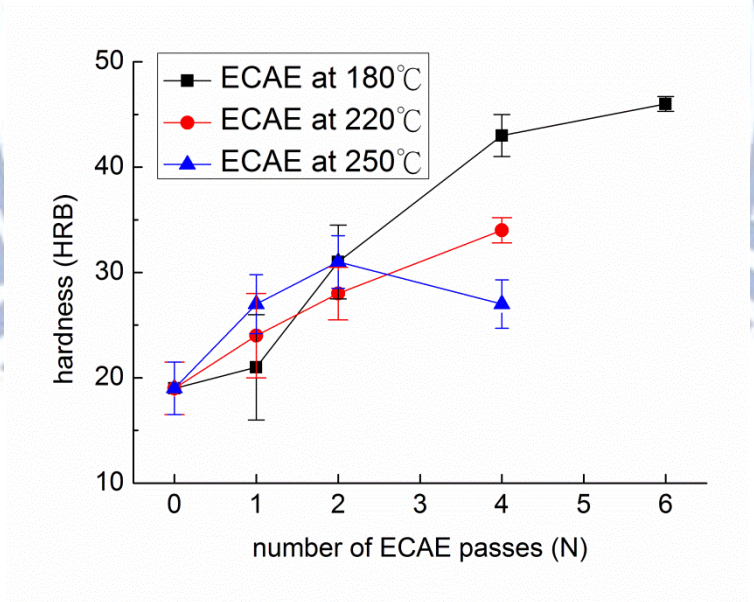

Figure 3.10 Hardness at room temperature with different number of passes at different ECAE temperatures.

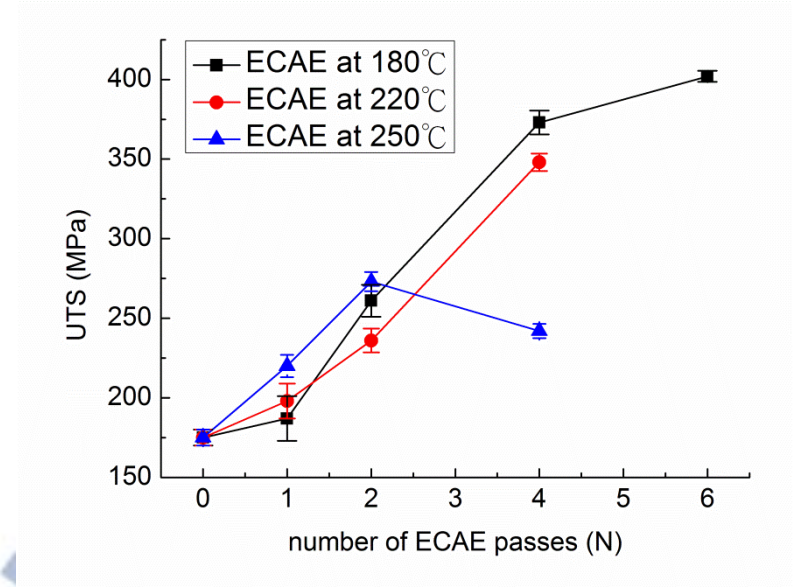

Figure 3.11 (a)

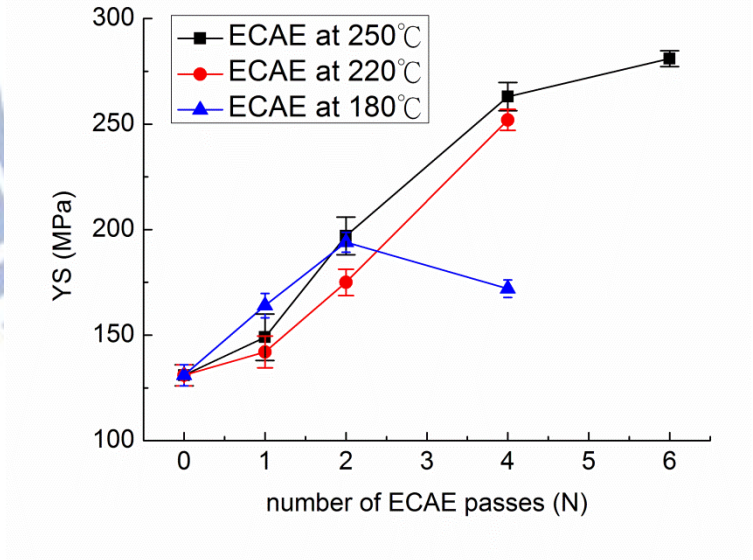

Figure 3.11 (b)

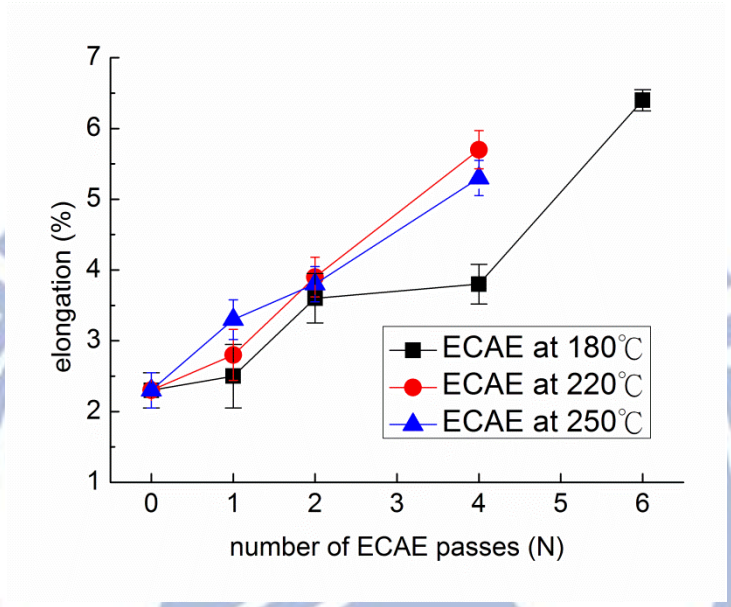

Figure 3.10 (c)

Figure 3.11 Tensile properties at room temperature: (a) UTS, (b) YS, and (c) elongation.

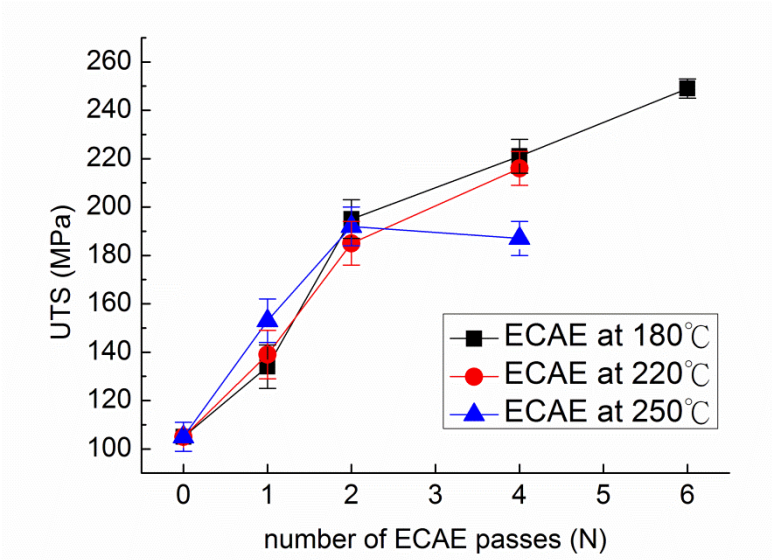

Figure 3.12 (a)

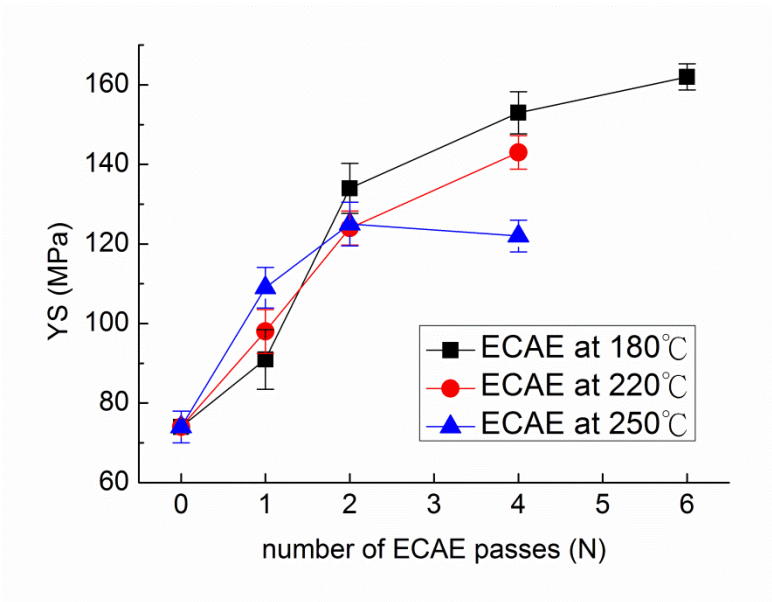

Figure 3.12 (b)

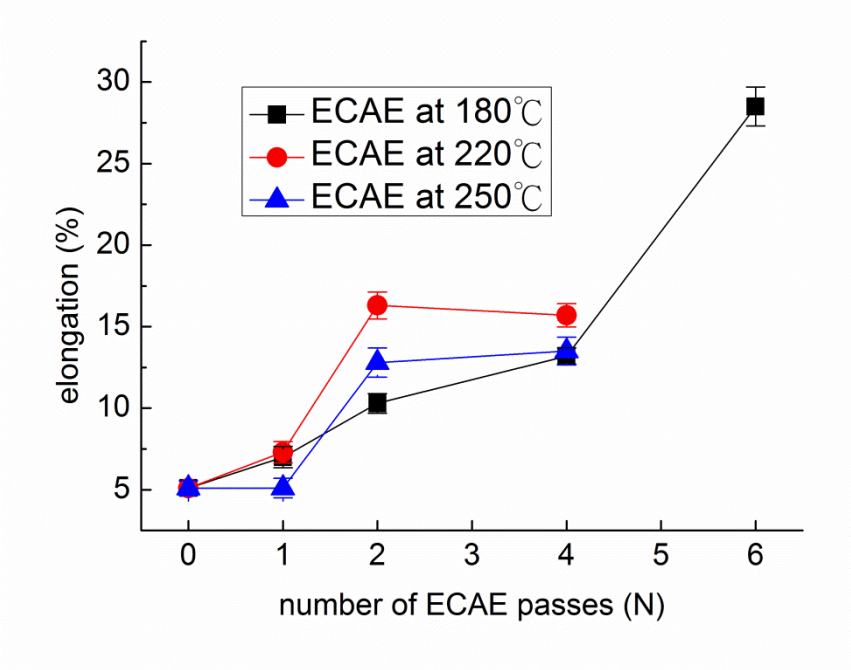

Figure 3.12 (c)

Figure 3.12 Tensile properties at 200 ℃: (a) UTS, (b) YS, and (c) elongation.

Table 3.1 Chemical composition of the ZA85 alloy

Element	Zn	Al	Mg
wt.%	8.34	4.74	Bal.

Table 3.2 Composition of matrix and second phase in the ZA85 alloy

Phase	Mg (wt.%)	Zn (wt.%)	Al (wt.%)
Matrix	96.67	--	3.33
Second phase	37.27	48.18	14.55

Table 3.3 Room temperature tensile properties of the ZA85 alloy

Alloy	Condition	UTS (MPa)
AZ91	die–cast, N=8	375 [18]
AZ31	as–extruded, N=8	310 [32]
AZ31	SC[b], N=4	210 [29]
AZ31	HR[c], N=4	350 [33]
ZA85[a]	as–cast, N=6	402

a: this work; b: squeeze casting; c: hot rolling

Table 3.4 High–temperature tensile properties of the ZA85 alloy [33]

Alloy	Temp. (^{o}C)	UTS (MPa)
AE42	177	135
AX53	175	196
AJ52X	175	148
AXJ	175	196
ZA85[a]	200	249

a: this work

Chapter 4 Effects of Equal–Channel Angular Extrusion on the Microstructure and Tensile Properties of the Solution–Heat–Treated ZA85 Magnesium Alloy

4.1 Introduction

In recent years, magnesium alloys have been widely used in the transportation, aerospace, and mobile electronics industries because of their advantages, which include low density, high specific strength, good damping capacity, high thermal conductivity, and good electromagnetic shielding characteristics [1–4]. Among various magnesium alloys, Mg–Al based alloys are widely used because of their desirable mechanical properties, corrosion resistance, and casting performance. However, the service temperature of Mg–Al based alloys is limited at temperatures above 120 ℃ because of the presence of $Mg_{17}Al_{12}$ (β–phase), which precipitates primarily along grain boundaries and exhibits a low decomposition temperature [5,6]. Therefore, numerous studies have been conducted to develop heat–resistant magnesium alloys. Magnesium alloys containing rare–earth (RE) elements heve been reported to be interesting light structureal materials with high strength at both room and elevated temperatures [7–9]. However, the application of Mg–RE alloys is limited because of their poor ductility and high cost of RE elements. At a Zn:Al composition of approximately 2:1, the ZA alloys with the $Mg_{32}(Al,Zn)_{49}$ (τ–phase) as the dominant intermetallic phase have been reported to completely suppress the formation of the β–phase. The τ–phase has a higher melting point and decomposition temperature than the β–phase. Consequently, ZA alloys exhibit strong potential for the development of heat–resistant magnesium alloys [10–12].

Conventional static aging is an effective way to improve the mechanical

properties of materials. Artifitial aging after a solution heat treatment (SHT) is a matter of temporal discretion in the nucleation and growth of precipitates. Dynamic precipitation (or dynamic aging) is a process that combines thermo–mechanical processing (TMP) and an aging treatment. After the SHT process, the precipitation reaction occurs simultaneously during TMP. Cai et al. have reported that, compared with a static aging process, both the 6061 and 6069 aluminum alloys experienced dynamic precipitaion and that the peak values of the hardness were achieved within a shorter time after the SHT + TMP process [13]. Moreover, the peak values of hardness, ultimate tensile strength (UTS), and yield strength (YS) of the dynamically aged alloys are also greater than those of the statically aged alloys. Equal–channel angular extrusion (ECAE) is an efficient TMP method. A great advantage of ECAE over other TMP methods is the possibility of accumulating a large amount of strain by repeating the process over several cycles because the channel cross–sections are identical. In addition, ECAE is a promising process for obtaining ultrafine–grained materials with increased strength and ductility through severe plastic deformation [2,6,12,14–19]. An ECAE die consists of two channels with identical cross–sections that intersect at an angle. A billet of the experimental material is placed into one of the channels and is pressed through the second channel. The material experiences severe deformation via pure shear as it crosses the intersection channel.

In the present study, the effects of ECAE on ZA85 alloy subjected to SHT were investigated. The ZA85 alloy was chosen as the experimental alloy because we found that both the strength and ductility of the ZA85 alloy are greatly increased by the ECAE process [2,12]. The strength at room temperature (RT) and at 200 ℃ are both superior to those of many other commercial magnesium alloys. Dynamic precipitation occurred during the ECAE process for the solution–heat–treated ZA85 alloy, leading to the formation of fine and well–distributed τ–phase particles in the α–Mg matrix.

Therefore, to further improve the tensile properties of the experimental material, the SHT process was conducted prior to the ECAE process in this study.

4.2 Experimental Procedures

An alloy with a composition of Mg–8 wt.% Zn–5 wt.% Al (ZA85) was prepared from commercially pure Mg, Al, and Zn (> 99.9%). A steel crucible and electronic resistance furnace were used for melting and alloying at 750 ℃ with SF_6 as the protective atmosphere. Steel molds with cavity dimensions of 300 mm × 70 mm × 60 mm were used for casting the alloy. The as–cast alloy in the molten state was air cooled. The chemical composition of the as–cast alloy, as determined by energy dispersive spectroscopy, was 8.34 wt.% Zn and 4.74 wt.% Al with the balance Mg. For the SHT process, specimens with dimensions of 17 mm × 17 mm × 60 mm were cut from the as–cast ingot. The SHT process was conducted at 335 ℃ for 48 h using a tube furnace. After the SHT process, the treated specimens were subjected to a two–step ECAE process. The first ECAE pass was conducted at a higher temperature of 250 ℃ to prevent cracking of the specimen during the ECAE process. The subsequent passes were conducted at 200 ℃. An ECAE die with a 120° angle was used, and boron nitride was used as the lubricant during the ECAE process. The ECAE die was preheated to the selected temperature and maintained at that temperature for 15 min before a lubricated ECAE specimen was inserted into the entrance channel. The specimen was held inside the ECAE die for 5 min before being pressed. The ECAE process was conducted via Route B_C, in which the specimen was rotated through 90° in the same direction after each pass with a pressing speed of 1 mm/min [20]. X-ray diffraction (XRD) studies were conducted to identify the phases present in the experimental alloy. Microstructures of the as–cast and ECAP materials were examined using standard metallographic procedures. The polished surfaces were

etched with 3 mL acetic acid solution, 5 mL deionized water, 35 mL ethanol, and 1 g picric acid. The microstructures were observed by optical microscopy and scanning electron microscopy (SEM). The average grain size was determined using Image Pro software package (IpWin32). A Rockwell indenter with a load of 100 kgf was used for Rockwell hardness B (HRB) tests at RT. The HRB values were averaged over 10 tests under each set of conditions. The tensile specimens with a gauge section of 6 mm × 3 mm × 2 mm were longitudinally cut from the ECAE specimens. Tensile tests were conducted at RT and 200 ℃ with an initial strain rate of $1 \times 10^{-3}\,s^{-1}$ using an Instron 8501 universal testing machine. A furnace mounted on the machine was used for high-temperature tensile tests. The specimens were heated to the selected temperature and then maintained at that temperature for 10 min prior to the tensile tests. The UTS, YS, and elongation were averaged over three to five tests under each set of conditions.

4.3 Results and Discussion

Fig. 4.1 presents the optical micrograph of the as–cast ZA85 alloy. The initial grain size of ~150 μm was obtained with an equiaxed grain structure. The coarse non–continuous second phase was distributed along the grain boundaries. Moreover, casting defects such as blow holes and shrinkage voids were clearly observed in the as–cast alloy. Fig. 4.2 shows the XRD pattern of the as–cast ZA85 alloy. The pattern confirms that the alloy consisted of the α–Mg matrix and the τ–phase, consistent with the results of previous reports [21–23]. Fig. 4.3 shows the SEM micrograph of the solution–heat–treated ZA85 alloy. The average grain size slightly increased to ~170 μm because of the high–temperature effect. A large amount of the τ–phase was dissolved into the α–Mg matrix, with only a small amount left along the grain boundaries. The resultant microstructure is very similar to that reported by Balasubramani et al. [24]. The XRD patterns do not show peaks that correspond to the

τ–phase in the solution–heat–treated specimens, as shown in Fig. 4.4, which is consistent with the microstructure of the solution–heat–treated ZA85 alloy.

A two–step ECAE process was used in this study. The first pass was conducted at higher temperature of 250 ℃ in to prevent cracking of the specimen. The following passes were then conducted at a lower temperature of 200 ℃ to reduce the grain growth effect. Lin et al. [12] reported that the average grain size of the ZA85 alloy would obviously increase at an ECAE temperature greater than 220 ℃. Fig. 4.5 shows the microstructure of the solution–heat–treated ZA85 alloy after the ECAE process. After fewer than four ECAE passes, all microstructures became inhomogeneous with fine dynamic–recrystallized grains along the grain boundaries and a number of large distorted grains. This resultant microstructure, termed as "bimodal," was also observed by Chang et al. [25]. Because of the dynamic recrystallization, the average grain size was greatly reduced as the number of ECAE passes increased [12,26,27], as shown in Fig. 4.6. Dynamic recrystallization led to the production of equiaxed grains with a high fraction of high–angle grain boundaries. After six ECAE passes, the microstructure became visibly uniform, and the average grain size was substantially reduced to approximately 4 μm, as shown in Fig. 4.5(d). In addition, casting defects such as blow holes and shrinkage voids were eliminated by the ECAE process.

In the present study, the τ–phase is divided into two categories: a non–dissolved τ–phase after the SHT process (denoted as τ_1) and the one formed by dynamic precipitation during the ECAE process (denoted as τ_2). The τ_1–phase would be shattered by shear stress during the ECAE process. Fig. 4.7(a) shows the SEM micrograph of the initial grain boundaries of the solution–heat–treated alloy after four ECAE passes. The shattered τ_1–phase particles with the average size of ~1 μm are distributed on the grain boundaries of the dynamic recrystallized grains. Close

inspection of the shape and surface of τ_1–phase particles reveals an irregular shape and rough surface, which is evidence that the τ_1–phase particles were shattered by shear stress during the ECAE process. These fine and well distributed τ_1–phase particles can effectively inhibit grain–boundary migration to improve the strength of the experimental alloy [12]. Fig. 4.7(b) shows the SEM micrograph of the α–Mg matrix of the solution–heat–treated alloy after four ECAE passes. The τ_2–phase particles with sizes of ~100 nm are well distributed in the α–Mg matrix. The round shape and smooth surface of these τ_2–phase particles are evidence that they form by dynamic precipitation during the ECAE process. However, after six ECAE passes, some τ_2–phase particles grew to ~300 nm and some precipitation–free zones (PFZs) were clearly observed, as shown in Fig. 4.7(c). The coarsening phenomenon is due to the longer time at high temperature in the case of samples subjected to six ECAE passes compared with those subjected to four passes. These coarsened τ_2–phase particles and PFZs are evidence of overaging, which would be unfavorable to the mechanical properties of the experimental alloy. Furthermore, XRD analysis showed that the τ–phase was present in the SHT + ECAE samples, as shown in Fig. 4.8. This result also implies that the τ_2–phase was formed by dynamic precipitation during the ECAE process.

Fig. 4.9 shows the results of a hardness test on the ZA85 alloy at RT. The HRB values were averaged over 10 tests under each set of conditions. The hardness of the as–cast alloy was HRB 19 and increased to HRB 24 after the SHT process, which is attributed to solid–solution hardening. The results in Fig. 4.9 also suggest that the hardness increased with increasing number of ECAE passes, with the exception of the one fabricated using six ECAE passes. The maximum hardness of HRB 46 occurred in the specimen fabricated using four ECAE passes. In general, smaller grains resulted in greater strength, as shown in Figs. 4.6 and 4.9. After six ECAE passes, the hardness

decreased to HRB 44 even though the average grain size for six ECAE passes was smaller than that for four ECAE passes. This result is attributed to overaging of the experimental alloy. The coarsened τ_2–phase particles and PFZs would adversely affect the strength of the materials. Balasubramani et al. [24] proposed that for solution–heat–treated ZA84 alloy, the optimum conditions for static aging are 180 ℃ and 16 h. In this study, the maximum hardness was observed in the sample fabricated using four ECAE passes. The time required for one single ECAE pass was approximately 1 h, which means that attaining the maximum hardness of the experimental alloy requires only 4 h. This phenomenon is due to two factors: the ECAE temperature is higher than 180 ℃, and aging occurs during the ECAE process. Both the higher temperature and external force would decrease the energy barriers required for precipitation and growth, thereby leading to a shorter time required to reach the peak hardness value. Cai et al. [13] proposed that, compared with 6061 and 6069 aluminum alloys aged by a static aging process, the same alloys underwent dynamic precipitaion, and the peak values of the hardness were achieved within a shorter time after being subjected to the SHT + ECAE process. The aging responses in some Al–Mg–Si alloys have also been reported to be accelerated by the ECAE process [28]. In the present study, the great improvement in the hardness of the experimental alloy is attributed to the grain refinement and presence of fine and well–distributed τ_1– and τ_2–phase particles. The τ_1–phase particles can inhibit grain–boundary migration, and the τ_2–phase particles can effectively obstruct the dislocation motion; thus, improve the properties of the experimental alloy.

Figs. 4.10 and 4.11 show the results of the tensile tests conducted on the ZA85 alloy at RT and 200 ℃, respectively. Notably, the data for the as–cast + ECAE condition are referenced from our previous study [12]. Also, the values for N = 0 in these figures represent results for the solution–heat–treated alloy in this study and for

the as–cast alloy in our previous study, respectively. The trend of the tensile properties determined in this study is similar to the trend of the hardness properties, i.e., the tensile strength reached its maximum value after four ECAE passes but decreased after six ECAE passes. The maximum UTS/YS of 415 MPa/284 MPa and 261 MPa/173 MPa were obtained at RT and 200 ℃, respectively. These figures also clearly imply that, after the same number of ECAE passes, both the UTS and YS of the samples fabricated using the SHT + ECAE process are greater than those of the samples fabricated using only the ECAE process, with the exception of the sample subjected to six ECAE passes. According to our previous study [12], the strengthening factors for the ECAE alloy are the grain refinement and well–distributed τ_1–phase particles. However, in this study, the strengthening factors for the SHT + ECAE alloy are the grain refinement, precipitation hardening, and presence of fine and well–distributed τ_1 and τ_2–phase particles. Refined grains less than 5 μm in size would hinder dislocation and improve mechanical properties. After SHT, the solute atoms act as a barrier to obstruct the dislocation movement and increase the strength of the materials. Moreover, the fine and well–distributed τ_1 and τ_2–phase particles are also important in improving the mechanical properties. The τ_1–phase particles uniformly distributed at dynamic recrystallized grain boundaries hinder grain– boundary migration. The τ_2–phase particles uniformly distributed in the α–Mg matrix impede dislocation movement. Therefore, the application of the SHT process prior to the ECAE process can obviously improve the tensile properties of the present alloy at RT as well as at 200 ℃. Notably, the tensile properties at RT and 200 ℃ of the SHT + ECAE ZA85 alloy in the present study are superior to those of many other ZA series Mg alloys, as shown in Tables 4.1 and 4.2, respectively [12,29–32]. Fig. 4.12 shows that the elongation of the present alloy was improved by the ECAE process. Notably, N = 0 represents the solution–heat–treated sample. At RT, the elongation of the alloy

improved from 4.2% to approximately 9% after six ECAE passes. At 200 ℃, the elongation of the alloy increased from 7.4% to approximately 60% after six ECAE passes. This increase in elongation after the ECAE process is attributed to three factors: (I) the elimination of casting defects such as blow holes and shrinkage voids, as shown in Fig. 1; (II) the improvements of not only the strength but also the ductility of the materials via grain refinement; (III) the homogeneity of the microstructure.

Fig. 4.13 shows the tensile fracture surface for the experimental alloy. In general, the failure of Mg alloys is brittle through cleavages at RT because of their HCP structure. Fig. 4.13(a) shows that the fracture surface for the solution–heat–treated sample tested at RT was mainly cleavages. Fig 4.13(b) shows that the fracture surface tested at RT consisted of some minor dimples and cleavages for the solution–heat–treated sample fabricated using six ECAE passes. This result means that the ductility of the materials was improved by the ECAE process, which is consistent with the elongation values shown in Fig. 4.12. Fig. 4.13(c) shows that the fracture surface for the solution–heat–treated sample tested at 200 ℃ was cleavages. Fig 4.13(d) shows that the fracture surface tested at 200 ℃ was mainly large dimples for the solution–heat–treated sample fabricated using six ECAE passes. The size of dimples is related to the ability to impede crack propagation in that a good ability to impede crack propagation would lead to large dimples. Therefore, the results in Fig. 4.12 suggest that both the number of ECAE passes and testing temperature affect the fracture surface of the investigated alloy. At the same testing temperature, additional ECAE passes corresponds to a finer grain size, which, in turn, results in improved ability to impede crack propagation and leads to a larger dimple size and better ductility. In addition, at six ECAE passes, a higher temperature leads to a larger dimple size and to better ductility through thermal activation. The resultant fracture

surface matches the value of the elongation in the experimental alloy shown in Fig. 4.12 with the value of the elongation that increases with increasing fraction of dimples.

4.4 Summary and Conclusions

The effects of ECAE on the microstructure and tensile properties of the solution–heat–treated ZA85 magnesium alloy were examined, and some interesting findings were obtained:

1. The initial grain size of ~150 μm of the as–cast sample slightly increased to ~170 μm after the sample was subjected to the SHT process. The grain size subsequently decreased as the number of ECAE passes increased. After six ECAE passes, the grain size decreased to ~4 μm.
2. After the SHT process, a large amount of τ–phase was dissolved into the α–Mg matrix, and XRD analysis did not indicate the presence of the τ–phase in the solution–heat–treated specimens.
3. In this study, τ–phase is divided into two categories: the τ_1–phase represents the non–dissolved τ–phase after the SHT process, whereas the τ_2–phase is formed by dynamic precipitation during the ECAE process. After the ECAE process, the τ_1–phase would be shattered to an average size of ~1 μm and would be distributed on the grain boundaries of the dynamic recrystallized grains; the τ_2–phase particles with sizes of ~100 nm are well distributed in the α–Mg matrix. However, after six ECAE passes, some τ_2–phase particles grow to ~300 nm and PFZs are clearly observed, which indicate overaging.
4. The best mechanical properties were found in the specimen fabricated by SHT + four ECAE passes. At RT, the maximum hardness, UTS, and YS values of HRB 46, 415 MPa, and 284 MPa, respectively, were obtained. At 200 ℃, the maximum

UTS and YS of 261 MPa and 173 MPa, respectively, were reached. The strengthening factors for the SHT + ECAE alloy are the grain refinement, precipitation hardening, and presence of fine and well–distributed τ_1 and τ_2–phase particles. The mechanical properties of the present alloy at RT and at 200 ℃ are both superior to those of numerous other ZA–series Mg alloys. After six ECAE passes, the strength of the experimental alloy slightly decreased due to overaging.

5. The elongation of the present alloy increased with increasing number of ECAE passes is ascribed to three factors: (I) the elimination of casting defects; (II) grain refinement; (III) a homogeneous microstructure. After six ECAE passes, the maximum elongations of 9% and 60% were attained at RT and 200 ℃, respectively.

References

[1] D. Eliezer, E. Aghion, F.H. Froes, Advanced Performance Materials 5 (1998) 201.

[2] C.Y. Lin, H.Y. Bor, C.G. Chao, T.F. Liu, Journal of Alloys and Compounds 556 (2013) 26.

[3] J. Wang, S. Gao, P. Song, X. Huang, Z. Shi, F. Pan, Journal of Alloys and Compounds 509 (2011) 8567.

[4] X.F. Huang, W.Z. Zhang, J.F. Wang, W.W. Wei, Journal of Alloys and Compounds 516 (2012) 186.

[5] A. Srinivasan, U.T.S. Pillai, B.C. Pai, Metallurgical and Materials Transactions A 36 (2005) 2235.

[6] J.Jiang, Y. Wang, Z. Du, J. Qu, Y. Sun, S. Luo, Journal of Materials Processing Technology 210 (2010) 751.

[7] D.K. Xu, W.N. Tang, L. Liu, Y.B. Xu, E.H. Han, Journal of Alloys and Compounds 432 (2007) 129.

[8] J.F. Nie, K. Oh–ishi, X. Gao, K. Hono, Acta Materialia 56 (2008) 6061.

[9] J. Luo, K. Qiu, W. Jie, X. Dong, F. Li, Journal of Rare Earths 30 (2012) 486.

[10] M. Vogel, O. Kraft, E. Arzt, Scripta Materialia 48 (2003) 985.

[11] J. Zhang, Z.X. Guo, F. Pan, Z. Li, X. Luo, Materials Science and Engineering A 456 (2007) 43.

[12] C.Y. Lin, H.J. Tsai, C.G. Chao, T.F. Liu, Journal of Alloys and Compounds 530 (2012) 48.

[13] M. Cai, D.P. Field, G.W. Lorimer, Materials Science and Engineering A 373 (2004) 65.

[14] V.M. Segal, Mater. Sci. Eng. A 197 (1995) 157-164.

[15] K. Yan, Y.S. Sun, J. Bai, F. Xue, Materials Science and Engineering A 528 (2011) 1149.

[16] R.B. Figueiredo, T.G. Langdon, Scripta Materialia 61 (2009) 84.

[17] K.Matsubara, Y. Miyahara, Z. Horita, T.G. Langdon, Acta Materialia 51 (2003) 3073.

[18] V.N. Chuvil'deev, T.G. Nieh, M.Yu. Gryaznov, A.N. Sysoev, V.I. Kopylov, Scripta Materialia 50 (2004) 861.

[19] X. Liu, R. Wu, Z. Niu, J. Zhang, M. Zhang, Journal of Alloys and Compounds 541 (2012) 372.

[20] Y. Iwahashi, Z. Horita, M. Nemoto, T.G. Langdon, Acta Materialia 46 (1998) 3317.

[21] Z. Zhang, A. Couture, A. Luo, Scripta Materialia 39 (1998) 45.

[22] J. Zhang, Z.X. Guo, F. Pan, Z. Li, X. Luo, Materials Science and Engineering A 456 (2007) 43.

[23] N. Balasubramani, A. Srinivasan, U.T.S. Pillai, K. Raghukandan, B.C. Pai, Journal of Alloys and Compounds 455 (2008) 168.

[24] N. Balasubramani, U.T.S. Pillai, B.C. Pai, Journal of Alloys and Compounds 457 (2008) 118.

[25] S.Y. Chang, S.W. Lee, K.M. Kang, S. Kamado, Y. Kojima, Mater. Trans. 45 (2004) 488-492.

[26] M. Janeček, M. Popov, M.G. Krieger, R.J. Hellmig, Y. Estrin, Materials Science and Engineering A 462 (2007) 116.

[27] C.W. Su, L. Lu, M.O. Lai, Materials Science and Engineering A 434 (2006) 227.

[28] K. Oh–ishi, Y. Hashi, A. Sadakata, K. Kaneko, Z. Horita, T.G. Langdon, Materials Science Forum 396–402 (2002) 333.

[29] S. Tardif, R. Tremblay, D. Dube, Materials Science and Engineering A 527 (2010) 7519.

[30] K. Yan, Y.S. Sun, J. Bai, F. Xue, Materials Science and Engineering A 528 (2011) 1149.

[31] J. Zhang, Y. Dou, B. Zhang, X. Luo, Materials Letters 65 (2011) 944.

[32] F. Pan, M. Yang, L. Cheng, Materials Science and Engineering A 527 (2010) 1074.

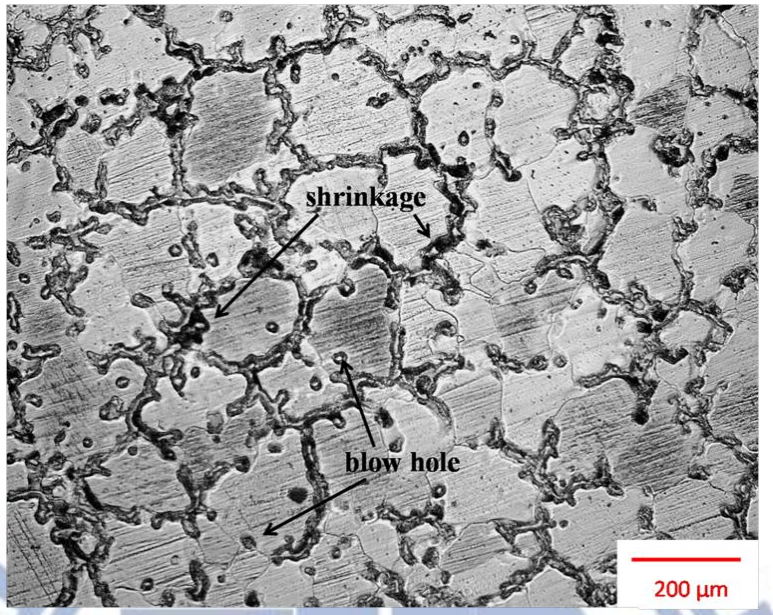

Figure 4.1. Optical micrograph of the as–cast ZA85 alloy.

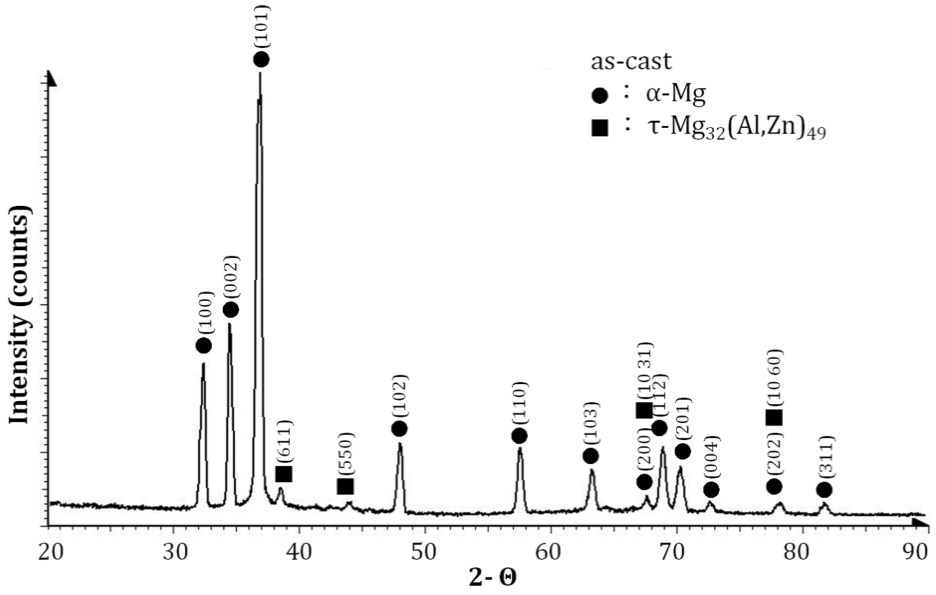

Figure 4.2. X–ray diffraction analysis of the as–cast ZA85 alloy.

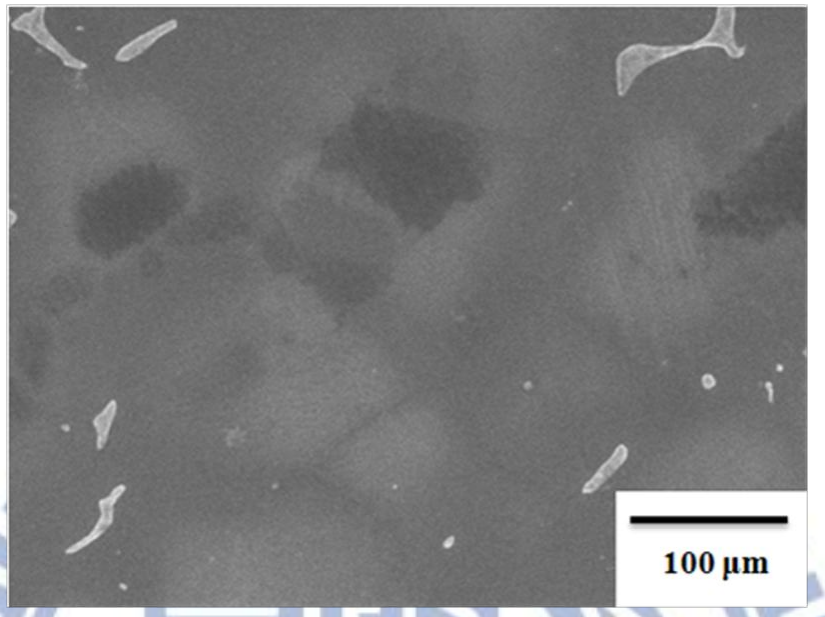

Figure 4.3. SEM micrograph of the solution–heat–treated ZA85 alloy.

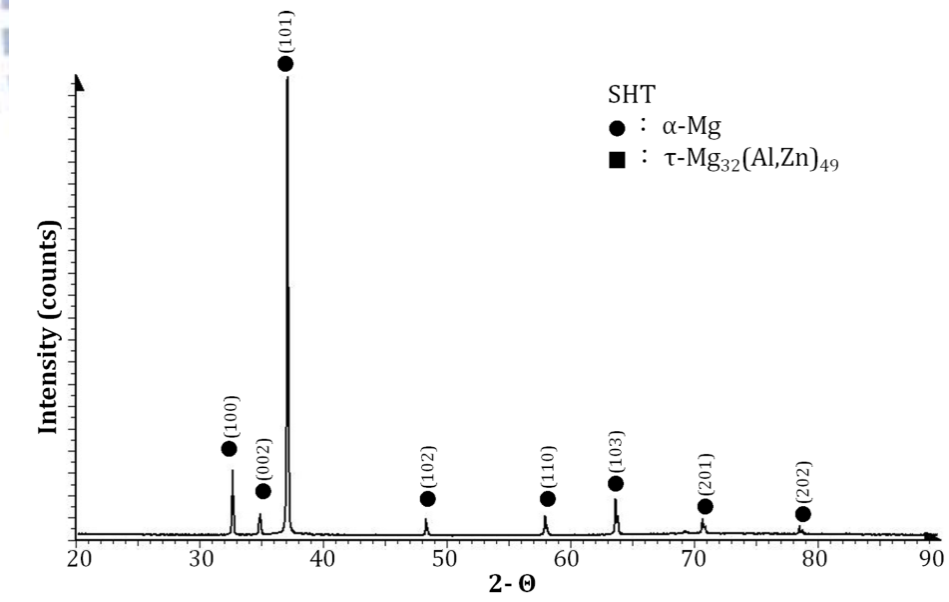

Figure 4.4. X–ray diffraction analysis of the solution–heat–treated ZA85 alloy.

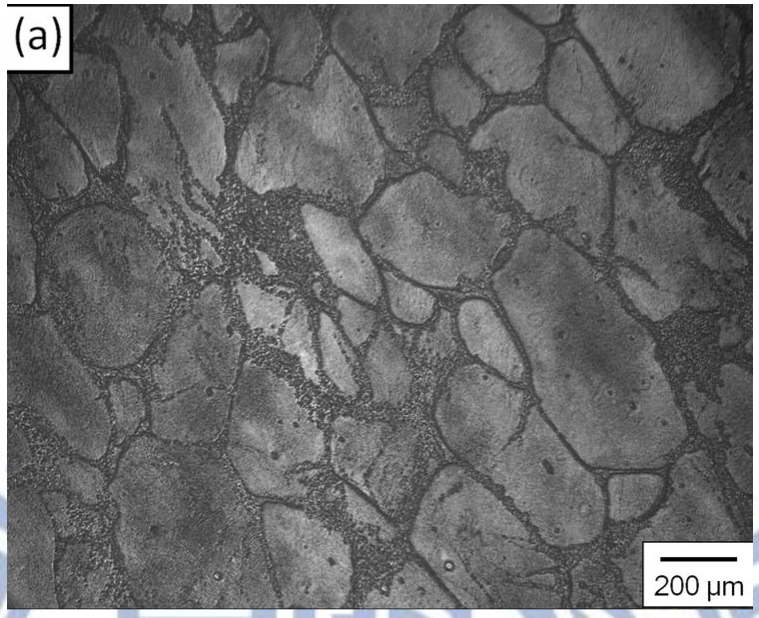

Figure 4.5 (a)

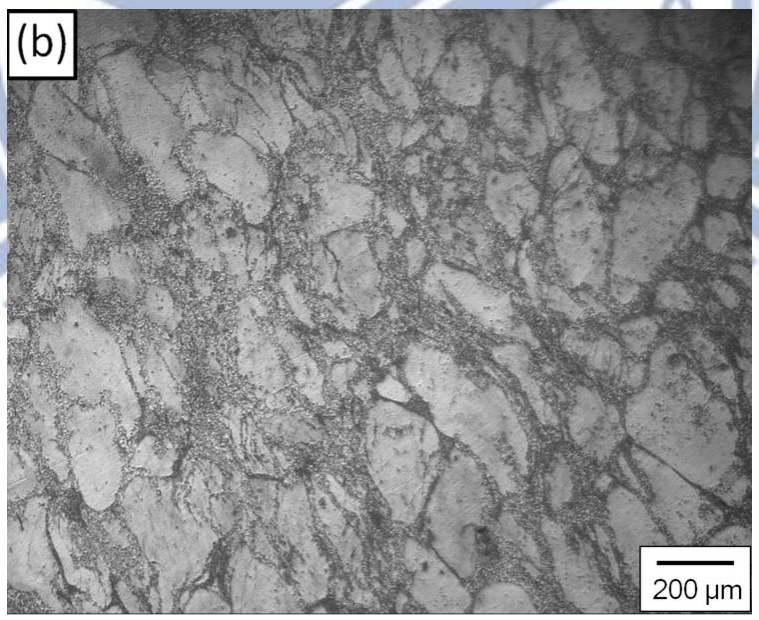

Figure 4.5 (b)

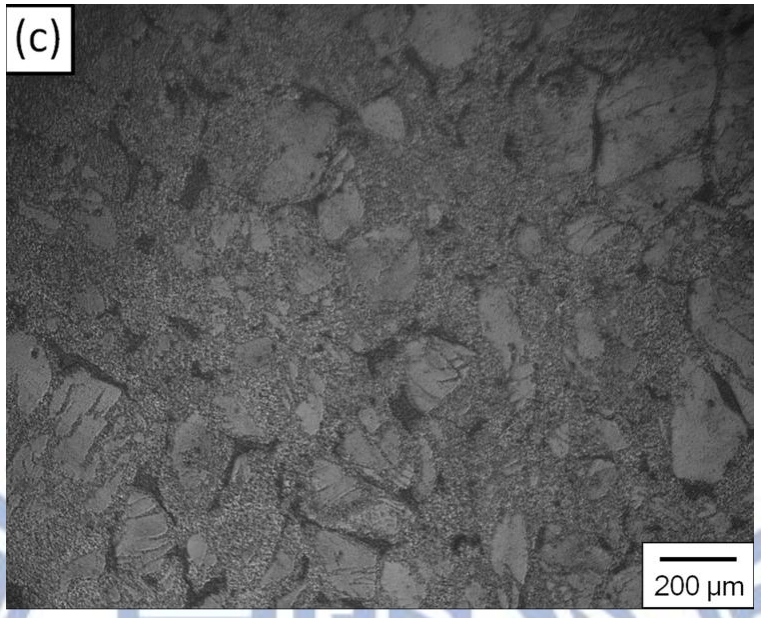

Figure 4.5 (c)

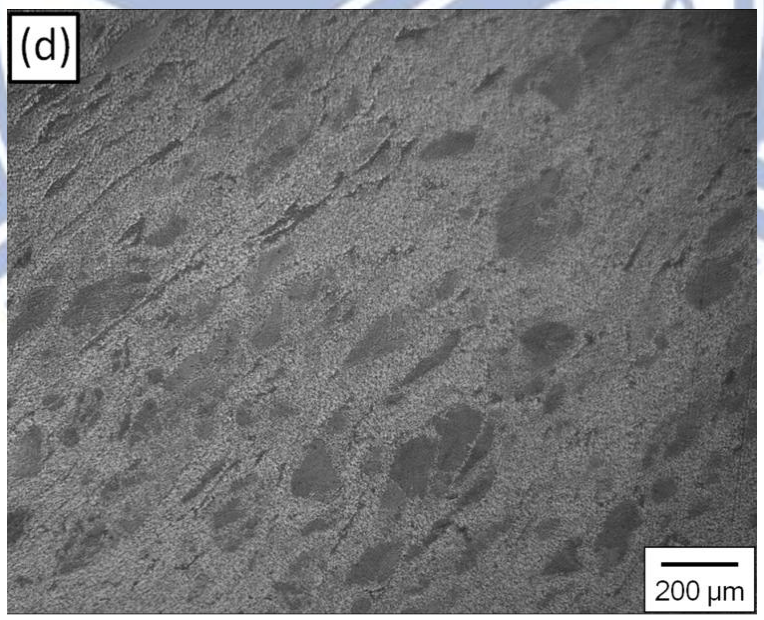

Figure 4.5 (d)

Figure 4.5. SEM micrographs of the solution–heat–treated ZA85 alloy after the ECAE process for (a) N = 1, (b) N = 2, (c) N = 4, and (d) N = 6.

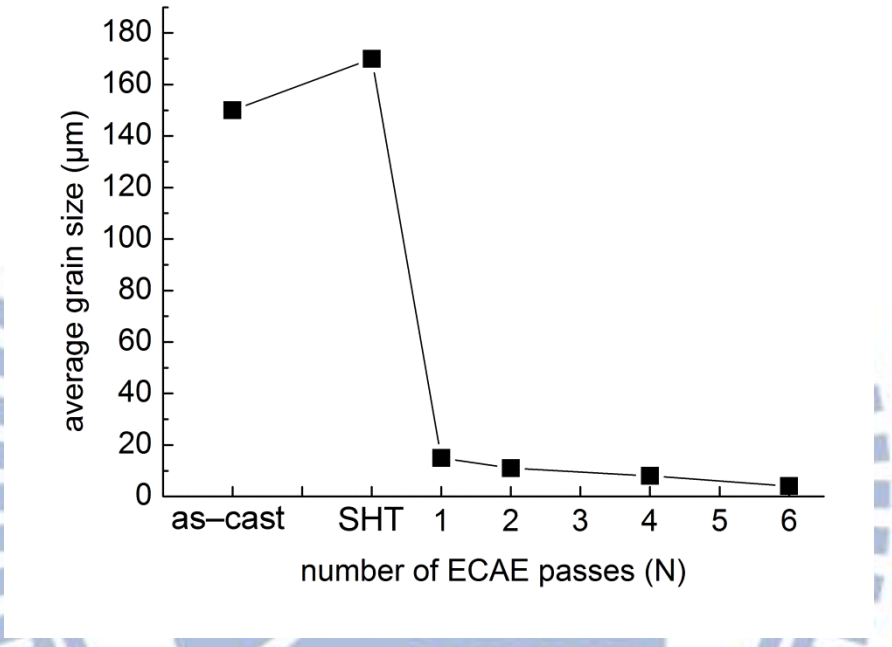

Figure 4.6 Average grain size versus different processing conditions of the ZA85 alloy.

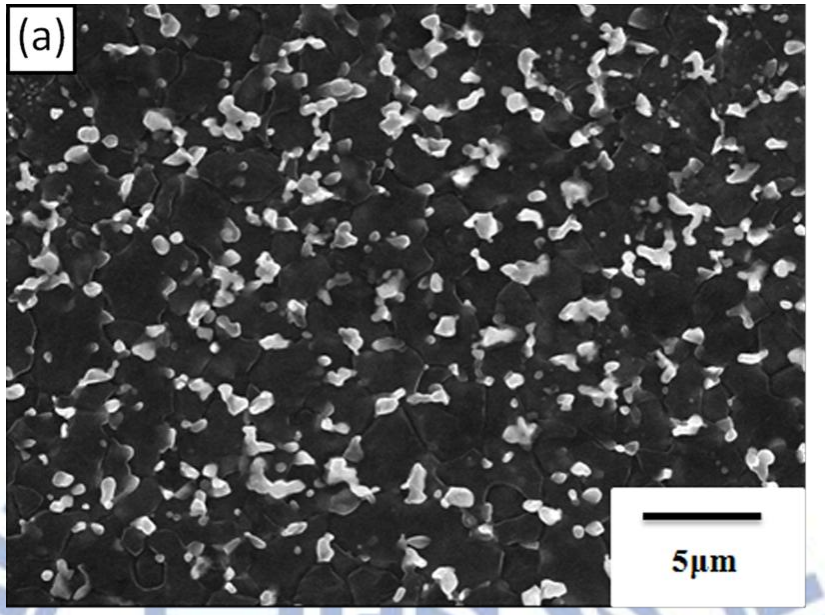

Figure 4.7 (a)

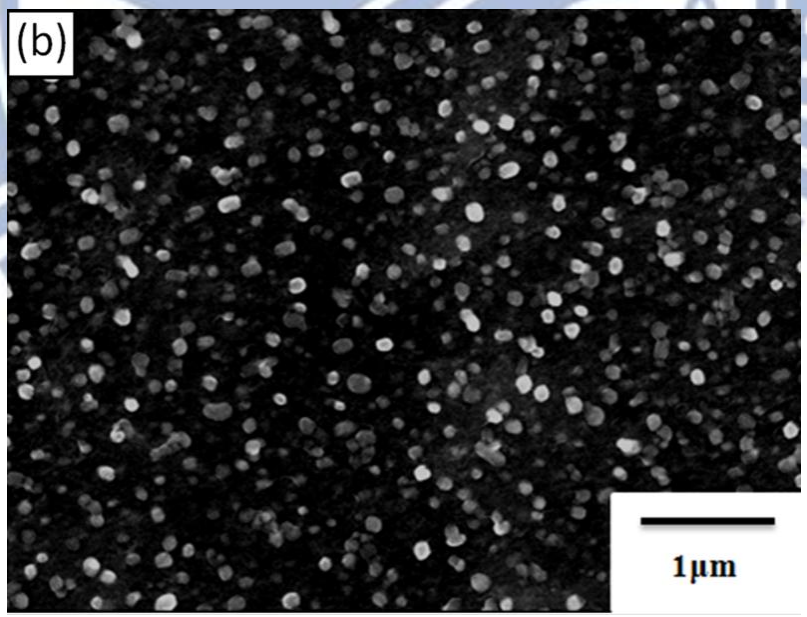

Figure 4.7 (b)

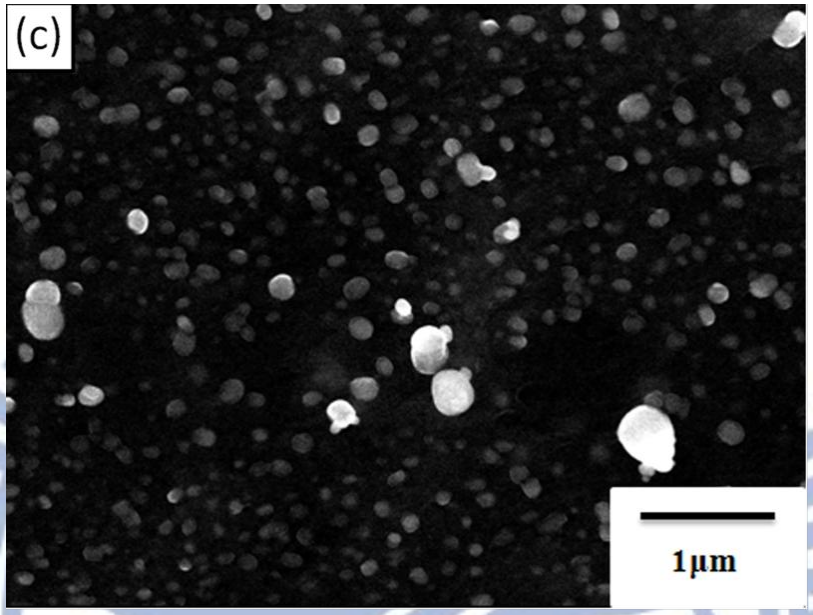

Figure 4.7 (c)

Figure 4.7. SEM micrographs of (a) the initial grain boundaries of the solution–heat–treated alloy after four ECAE passes, (b) the α–Mg matrix of the solution–heat–treated alloy after four ECAE passes, and (c) the α–Mg matrix of the solution–heat–treated alloy after six ECAE passes.

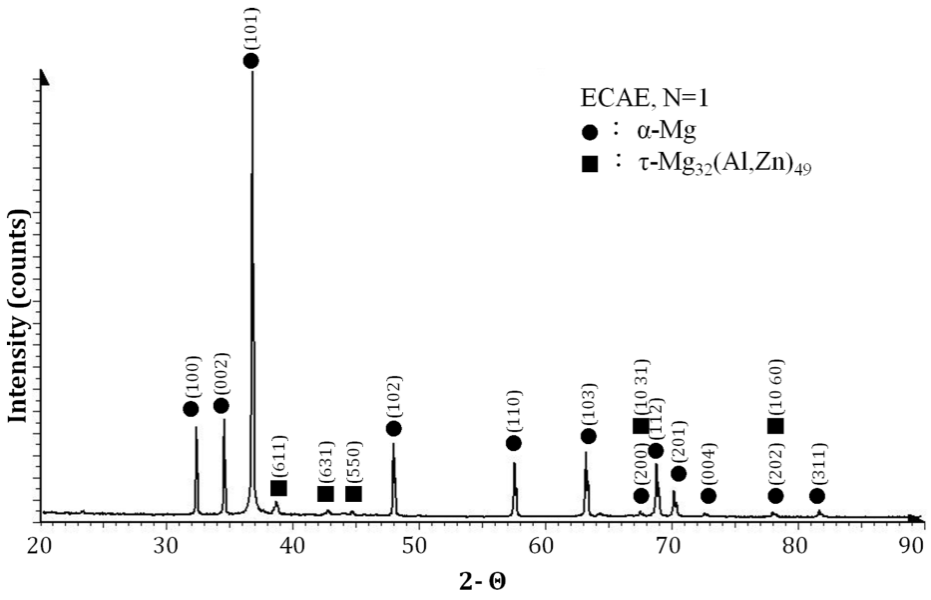

Figure 4.8. X–ray diffraction analysis of the SHT + ECAE ZA85 alloy.

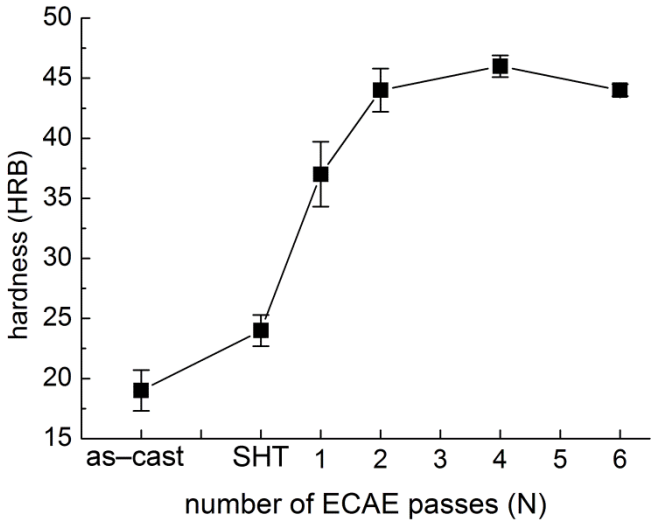

Figure 4.9. Hardness at room temperature under different processing conditions of the ZA85 alloy.

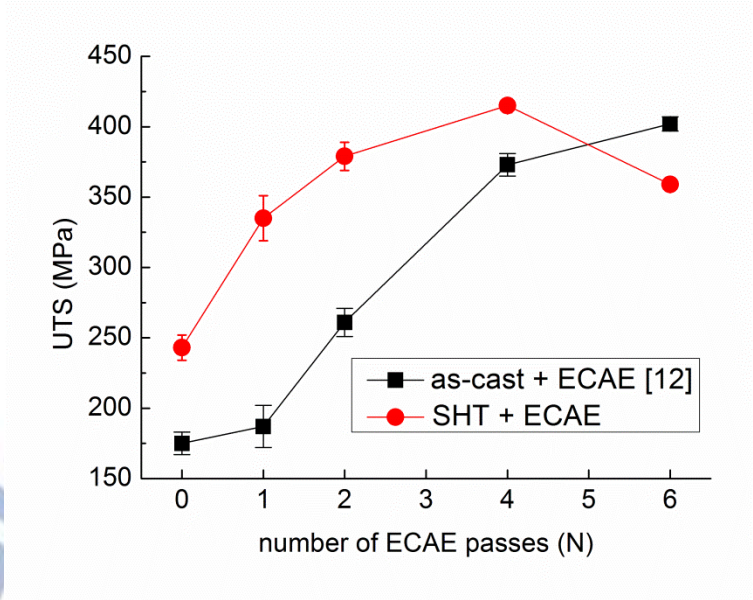

Figure 4.10 (a)

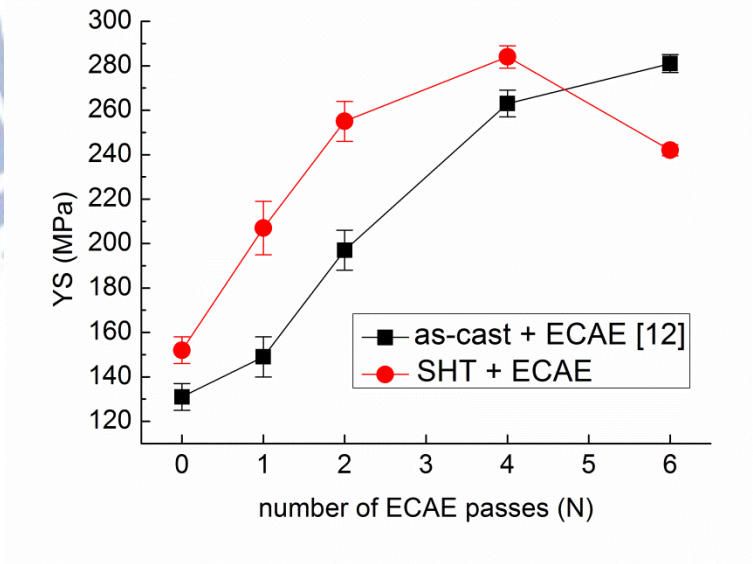

Figure 4.10 (b)

Figure 4.10. Tensile properties of the ZA85 alloy at RT: (a) UTS and (b) YS.

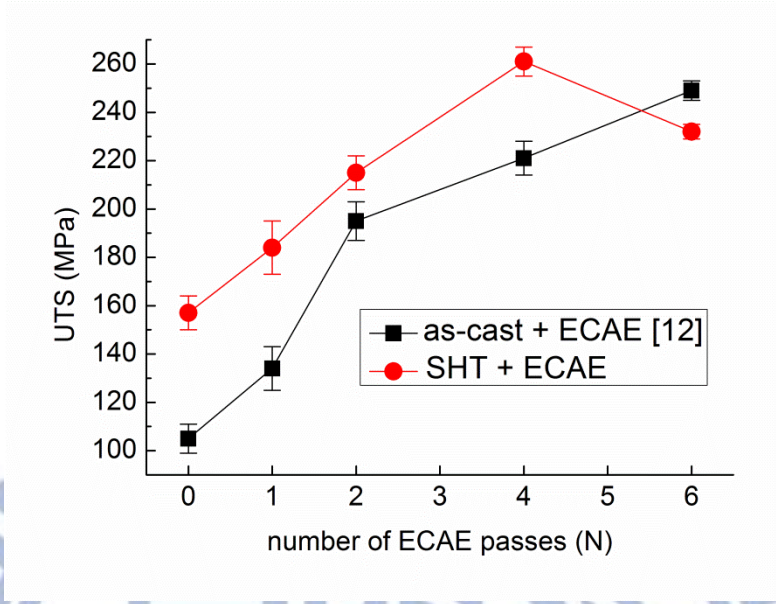

Figure 4.11 (a)

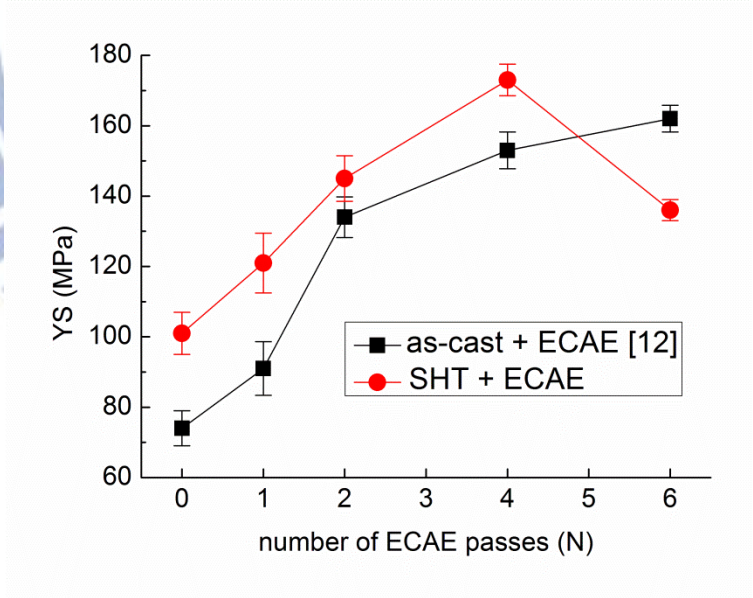

Figure 4.11 (b)

Figure 4.11. Tensile properties of the ZA85 alloy at 200 ℃: (a) UTS and (b) YS.

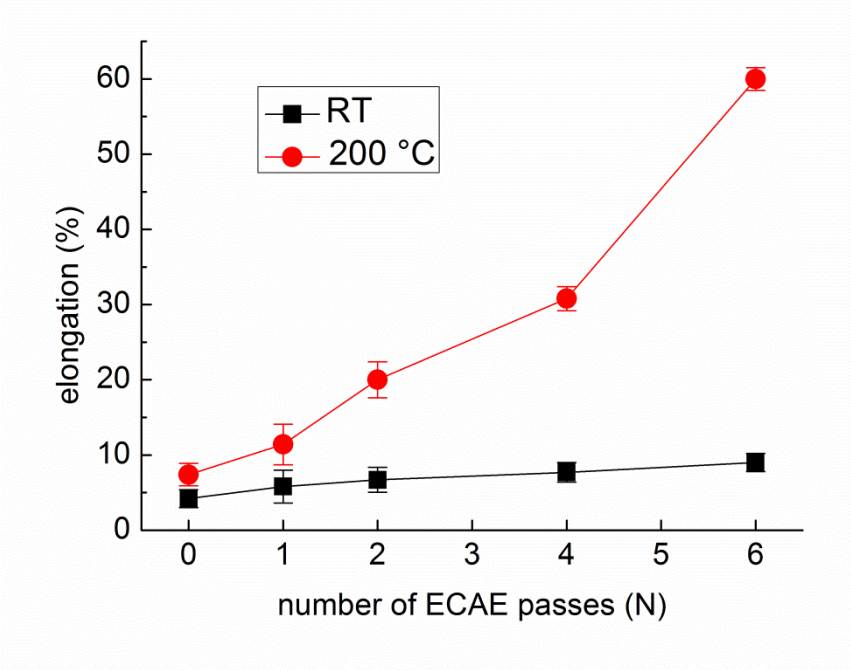

Figure 4.12. Elongation of the ZA85 alloy at RT and 200 ℃.

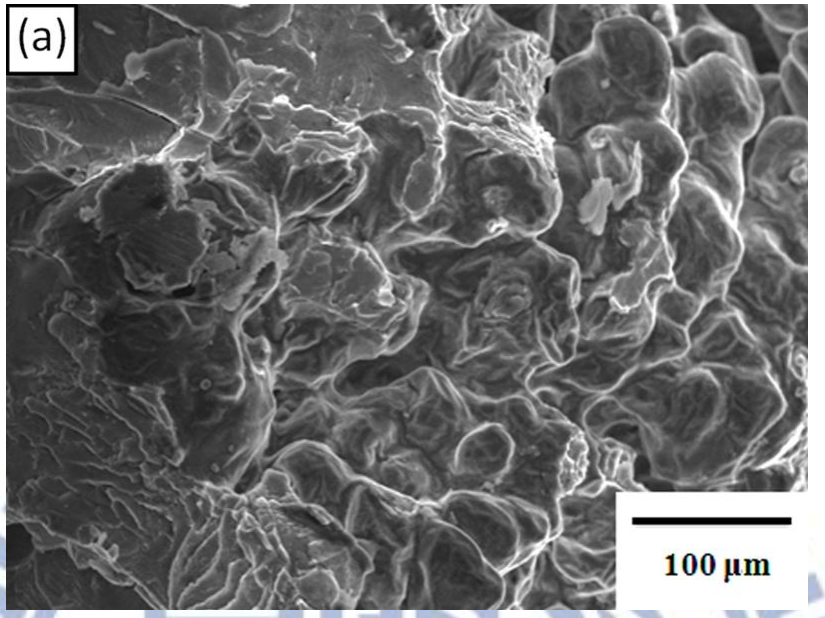

Figure 4.13 (a)

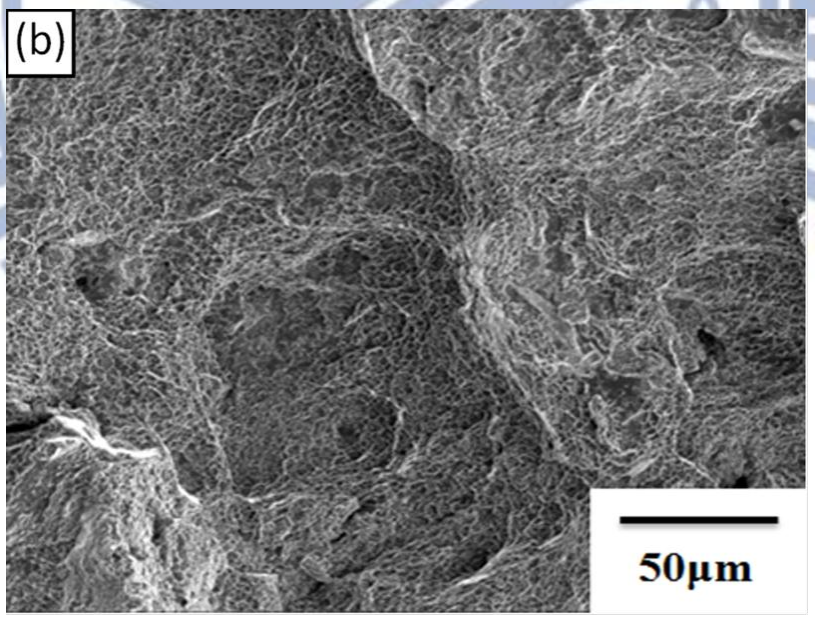

Figure 4.13 (b)

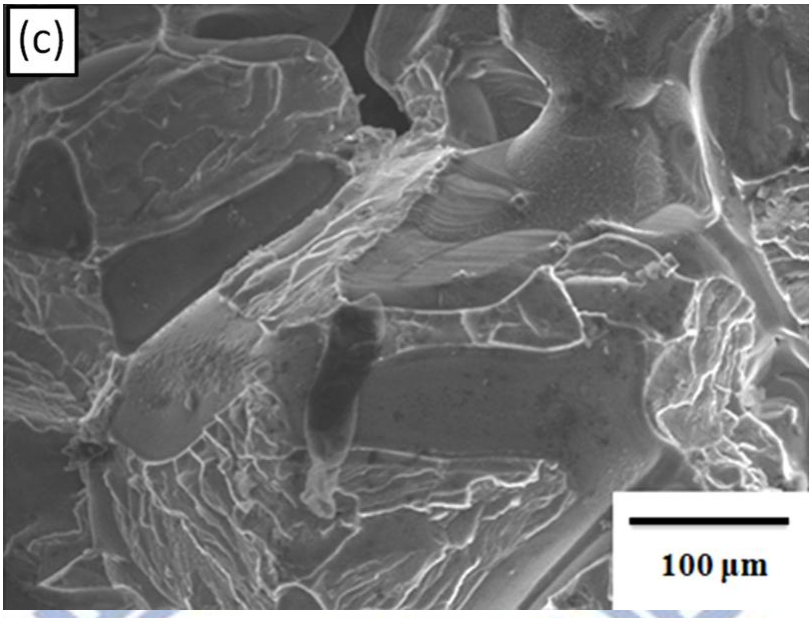

Figure 4.13 (c)

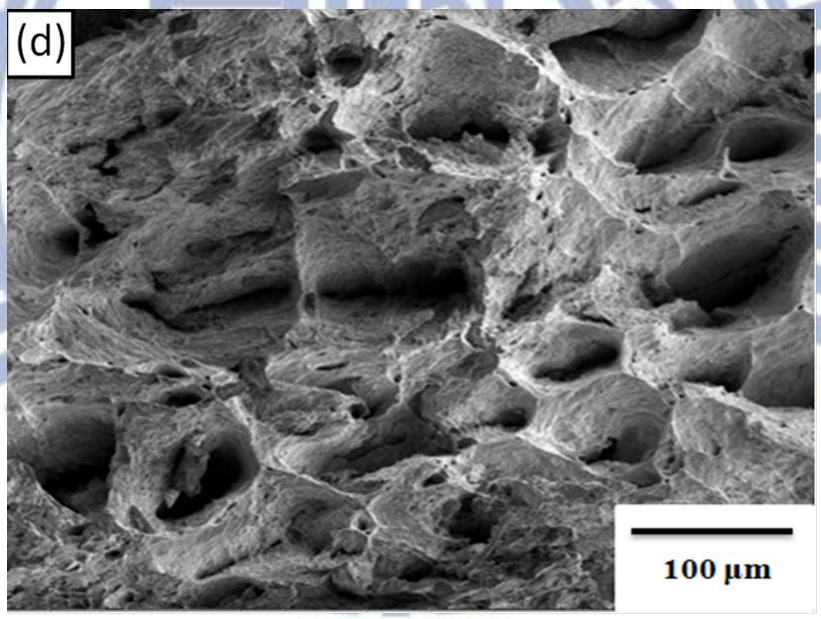

Figure 4.13 (d)

Figure 4.13. Tensile fracture surface for (a) the solution–heat–treated sample tested at RT, (b) the SHT + ECAE sample tested at RT, (c) the solution–heat–treated sample tested at 200 ℃, and (d) the SHT + ECAE sample tested at 200 ℃.

Table 4.1. Tensile properties of the ZA–series Mg alloy at room temperature [12,29–32]

Alloy	Condition	UTS (MPa)
ZA62	as–cast	190
ZA62	as–cast + ECAE (N = 8)	330
ZA73	as–cast	165
ZA73	as–cast + extrusion	360
ZA84	as–cast	174
ZA85	as–cast + ECAE (N = 6)	402
ZA85[a]	SHT + ECAE (N = 4)	415
ZA104	as–cast	188

a: this work

Table 4.2. Tensile properties of the ZA–series Mg alloy at high temperature [12,31,32].

Alloy	Condition	Temp. (^{o}C)	UTS (MPa)
ZA73	as–cast	200	130
ZA84	as–cast	150	126
ZA85	as–cast + ECAE (N = 6)	200	249
ZA85[a]	SHT + ECAE (N = 4)	200	261

a: this work

Chapter 5 Superplasticity of the ZA85 Magnesium Alloy Fabricated by Equal–Channel Angular Extrusion

5.1 Introduction

Combinations of light weight and high strength magnesium (Mg) alloys represent ideal materials for a wide range of applications in the automobile and aerospace industries [1,2]. However, owing to the closed–packed hexagonal (HCP) crystal structure, Mg alloys have a poor plasticity at room temperature (RT) and a limited forming and machining ability. Consequently, their potential applications are limited [3,4]. Superplastic forming (SPF) is an effective method to fabricate hard–to–form materials into complex shapes [5]. For SPF to be used in industry, the development of high strain–rate superplasticity (HSRSP), defined as superplasticity occurring at strain rates at or above 1.0×10^{-2} s^{-1} [6], is needed, especially for Mg alloys with poor formability. Another desirable property for developing superplasticity in a material is low temperature superplasticity (LTSP), defined as superplasticity occurring at temperatures at or below 0.55 T_m, where T_m is the alloy melting temperature [6].

Many previous experiments established that superplasticity requires a small polycrystalline grain size (typically less than 10 μm [7]) and these small grains are generally achieved through the application of severe plastic deformation (SPD). Equal channel angular extrusion (ECAE) is one of the most popular SPD methods and has proved to be effective in refining grains in various Mg alloys, resulting in improved ductility, strength, and superplasticity [8–14]. K. Matsubara et al. [9] reported that the Mg–9% Al alloy processed by a combination of extrusion and ECAE exhibited a maximum elongation of 840% at 200 ℃ with a strain rate of 3.3×10^{-4} s^{-1}. R.B.

Figueiredo et al. [10] reported that an ECAE ZK60 alloy showed a maximum elongation of 480% at 220 ℃ with a strain rate of 1.0×10^{-2} s^{-1}. V.N. Chuvil'deev et al. [11] found that the ECAE AZ91 alloy possessed 570% in elongation at 300 ℃ with a strain rate of 3.0×10^{-3} s^{-1} and the ECAE ZK60 alloy exhibited 810% in elongation at 260 ℃ with a strain rate of 3.0×10^{-3} s^{-1}. X. Liu et al. [14] reported that the as-rolled LZ82 alloy exhibited superplasticity with a maximum elongation of 430% at 225 ℃ and of 120% even at 150 ℃.

In the present study, the ZA85 alloy was chosen as the experimental alloy because Mg–Zn–Al (ZA) alloys have been developed as new high–strength Mg alloys for elevated–temperature applications [15,16]. The poor high–temperature properties of commercial Mg–Al–Zn (AZ) alloys are attributed to the presence of intermetallic $Mg_{17}Al_{12}$ (β–phase), which mainly precipitates along grain boundaries and exhibits a low decomposition temperature. Thus, grain boundary sliding (GBS) occurs even at temperatures below 150 ℃ [17,18]. It has been reported that a ternary addition of a large amount of zinc to binary Mg–Al alloys, with a Zn:Al composition of approximately 2:1, can completely suppress the formation of the β–phase [15,16,19]. The main precipitate of the ZA alloy is the τ–phase that has a higher melting point and decomposition temperature than the β–phase [20], leading to better properties at elevated temperatures than commercial AZ alloys. In this study, ECAE was used to refine grains and precipitates, and to eliminate defects for developing superplasticity in the ZA85 alloy. It was found that the ECAE ZA85 alloy exhibits both HSRSP and LTSP. The mechanism and activation energy of superplastic deformation of the experimental alloy were also investigated.

5.2 Experimental Procedures

An alloy with a composition of Mg–8 wt.%Zn–5 wt.%Al (ZA85) was prepared.

Pure Mg, Al, and Zn (>99.9%) were melted at 750 ℃ with SF_6 as the protective atmosphere. Steel molds with cavity dimensions of 300 mm × 70 mm × 60 mm were used for casting the alloy. The as–cast alloy in the molten state was air cooled. The chemical composition of the alloy was 8.34 wt.%Zn, 4.74 wt%Al with the balance Mg.

For the ECAE process, the dimensions of the specimens are 17 mm × 17 mm × 60 mm, and an ECAE die with 120° angle was used. Boron nitride was used as the lubricant during ECAE. An ECAE temperature of 180 ℃ was used because higher ECAE temperatures would have led to grain growth [15]. The ECAE die was preheated to 180 ℃ and maintained for 15 min before inserting a lubricated ECAE specimen into the entrance channel. The specimen was held inside the ECAE die for 5 min before pressing. The ECAE process was conducted via Route B_C in which the specimen was rotated through 90° in the same direction after each pass with a pressing speed of 2 mm/min.

Following the ECAE process, some samples were sliced perpendicular to the longitudinal axes to a 3 mm thickness. These small disks were sealed in glass tubes under vacuum and annealed for 1 h at selected temperatures ranging from 200 to 400 ℃. These static annealing experiments were used to observe the thermal stability of the microstructure.

Microstructures of the as–cast and ECAE materials were examined using standard metallographic procedures. The polished surfaces were etched with 3 mL acetic acid solution, 5 mL deionized water, 35 mL ethanol, and 1 g picric acid. The microstructures were observed by optical microscopy and scanning electron microscopy (SEM). The average grain size was determined with Image Pro software (IpWin32).

The tensile tests were conducted over temperatures ranging from 250 to 400 ℃

with the initial strain rate ranging from 1.0×10^{-2} to 1.0×10^{-4} s^{-1}, using a testing machine operating at a constant cross–head displacement rate. The tensile specimens were longitudinally cut from the samples after ECAE by wire–electrode cutting and were made with a gauge section of 6 mm × 3 mm × 2 mm. The specimens were heated to the selected temperatures and then held for 10 min prior to the tensile tests. All tensile specimens were pulled to failure to obtain information on the total elongations.

5.3 Results and Discussion

Fig. 5.1 shows the optical micrograph of the as–cast ZA85 alloy. The initial grain size of ~150 μm was obtained with an equiaxed grain structure. The coarse precipitates, identified as the τ–phase by X–ray diffraction (the same as in prior literature [19–21]), were distributed along the grain boundaries. Furthermore, defects such as blow holes and shrinkage voids were clearly observed in the as–cast specimens. These defects resulted from the air trapped in the melting alloy during casting and from the difference between the cooling rates in the inner and outer regions of the ingot. Fig. 5.2 shows the microstructure of the ECAE ZA85 alloy. After six ECAE passes at 180 ℃, the average grain size was significantly reduced to 4 μm, as shown in Fig. 5.2 (a). The mechanism of grain refinement for Mg alloys by ECAE was dynamic recrystallization (DRX) [15,22,23]. DRX led to the production of equiaxed grains with a high fraction of high–angle grain boundaries. In addition, defects such as blow holes and shrinkage voids were totally eliminated by ECAE. The precipitate size was also refined during the ECAE process; it was greatly reduced to an average of 1 μm with uniform distribution after six ECAE passes at 180 ℃, as shown in Fig. 5.2 (b).

The ECAE samples were subjected to a static annealing treatment for 1 h at

selected temperatures ranging from 200 to 400 ℃ to investigate the thermal stability of the fine–grained structure. The results are shown in Figs. 5.3 and 5.4 and it is apparent that there was reasonable grain stability up to 325 ℃; however, at higher temperatures, there was grain growth yielding grain sizes of ~13.7, ~21.0, and ~36.5 μm after annealing at 350, 375, and 400 ℃, respectively. The SEM micrographs (Fig. 5.4) show the microstructures of the ECAE samples after annealing at 300, 350, and 400 ℃. After annealing at 300 ℃ for 1 h, the average grain size merely increased to 7.1 μm, which is still desirable for superplastic deformation. This thermal stability of the fine–grained structure at the temperatures at or below 325 ℃ is attributed to the presence of the fine and well–distributed τ–phase, which inhibits grain–boundary migration. With the annealing temperature higher than 350 ℃, the average grain size increased to above 10 μm and the fine precipitates were gradually dissolved into the matrix. Fig. 5.4 (c) shows that after annealing for 1 h at 400 ℃, the fine precipitates were hardly observed in the microstructure and the average grain size increased to 36.5 μm.

Fig. 5.5 shows the stress versus elongation to failure for samples processed by six ECAE passes at 180 ℃ and then pulled to failure in tension at temperatures ranging from 250 to 400 ℃ with the initial strain rates from 1.0×10^{-2} to $1.0 \times 10^{-4}\ s^{-1}$. The outer appearance of the testing specimens is illustrated in Fig. 5.6, where the upper specimen is untested and the other specimens were pulled to failure under the selected conditions. A maximum elongation of 400% was achieved at 300 ℃ with the initial strain rate of $1.0 \times 10^{-4}\ s^{-1}$. The necking phenomenon observed in the specimens tested at 300 and 350 ℃ with initial strain rates of $1.0 \times 10^{-3}\ s^{-1}$ and $1.0 \times 10^{-4}\ s^{-1}$ is very similar to that previously reported for Mg–based alloys [9,24]. It is worth mentioning that the flow stress was relatively uniform without apparent strain hardening when testing at higher temperatures with slower initial strain rates. This

phenomenon is ascribed to the occurrence of strain softening under higher temperatures and slower initial strain rates, which compensated for the effect of strain hardening.

Fig. 5.7 shows the elongation to failure versus the initial strain rate for the ECAE samples. The inspection of Fig. 5.7 provides five significant trends. First, the maximum elongation achieved at each temperature tends to increase with temperature up to 300 ℃, but decreases at higher temperatures of 350 and 400 ℃. This is attributed to the rapid grain growth occurring above 350 ℃, as demonstrated in Figs. 5.3 and 5.4. Second, the elongations generally increase with decreasing initial strain rates, except at 400 ℃ where the peak elongation is achieved at 1.0×10^{-3} s^{-1}, and the elongation decreases when the initial strain rate is reduced to 1.0×10^{-4} s^{-1}. Third, for testing temperatures of 350 and 400 ℃, higher elongations are achieved at the initial strain rate of 1.0×10^{-2} s^{-1} with a testing temperature of 400 ℃, but the situation reverses for initial strain rates at and below 1.0×10^{-3} s^{-1}. The higher elongation achieved at 400 ℃ with the higher initial strain rate of 1.0×10^{-2} s^{-1} is ascribed to the short testing time that limits grain growth within the specimens during tensile testing. On the other hand, the slower strain rate allows grains to have sufficient time to grow, leading to a reduction in the elongations when tested at 400 ℃ in comparison with the tests conducted at 350 ℃. Fourth, the melting temperature of the ZA85 alloy is about 570 ℃ [25]. At 300 ℃, which corresponds to 0.53 T_m, elongations to failure of 147% and 400% are obtained with initial strain rates of 1.0×10^{-3} s^{-1} and 1.0×10^{-4} s^{-1}, respectively. Even at the lower temperature of 250 ℃, which corresponds to 0.44 T_m, elongation to failure of 205% is achieved with the initial strain rate of 1.0×10^{-4} s^{-1}. These results clearly demonstrate the occurrence of LTSP in the experimental alloy. The presence of LTSP is an attractive property in Mg alloys because of their susceptibility to surface oxidation when formed at elevated temperatures and their low

formability at temperatures close to RT. Fifth, at a testing temperature of 400 ℃, an elongation to failure of 113% is achieved with the initial strain rate of 1.0×10^{-2} s^{-1}, which indicates HSRSP in the experimental alloy. Therefore, after the ECAE process at 180 ℃ with six passes, the ZA85 alloy exhibits both LTSP and HSRSP.

Fig. 5.8 shows the flow stress versus the initial strain rate for the experimental alloy under the selected testing conditions. The strain rate sensitivity exponent (*m* value), which is obtained from the slopes of the fitted lines, is an important parameter during superplastic deformation. Superplastic deformation is an integrated process that combines GBS, dislocation movement, and diffusion in intracrystalline. The *m* value represents the proportion of GBS, and it is well known that high strain rate sensitivity (usually $m > 0.33$) is a characteristic of superplastic metals and alloys [26]. The stress exponent (*n* value), which is reciprocal of the *m* value, was calculated to determine superplastic deformation mechanism of the experimental alloy. The results show that the *m* values were all larger than 0.33 with the initial strain rate ranging from 1.0×10^{-4} s^{-1} to 1.0×10^{-3} s^{-1} at all testing temperatures except at 250 ℃. The *m* values of 0.55 and 0.45 corresponding to $n = 1.81$ and 2.22 were obtained with the initial strain rate ranging from 1.0×10^{-4} s^{-1} to 1.0×10^{-3} s^{-1} at 300 and 350 ℃, respectively. It has been reported that the *n* value of the GBS and the dislocation creep mechanisms are 2 and 3, respectively [26,27]. Therefore, the superplastic deformation mechanism for the specimens tested at 300 and 350 ℃ with the initial strain rate ranging from 1.0×10^{-4} s^{-1} to 1.0×10^{-3} s^{-1} is GBS. At 400 ℃, the *n* value is 3.03 ($m = 0.33$), which means that the superplastic deformation mechanism is dislocation creep.

It has been reported that GBS is accommodated by slip assisted by diffusion [28]. To understand the mechanism during the superplastic process, the activation energy for the superplastic deformation was calculated under constant strain rate using the following formula [29]:

$$Q = nR\frac{\partial(\ln\sigma)}{\partial(1/T)}$$

where Q is the apparent activation energy, n is the stress exponent, R is the gas constant (R = 8.31 J/(K·mol)), σ is the true stress, and T is the absolute temperature. It has been reported that the activation energy in Mg alloys for grain boundary diffusion and for lattice diffusion are 92 and 135 kJ mol^{-1}, respectively [30,31]. According to the relationship of lnσ versus 1/T at different strain rates during the deformation, the activation energy Q in the ECAE ZA85 alloy tested with the initial strain rate of 1.0 × 10^{-4} s^{-1} was calculated to be 88.5 kJ mol^{-1}, which is very close to the value for grain boundary diffusion. When increasing the initial strain rates to 1.0 × 10^{-3} s^{-1} and 1.0 × 10^{-2} s^{-1}, activation energies Q of 105 and 118 kJ mol^{-1} were estimated, respectively, which are higher than those for grain boundary diffusion but lower than those for lattice diffusion. Therefore, the dominant deformation mechanism of the ECAE ZA85 alloy tested at temperatures ranging from 300 to 350 ℃ is GBS controlled by grain boundary diffusion.

Fig. 5.9 shows the tensile fracture surface of the ECAE specimens tested with the initial strain rate of 1.0 × 10^{-3} s^{-1} at 250, 300, 350, and 400 ℃. In general, the failure of Mg alloys is brittle through cleavages at RT because of their HCP structure. Fig. 5.9 (a) shows that the fracture surface for the ECAE sample tested at 250 ℃ with the initial strain rate of 1.0 × 10^{-3} s^{-1} showed mainly cleavages. Fig. 5.9 (b) shows that the fracture surface consisted of some dimples and cleavages when tested at 300 ℃ with the initial strain rate of 1.0 × 10^{-3} s^{-1}. This means that the deformation of the experimental alloy gradually transformed from brittle to ductile through thermal activation. Fig. 5.9 (c) shows that the fracture surface totally changed to dimples when tested at 350 ℃ with the initial strain rate of 1.0 × 10^{-3} s^{-1}. However, when increasing the tensile testing temperature to 400 ℃, the fracture surface consisted of some

dimples and cleavages, as shown in Fig. 5.9 (d). This is attributed to the obvious grain growth effect at 400 ℃, which decreased the elongation to failure of the sample, as can be seen in Fig. 5.7. Close inspection shows that the fraction of dimples in Fig. 5.9 (b) is less than that in Fig. 5.9 (d). This matches the value of the elongation to failure in the materials shown in Fig. 5.7 with the value of the elongation that increases with the increasing fraction of dimples.

5.4 Summary and Conclusions

1. By applying the ECAE process with six passes at 180 ℃ to the as–cast ZA85 alloy, the average grain size was greatly reduced from ~150 μm to 4 μm and the precipitate size was also refined to an average of 1 μm with uniform distribution.
2. After annealing at 300 ℃ for 1 h, the average grain size only increased to 7.1 μm. This thermal stability of the fine–grained structure at temperatures at or below 325 ℃ is attributed to the presence of the fine and well distributed τ–phase.
3. A maximum elongation to failure of 400% was obtained for the ECAE ZA85 alloy tested at 300 ℃ with the initial strain rate of 1.0×10^{-4} s^{-1}.
4. By testing over a range of temperatures and strain rates, it is shown that the ECAE ZA85 alloy exhibits both LTSP (elongations of 147% and 400% at 300 ℃ with initial strain rates of 1.0×10^{-3} s^{-1} and 1.0×10^{-4} s^{-1}, respectively; an elongation of 205% at 250 ℃ with the initial strain rate of 1.0×10^{-4} s^{-1}) and HSRSP (an elongation of 113% at 400 ℃ with the initial strain rate of 1.0×10^{-2} s^{-1}).
5. In the ECAE processed ZA85 alloy, the dominant deformation mechanism for the specimens tested at 300 and 350 ℃ with the initial strain rates ranging from 1.0×10^{-4} s^{-1} to 1.0×10^{-3} s^{-1} is GBS controlled by grain boundary diffusion. At the higher testing temperature of 400 ℃, the deformation mechanism for the experimental alloy is dislocation creep.

References

[1] M. Bamberger, G. Dehm, Annual Review of Materials Research 38 (2008) 505.

[2] K. Liu, J. Meng, Journal of Alloys and Compounds 509 (2011) 3299.

[3] W.J. Kim, S.W. Chungl, C.S. Chung, D. KUM, Acta Materialia 49 (2001) 3337.

[4] L. Wu, Q. Ma, C. Zhang, Rare Metal Materials and Engineering 37 (2008) 54.

[5] R. Kaibyshev, T. Sakai, F. Musin, I. Nikulin, H. Miura, Scripta Materialia 45 (2001) 1373.

[6] T.G. Langdon, Journal of Materials Science 44 (2009) 5998.

[7] Glossary of terms used in metallic superplastic materials, Japanese Industrial Standard, JIS H7007, 1995.

[8] R.B. Figueiredo, T.G. Langdon, Scripta Materialia 61 (2009) 84.

[9] T.G. Langdon, Metallurgical Transactions 13A (1982) 689.

[10] V.M. Segal, Materials Science and Engineering A 197 (1995) 157.

[11] K.Matsubara, Y. Miyahara, Z. Horita, T.G. Langdon, Acta Materialia 51 (2003) 3073.

[12] R.B. Figueiredo, T.G. Langdon, Advanced Engineering Materials 10 (2008) 37.

[13] V.N. Chuvil'deev, T.G. Nieh, M.Yu. Gryaznov, A.N. Sysoev, V.I. Kopylov, Scripta Materialia 50 (2004) 861.

[14] G. Ben Hamu, D. Eliezer, L. Wagner, Journal of Alloys and Compounds 468 (2009) 222.

[15] B. Chen, D.L. Lin, L. Jin, X.Q. Zeng, C. Lu, Materials Science and Engineering A 483-484 (2008) 113.

[16] X. Liu, R. Wu, Z. Niu, J. Zhang, M. Zhang, Journal of Alloys and Compounds 541 (2012) 372.

[17] Y. Miyahara, Z. Horita, T.G. Langdon, Materials Science and Engineering A 420 (2006) 240.

[18] M. Kawasaki, T.G. Langdon, Journal of Materials Science 42 (2007) 1782.

[19] C.Y. Lin, H.J. Tsai, C.G. Chao, T.F. Liu, Journal of Alloys and Compounds 530 (2012) 48.

[20] R.B. Figueiredo, T.G. Langdon, Journal of Materials Science 45 (2010) 4827.

[21] M. Vogel, O. Kraft, E. Arzt, Scripta Materialia 48 (2003) 985.

[22] A. Srinivasan, U.T.S. Pillai, B.C. Pai, Metallurgical and Materials Transactions 36 A (2005) 2235.

[23] B.H. Kim, S.W. Lee, Y.H. Park, I.M. Park, Journal of Alloys and Compounds 493 (2010) 502.

[24] Z. Zhang, A. Couture, A. Luo, Scripta Materialia 39 (1998) 45.

[25] J. Zhang, Z.X. Guo, F. Pan, Z. Li, X. Luo, Materials Science and Engineering A 456 (2007) 43.

[26] N. Balasubramani, A. Srinivasan, U.T.S. Pillai, K. Raghukandan, B.C. Pai, Journal of Alloys and Compounds 455 (2008) 168.

[27] M. Janeček, M. Popov, M.G. Krieger, R.J. Hellmig, Y. Estrin, Materials Science and Engineering A 462 (2007) 116.

[28] C.W. Su, L. Lu, M.O. Lai, Materials Science and Engineering A 434 (2006) 227.

[29] H.K. Lin, J.C. Huang, T.G. Langdon, Materials Science and Engineering A 402 (2005) 250.

[30] N. Balasubramani, U.T.S. Pillai, B.C. Pai, Journal of Alloys and Compounds 457 (2008) 118.

[31] T.G. Nieh, J. Wadsworth, O.D. Sherby, Superplasticity in Metals and Ceramics, Cambridge University Press, Cambridge (1997).

[32] R.Z. Valiev, Materials Science and Engineering A 59 (1997) 234.

[33] O.D. Sherby, J. Wadsworth, Progress in Materials Science 33 (1989) 169.

[34] X. Wu, Y. Liu, Scripta Materialia 46 (2002) 269.

[35] W.J. Kim, S.W. Chung, C.S. Chung, D. Kum, Acta Materialia 49 (2001) 3337.

[36] R.S. Chen, J.J. Blandin, M. Suery, Q.D. Wang, E.H. Han, Journal of Materials Science and Technology 20 (2004) 295.

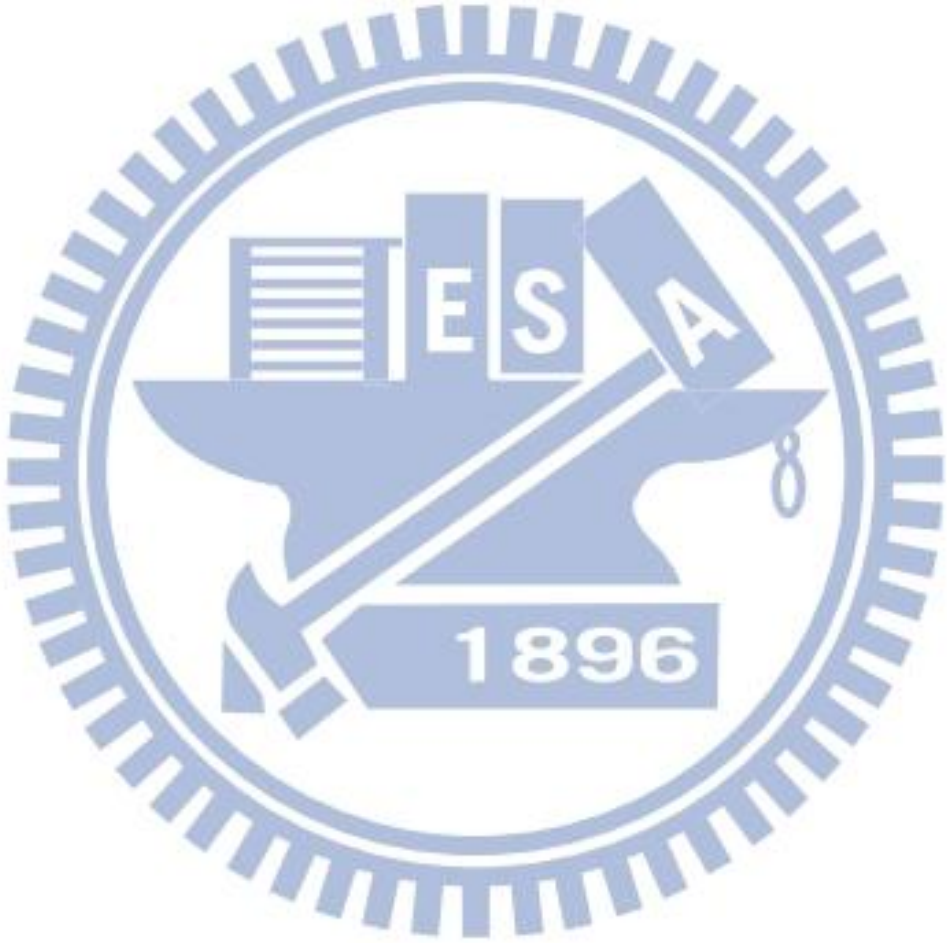

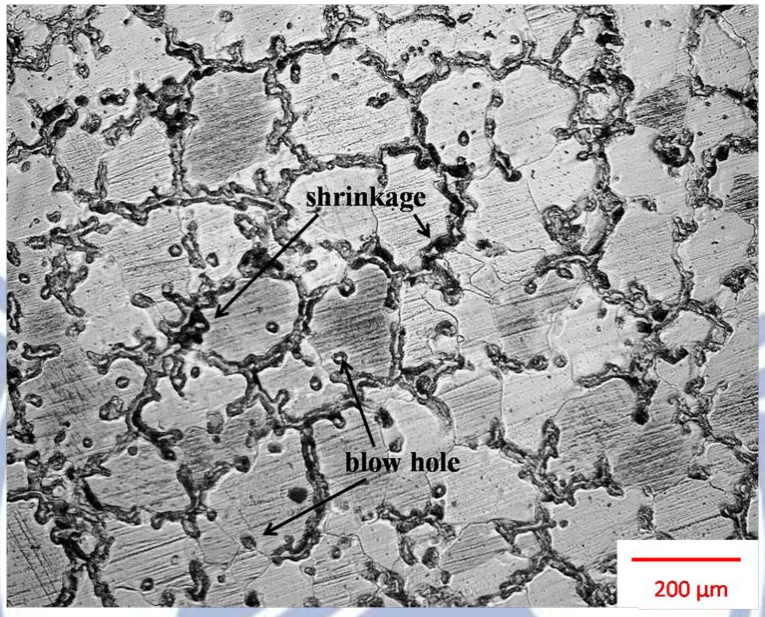

Figure 5.1. Optical micrograph of the as–cast ZA85 alloy.

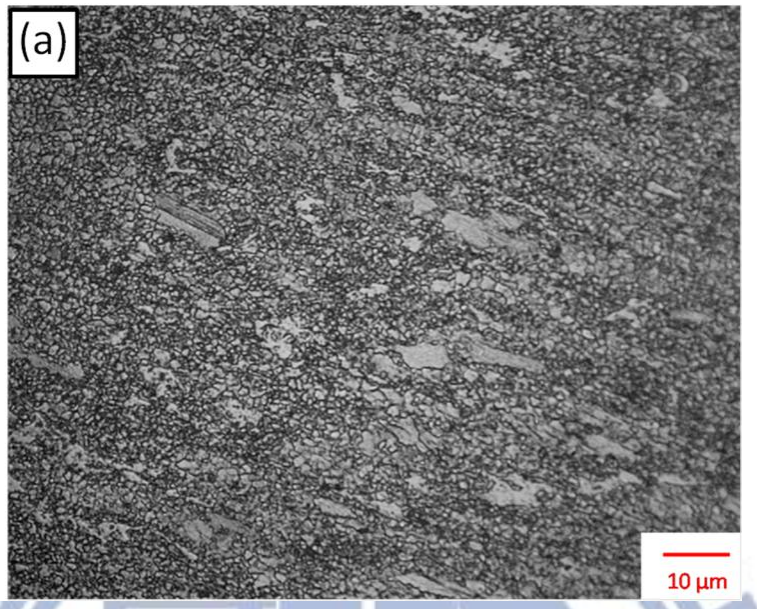

Figure 5.2 (a)

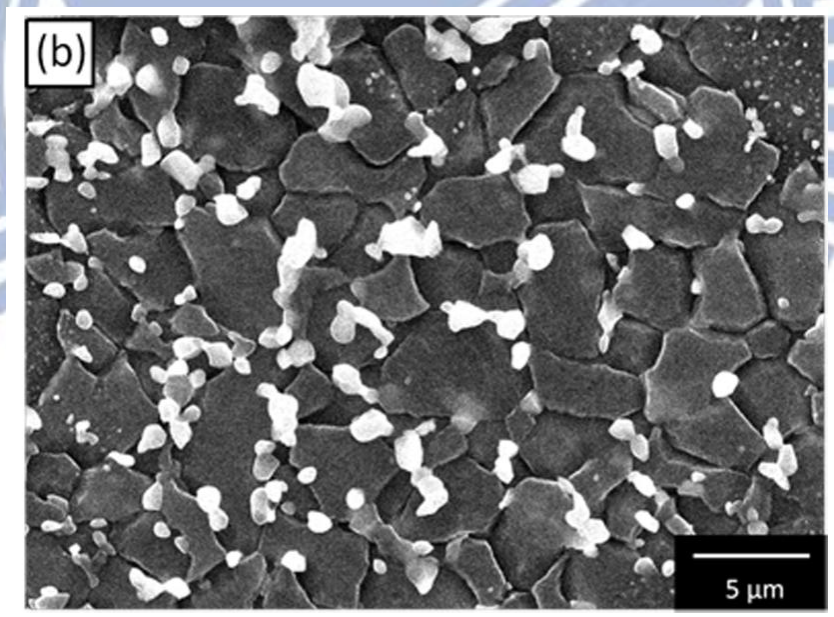

Figure 5.2 (b)

Figure 5.2. (a) Optical micrograph and (b) SEM micrograph of the ZA85 alloy fabricated by ECAE with six passes at 180 ℃.

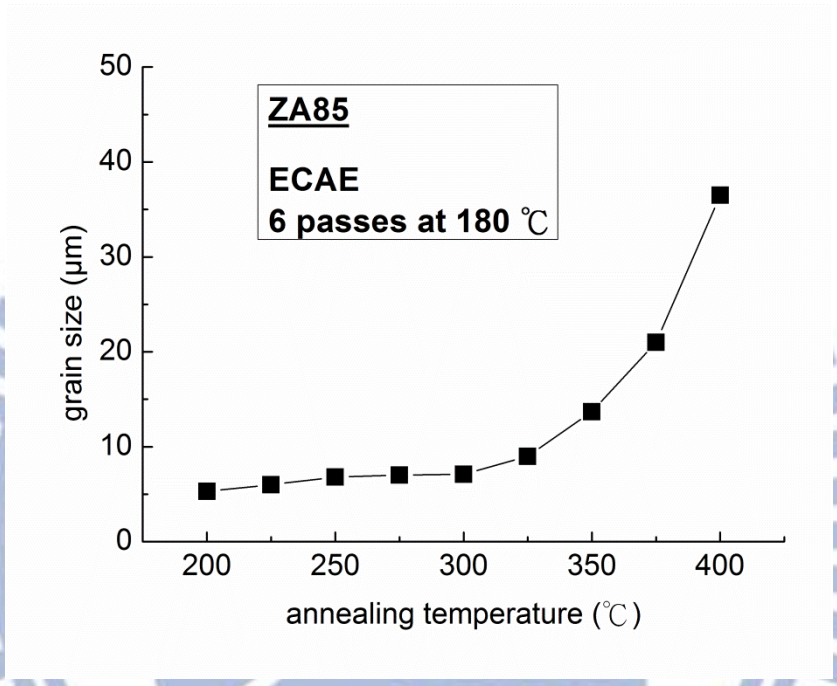

Figure 5.3. Grain size versus annealing temperature after static annealing of the material processed by ECAE with six passes at 180 ℃.

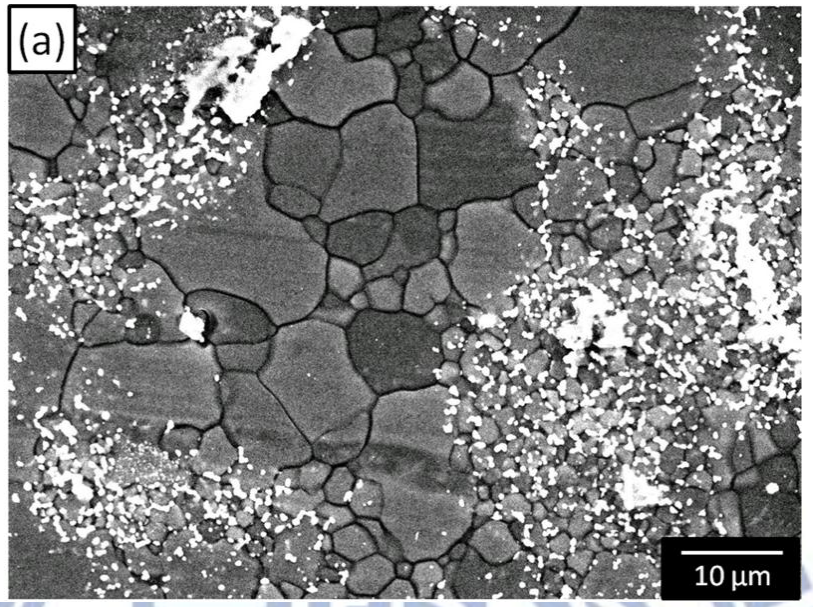

Figure 5.4 (a)

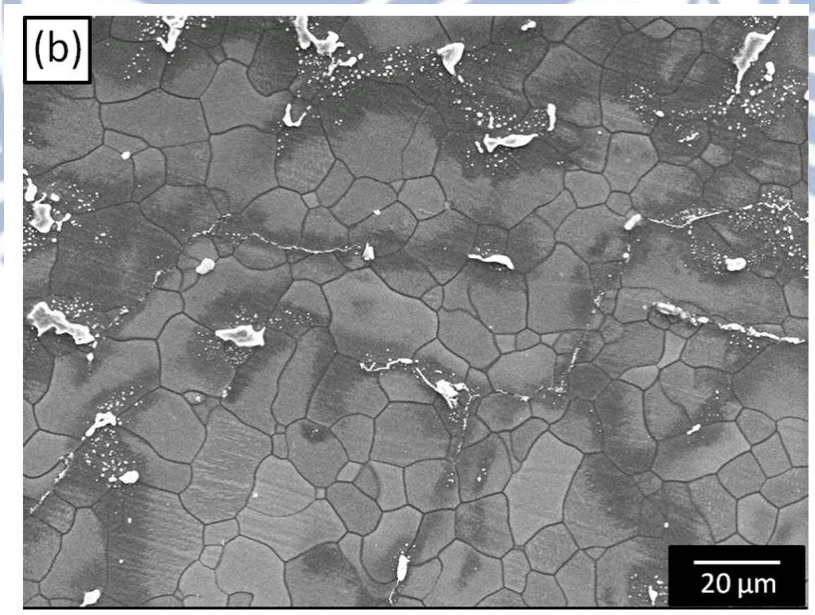

Figure 5.4 (b)

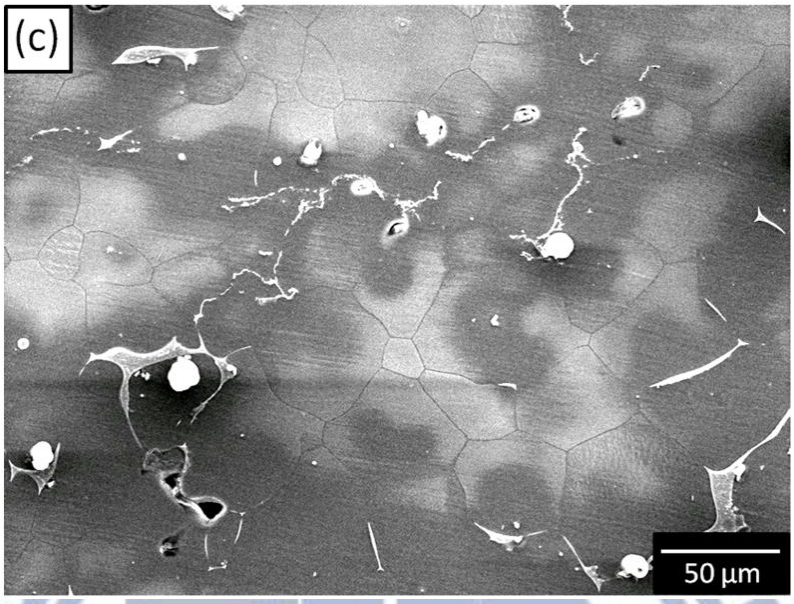

Figure 5.4 (c)

Figure 5.4. SEM micrographs of the ECAE processed ZA85 alloy after static annealing for 1 h at (a) 300, (b) 350, and (c) 400 ℃.

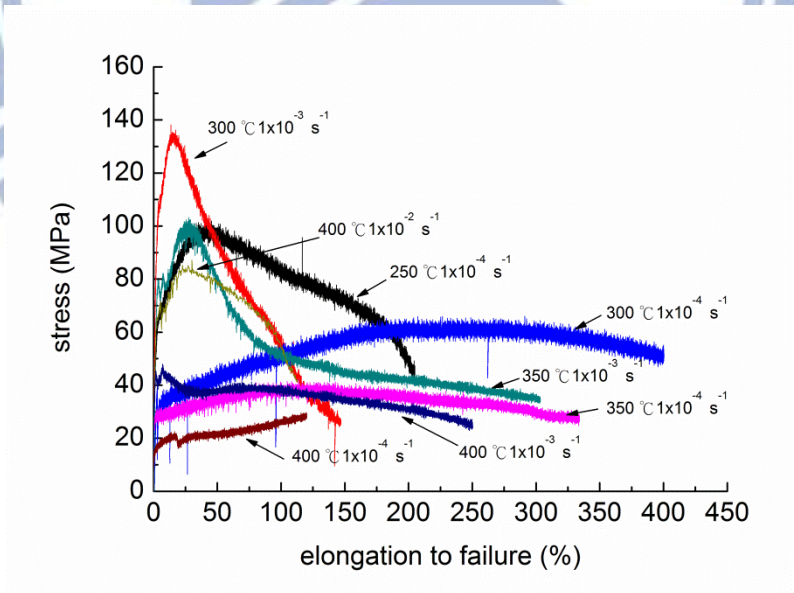

Figure 5.5. Stress versus elongation to failure for the ECAE processed ZA85 alloy at the testing temperatures ranging from 250–400 ℃ with the initial strain rates from 1.0×10^{-2} to 1.0×10^{-4} s^{-1}.

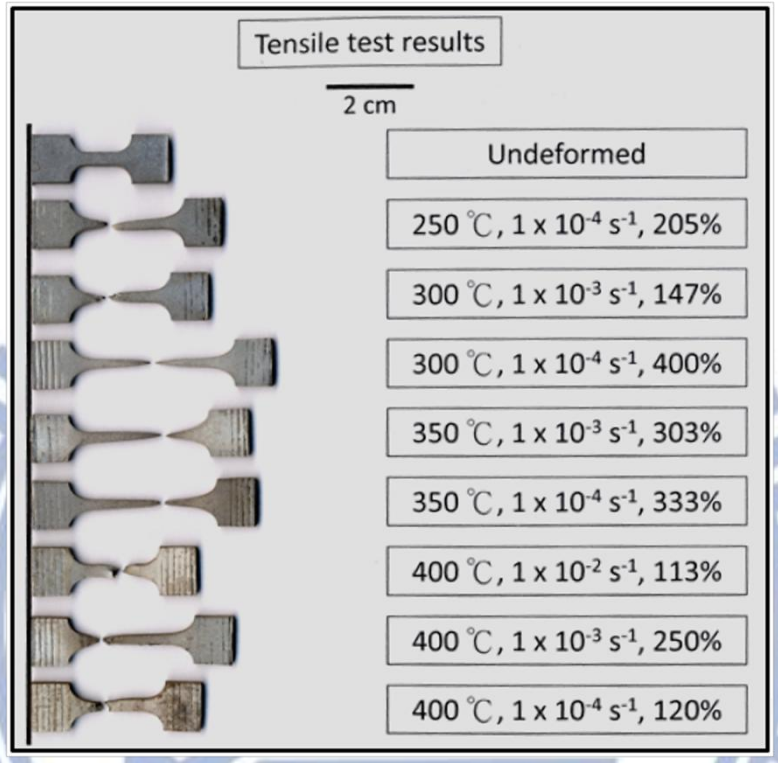

Figure 5.6. Appearance of the specimens processed by ECAE with six passes at 180 ℃ and subsequently tested in tensile to failure under the selected conditions.

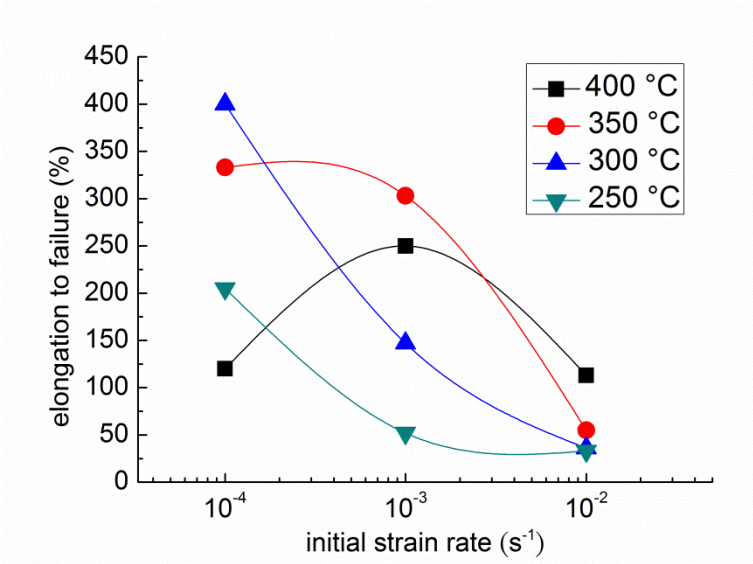

Figure 5.7. Elongation to failure versus initial strain rate over a range of temperatures for the ECAE processed ZA85 alloy.

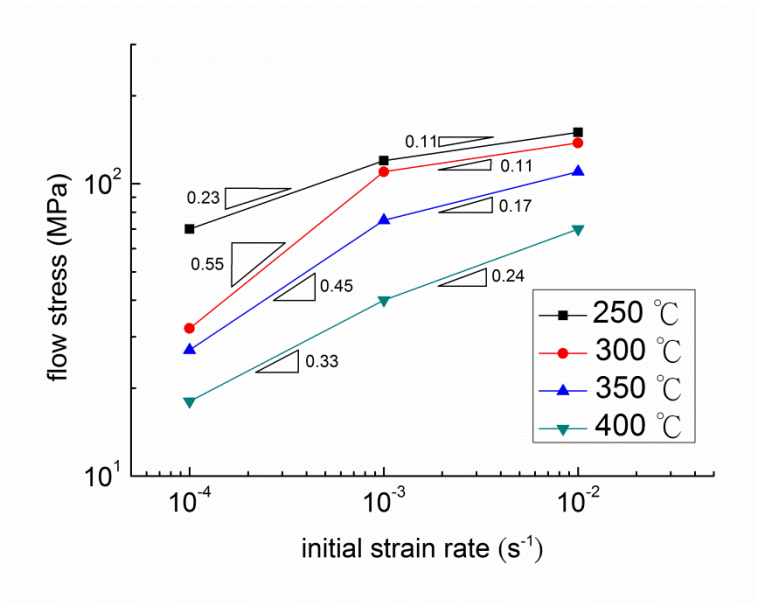

Figure 5.8. Flow stress versus initial strain rate over a range of temperatures for the ECAE processed ZA85 alloy.

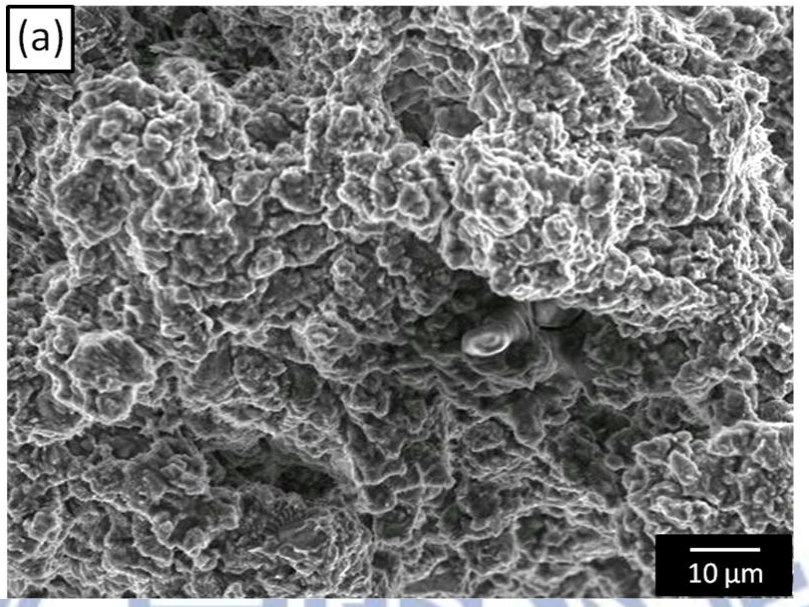

Figure 5.9 (a)

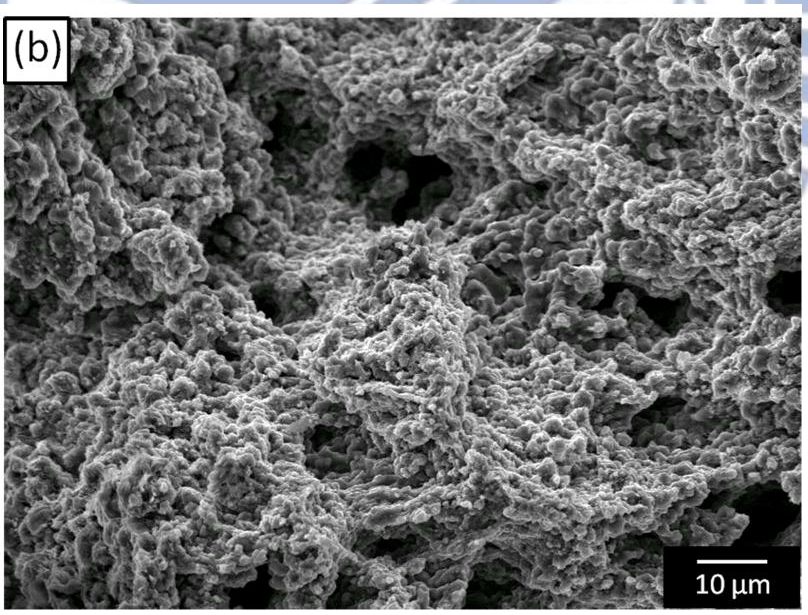

Figure 5.9 (b)

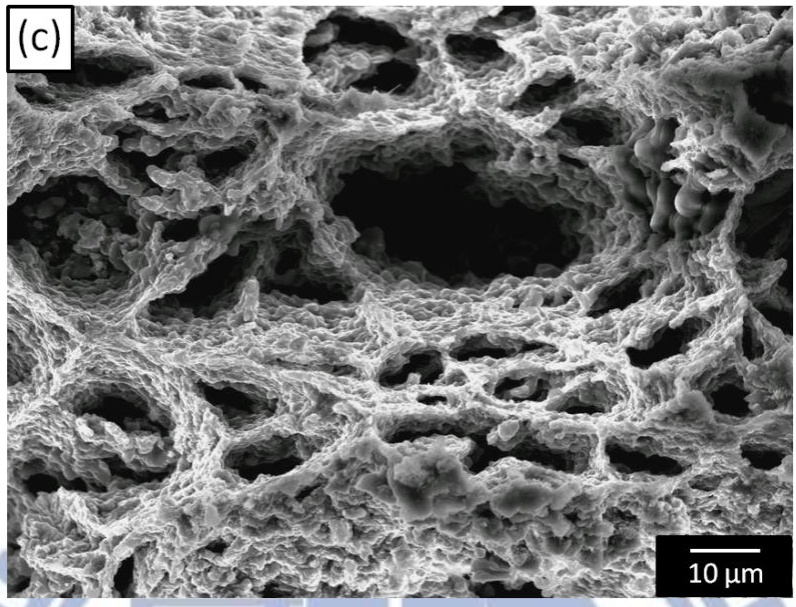

Figure 5.9 (c)

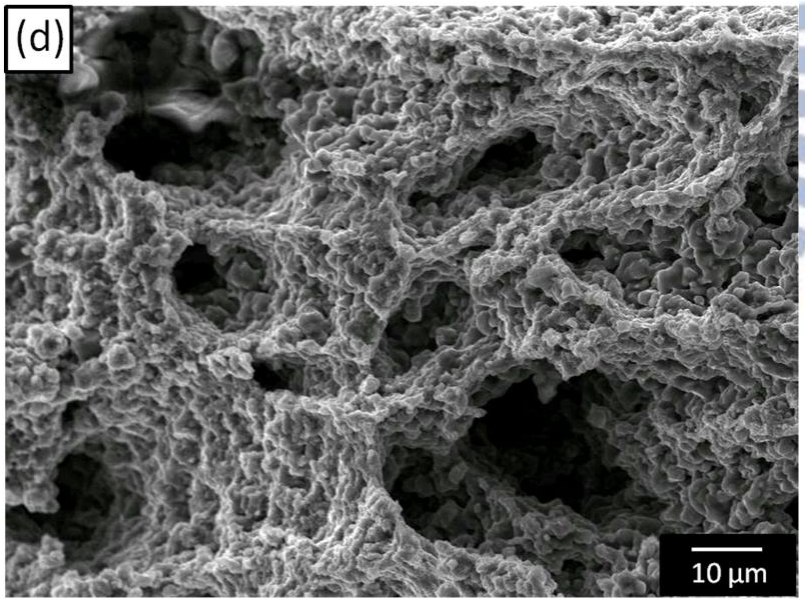

Figure 5.9 (d)

Figure 5.9. Tensile fracture surface of the ECAE processed specimens tested with the initial strain rate of 1.0×10^{-3} s^{-1} at (a) 250, (b) 300, (c) 350, and (d) 400 ℃, respectively.

Chapter 6 Summary and Conclusions

In the present study, the microstructures and mechanical properties of the as–cast ZA85 magnesium alloy were significantly improved by using equal–channel angular extrusion (ECAE). Several interesting findings were obtained and are concluded as bellow:

1. In chapter 3, the average grain size under the as–cast condition (about 150 μm) was significantly reduced to 4 μm after six ECAE passes at 180 ℃. The grain–refinement mechanism of the experimental alloy fabricated by the ECAE process is dynamic recrystallization. After one and two ECAE passes, the microstructure was not uniform, showing a "bimodal" grain size distribution; however, it became more homogeneous with further ECAE passes. The precipitate size was significantly reduced, from an average of 100 μm to 1 μm, with increasing number of ECAE passes and uniform distribution was obtained after six passes. As for the mechanical properties of the experimental alloy, after six ECAE passes at 180 ℃, hardness increased from HRB 19 to HRB 46; the UTS, YS, and elongation at room temperature (RT) increased to 402 MPa, 281 MPa, and 6.4%, respectively; the UTS, YS, and elongation at 200 ℃ increased to 249 MPa, 162 MPa, and 28.5%, respectively.
2. In chapter 4, after the solution heat treatment (SHT), a large amount of τ–phase was dissolved into the α–Mg matrix, and X–ray diffraction analysis did not indicate the presence of the τ–phase in the solution–heat–treated specimens. During the ECAE process, dynamic precipitation was observed to occur and formed fine and well–distributed τ–phase with ~100 nm in size within the α–Mg matrix. However, after six ECAE passes, some τ–phase particles grew to ~300 nm

and PFZs were clearly observed, which indicate overaging. The best mechanical properties were found in the specimen fabricated by SHT + four ECAE passes. At RT, the maximum hardness, UTS, and YS values of HRB 46, 415 MPa, and 284 MPa, respectively, were obtained. At 200 ℃, the maximum UTS and YS of 261 MPa and 173 MPa, respectively, were reached. The strengthening factors for the SHT + ECAE alloy are the grain refinement, precipitation hardening, and presence of fine and well–distributed τ–phase particles.

3. In chapter 5, after annealing at 300 ℃ for 1 h, the average grain size of the ZA85 alloy fabricated by six ECAE passes only increased from 4 to 7.1 μm. This thermal stability of the fine–grained structure at temperatures at or below 325 ℃ is attributed to the presence of the fine and well distributed τ–phase. By testing over a range of temperatures and strain rates, the ECAE processed ZA85 alloy exhibits both low temperature superplasticity (elongations of 147% and 400% at 300 ℃ with initial strain rates of 1.0×10^{-3} s^{-1} and 1.0×10^{-4} s^{-1}, respectively; an elongation of 205% at 250 ℃ with the initial strain rate of 1.0×10^{-4} s^{-1}) and high strain rate superplasticity (an elongation of 113% at 400 ℃ with the initial strain rate of 1.0×10^{-2} s^{-1}). The dominant deformation mechanism for the specimens tested at 300 and 350 ℃ with the initial strain rates ranging from 1.0×10^{-4} s^{-1} to 1.0×10^{-3} s^{-1} is GBS controlled by grain boundary diffusion. At the higher testing temperature of 400 ℃, the deformation mechanism for the experimental alloy is dislocation creep.

List of Publications

Journal Papers

1. C.Y. Lin, H. J. Tsai, C.G. Chao, T.F. Liu, “Effects of equal channel angular extrusion on the microstructure and high–temperature mechanical properties of ZA85 magnesium alloy”, Journal of Alloys and Compounds 530 (2012) 48.
2. C.Y. Lin, H.Y. Bor, C.G. Chao, T.F. Liu, “Enhanced ductility of the ZA85 magnesium alloy fabricated by equal–channel angular pressing”, Journal of Alloys and Compounds 556 (2013) 26.
3. H.C. Lee, C.G. Chao, T.F. Liu, C.Y. Lin, H.C. Wang, “Effect of Temperature and Extrusion Pass on the Consolidation of Magnesium Powders using Equal Channel Angular Extrusion”, Materials Transactions 54 (2013) 765.
4. C.Y. Lin, K.W. Ma, C.G. Chao, T.F. Liu, “Effects of equal–channel angular extrusion on the microstructure and tensile properties of the solution–heat–treated ZA85 magnesium alloy”, submitted to Metallurgical and Materials Transactions A (2014).

Conference Papers

1. 林哲毅、蔡浩然、朝春光、郭金國，ZA85 鎂合金高溫機械性質之研究，2008 年材料年會論文集，台北科技大學，P08–073 (2008)。
2. C.W. Su, H.Y. Wang, K.M. Cheng, C.Y. Lin, L.Y. Liu, Y.C. Chen, C.S. Wang, C.G. Chao, T.F. Liu, “Formation of (B2+$D0_3$) phase at a/2<100> anti–phase boundary in an Fe–23 at% Al–8.5 at% Ti alloy”, The 2008 Annual Conference of the Chinese Society For Material Science, P08–029, NTUN (2008).
3. 蘇祥溢、楊大偉、蔡浩然、林哲毅、陳蓉萱、朝春光、劉增豐，利用真空鑄

造法製造三元合金之熱電奈米線，2009 年材料年會論文集，國立東華大學，01–0305 (2009)。

4. C.Y. Lin, C.G. Chao, T.F. Liu, “Superplasticity of ZA85 magnesium alloy fabricated by equal channel angular extrusion”, Materials Science & Technology 2012 Conference & Exhibition (2012).
5. H.C. Lee, C.Y. Lin, C.G. Chao, T.F. Liu, “The effects of temperature and extrusion pass on the consolidation of magnesium powders using equal channel angular extrusion”, Materials Science & Technology 2012 Conference & Exhibition (2012).
6. C.Y. Lin, K.W. Ma, C.G. Chao, T.F. Liu, “Effects of Equal Channel Angular Extrusion on Microstructures and Mechanical Properties of Solution Heat Treated ZA85 Magnesium Alloy”, Materials Science & Technology 2013 Conference & Exhibition (2013).